RAMAN AND BRILLOUIN SPECTROSCOPIC STUDIES OF PHASE TRANSITIONS IN PEROVSKITE FERROELECTRIC MATERIALS

By

KARUNA KARA MISHRA

Enrolment No: PHYS02200704018

Indira Gandhi Centre for Atomic Research,

Kalpakkam, Tamil Nadu, India, 603 102

A thesis submitted to the

Board of Studies in Physical Sciences

In partial fulfillment of requirements

For the Degree of

DOCTOR OF PHILOSOPHY

of

HOMI BHABHA NATIONAL INSTITUTE

June 2012

Homi Bhabha National Institute

Recommendations of the Viva Voce Board

As members of the Viva Voce Board, we certify that we have read the dissertation prepared by Karuna Kara Mishra entitled "Raman and Brillouin Spectroscopic Studies of Phase Transitions in Perovskite Ferroelectric Materials" and recommend that it may be accepted as fulfilling the dissertation requirement for the Degree of Doctor of Philosophy.

Chairman: Prof. C. S. Sundar	Date
Convenor: Prof. A. K. Arora	Date
Examiner:	Date
Member: Dr. T. R. Ravindran	Date
Member: Dr. R. K. Dayal	Date

Final approval and acceptance of this dissertation is contingent upon the candidate's submission of the final copies of the dissertation to HBNI.

CERTIFICATE

I here by certify that I have read this dissertation prepared under my direction and recommend that it may be accepted as fulfilling the dissertation requirement.

Date: Prof. Akhilesh Kumar Arora (Guide)

Place:

STATEMENT BY AUTHOR

This dissertation has been submitted in partial fulfillment of requirements for an advanced degree at Homi Bhabha National Institute (HBNI) and is deposited in the Library to be made available to borrowers under rules of the HBNI.

Brief quotations from this dissertation are allowable without special permission, provided that accurate acknowledgement of source is made. Requests for permission for extended quotation from or reproduction of this manuscript in whole or in part may be granted by the Competent Authority of HBNI when in his or her judgment the proposed use of the material is in the interests of scholarship. In all other instances, however, permission must be obtained from the author.

Karuna Kara Mishra

DECLARATION

I, hereby declare that the investigation presented in the thesis has been carried out by me. The work is original and has not been submitted earlier as a whole or in part for a degree/diploma at this or any other Institution/University.

Karuna Kara Mishra

DEDICATIONS

To My Beloved Parents

Smt. Allhadini Mishra

Shri. Goutama Mishra

ACKNOWLEDGEMENTS

First and foremost, it is a great pleasure for me to express my deep sense of gratitude and indebtedness to Dr. A. K. Arora, my supervisor whose encouragement, invaluable guidance and constant support made this thesis a reality. This thesis would not have been possible without his efforts and supports. His motivation and enthusiasm constantly motivated me.

I am highly grateful to Dr. V. Sivasubramanian, who had immensely helped me in synthesis of samples and many useful discussions and encouragement during the entire tenure of my Ph.D. He also taught and guided me, how to operate Brillouin spectrometer and analyze the data. I would like to acknowledge Dr. T. R. Ravindran for guidance in Raman spectroscopic measurements, useful discussion, support and encouragement. I am grateful to Dr. B. V. R. Tata for his support and encouragement. I extend my sincere thank to Mr. Sarguna and Ms. Kalavati for their timely help in X-ray diffraction measurements. I would like to thank Mr. A. T. Satya and Dr. A. Bharathi for magnetization studies on the samples. The help rendered by Ms. Shabana Khan and Dr. R. Divakar for TEM measurements, Dr. C. R. Das, and Dr. S. Hussain of UGC-DAE-CSR, Kalpakkam-node for recording SEM images and EDS spectra, Dr. V. Sridharan, and Dr. D. Pradhan of NIT, Rourkela for dielectric and Dr. V. R. K. Murthy of IIT, Chennai for P-E loop measurements during the course of my research is gratefully acknowledged. I like to thank Mr. Jagadessan for the assistance in smooth running of my computer.

I am very happy to recall the company enjoyed in lab during my Ph. D tenure with other members of laboratory, Dr. S. Sahoo, Ms. S. Sohila, Ms. S. Chakraborty, and Ms. K. Kamali.

I would like to thank all my teachers, who had taught me at various stage of my educational career. It is my great pleasure to thank Dr. K. S. Viswanathan, M. C. Valsakumar, G. Amarendra and more for their teaching and encouragement during the course work period.

Thanks are due to my doctoral committee members (Dr. A. K. Arora, Dr. C. S. Sundar, Dr. T. R. Ravindran, and Dr. R. K. Dayal) for their useful suggestions and evaluation of my research work.

I am extremely grateful to Dr. C. S. Sundar, Director, Material science Group and Director, Indira Gandhi Center for Atomic Research, for extending the support and constant encouragement. I would like to thank the member of administration, accounts and management group of IGCAR for their kind and valuable supports.

It is my pleasure to thank my batch mates Bisnu, Prasana, Kalpataru, Hari Babu, Varghese, Sorb, Saravanakumar, Girish, Rahul, Joyshankar, Madhu, Subhra, Rajini and Nithila for their cooperation during my stay at JRF enclave and at IGCAR. The affection of senior and love of junior scholars are highly acknowledged.

Finally, I wish to express my deep sense of gratitude to my family members and my late grand parents for their immense patience, love, affection, encouragements and support. I am indebted to my parents for giving me the moral and emotional support at every stage of my life. It is only because of their kind blessing that I could complete this work.

Karuna Kara Mishra

List of Publications/Preprints

Publications in Journals/Preprints

1 Low-temperature Raman spectroscopic studies in $NaNbO_3$
K. K. Mishra, V. Sivasubramanian, and A. K. Arora, J. Raman Spectrosc. **42**, 517 (2011).

2 Raman scattering from La-substituted $BiFeO_3$–$PbTiO_3$
K. K. Mishra, V. Sivasubramanian, R. M. Sarguna, T. R. Ravindran, and A. K. Arora, J. Solid State Chem. **184**, 2381 (2011).

3 *x*-T phase diagram of La-substituted $BiFeO_3$-$PbTiO_3$
K. K. Mishra, R. M. Sarguna, S. Khan, and A. K. Arora, AIP Advances **1**, 032126 (2011).

4 Vibrational, magnetic, and dielectric behavior of La-substituted $BiFeO_3$-$PbTiO_3$
K. K. Mishra, A. T. Satya, A. Bharathi, V. Sivasubramanian, V. R. K. Murthy, and A. K. Arora, J. Appl. Phys. **110**, 123529 (2011).

5 Anomalous behavior of acoustic phonon mode and central peak in $Pb(Zn_{1/3}Nb_{2/3})_{0.85}Ti_{0.15}O_3$ single crystal studied using Brillouin scattering
K. K. Mishra, V. Sivasubramanian, A.K. Arora, and D. Pradhan (Under review).

6 Brillouin spectroscopic study of central peak in $NaNbO_3$ single crystal
K. K. Mishra, V. Sivasubramanian, A. K. Arora, and R. M. Sarguna (Under review).

7 Polarized *micro*-Raman spectroscopic study of relaxor $Pb(Zn_{1/3}Nb_{2/3})_{0.85}Ti_{0.15}O_3$ single crystal
K. K. Mishra, V. Sivasubramanian, A. K. Arora, and D. Pradhan (Under review).

Publications not included in thesis

8 Impedance and Raman spectroscopic studies of $(Na_{0.5}Bi_{0.5})TiO_3$
B. K. Barick, **K. K. Mishra**, A. K. Arora, R. N. P. Choudhary, and D. Pradhan, J. Phys. D: Appl. Phys. **44**, 355402 (2011).

9 Low Frequency Raman Scattering from Confined Acoustic Phonons in Free Standing Silver Nanoparticles
Venu Mankad, **K. K. Mishra**, S. K Gupta, T.R. Ravindran, and P. K. Jha, J. Vibrational Spectrosc. **61**, 183 (2012).

Published Conference Proceedings

1 Raman spectroscopic study of the coexistence of phases in $NaNbO_3$
K. K. Mishra, V. Sivasubramanian, and A.K. Arora
Proc. 54^{th} DAE Solid State Physics Symp. P. 159 (Boroda 2009).

2 Phonons in La-Substituted $BiFeO_3$-$PbTiO_3$
K.K.Mishra, V.Sivasubramanian, R.M.Sarguna, T.R.Ravindran, and A.K.Arora, Int. Conf. on Physics of Emerging Functional Material (Mumbai, 2010) AIP Conf. Proc. **1313**, 174-176 (2011).

3 Magnetic ordering in La-substituted $BiFeO_3$-$PbTiO_3$
K. K. Mishra, A.T. Satya, A. Bharathi, and A. K. Arora, 56^{th} DAE Solid State Physics Symp. (Chennai, 2011) AIP Conf. Proc. **1447**, 1149-1150 (2012).

Conference papers – Unpublished (Abstract only)

4 Tetragonal-Cubic transition in multiferroic La-substituted $BiFeO_3$-$PbTiO_3$
K. K. Mishra, R. M. Sarguna, and A. K. Arora
National Conf. on Recent Trends in Material Science (Wakanaghat, 2011).

Synopsis

Introduction

Perovskite ferroelectric compounds with general formula ABO_3 have been of interest both from fundamental and applications point of view.[1] Ferroelectricity arises when centre of positive charges does not match with that of negative charges in the unit cell. In contrast to pure compounds, solid solutions obtained by partial substitution at either *A* or *B* site or both led to broad and frequency dependent dielectric response peak as a function of temperature.[1] This was attributed to existence of polar nano regions,[1] which exhibited a distribution of relaxation time. These substituted systems were termed as relaxor-ferroelectric, where one could tailor the dielectric properties by controlling the composition. Another class of materials, where magnetic and electrical ordering can coexist over certain temperature range are termed as 'multiferroic'.[2, 3] However, magnetic ferroelectrics are scarce in nature because the conventional mechanism for ferroelectricity, namely an off-centering of the cations, which can be achieved best in ions with empty *d*-shells, whereas the formation of ferro-, ferri- and antiferro-magnetic order require the presence of (3*d*) transition metal ions with partially filled *d*-shells.[4] Subsequently, researchers discovered that in ABO_3 Perovskite oxides, the stereo-chemically active $6s^2$ lone-pair electrons of ions in the *A*-site (Bi^{3+}, Pb^{2+}etc.) offer an alternate way to get the ferroelectric ordering irrespective of the nature of magnetic ions present in the *B*-site.[4] Due to coupling of the two properties in such system it is possible to modify one type of ordering by controlling the other. This generated considerable interest in search of new partially and fully substituted multiferroic Perovskite system.[2, 3]

This thesis reports Raman and Brillouin spectroscopic investigations of phase transitions in one representative system of each type: (a) ferroelectric $NaNbO_3$, (b) relaxor-ferroelectric $Pb(Zn_{1/3}Nb_{2/3})_{0.85}Ti_{0.15}O_3$ (PZN-PT) and (c) multiferroic $(Bi_{1-x}La_x)_{0.5}Pb_{0.5}Fe_{0.5}Ti_{0.5}O_3$, $0 \leq x \leq 0.5$ (BLF-PT). Temperature is used as a primary thermodynamic parameter to take the system across

phase transition(s). Where ever possible, both polycrystalline ceramic samples and single crystals are investigated. In the case of BLF-PT, tetragonal-cubic structural transition induced by La-composition as well as by temperature is studied using *in-situ* high temperature X-ray diffraction. Supporting dielectric and magnetic measurements are also carried out, where ever necessary and correlation of these properties to structural changes are discussed. The new results obtained from the present set of studies are listed towards the end of the synopsis.

Experimental details

(a) *Synthesis*: Polycrystalline $NaNbO_3$ powder samples were synthesized by solid state reaction method. Stoichiometric ratio of Na_2CO_3 and Nb_2O_5 was calcined at 1123 K followed by sintering at 1373 K. Transparent and colourless single crystals of $NaNbO_3$ were grown by flux method with Na_2CO_3 and B_2O_3 as fluxes. The crystals were grown by cooling from 1448 to 1048 K at a rate of 1.5 K / h. Transparent yellow coloured single crystals of PZN-PT were grown by flux method with Pb_3O_4 as flux.[5] The charge and flux were taken in ratio 40:60 by weight. The crystals were grown by cooling from 1473 to 1203 K at a rate of 0.8 K / h. Polycrystalline BLF-PT samples for $0 \leq x \leq 0.5$ were synthesized by the solid-state reaction technique. High purity starting materials (Bi_2O_3, La_2O_3, PbO, Fe_2O_3, and TiO_2) were mixed in stoichiometric proportion and ground together. Calcinations were done at 773 K and 1073 K followed by sintering at 1373 K. Precaution was taken to avoid loss of PbO from the sample. This was done by placing $PbZrO_3$ powder around the pellet which maintains a high partial pressure over the sample.[6] The pellets were about 10.5 mm in diameter and 1.5 mm thick.

(b) *Characterization*: Samples were checked for phase purity using X-ray diffractometer (Siemens D500) and transmission electron microscope (JEOL–2000 EX II) operated at 200 kV. Energy dispersive X-ray analysis (EDAX) and microstructural analysis (i.e., grain size, grain

distribution, voids etc.) of the samples were carried out using a scanning electron microscope (Cam Scan CS 3200).

(c) *Measurements*: Temperature dependence Raman measurements in the range 10-300 K were carried out using a closed cycle helium refrigerator (APD 202) in the back-scattering geometry using 350 mW power of the 488 nm line from an Ar ion laser. Scattered light was analyzed using a double monochromator (SPEX 14018) and detected using a photomultiplier tube (Hamamatsu R943-02) operating in the photon counting mode.[7] Raman spectra were also recorded using a *micro*-Raman spectrometer (Renishaw InVia) and 514.5 nm excitation. In the *micro*-Raman set up a Linkam heating-cooling stage was used for changing temperature between 80 and 873 K. Brillouin spectra were measured in backscattering geometry using a high-contrast 3 + 3-pass tandem Fabry-Perot interferometer (JRS Scientific Instruments) in the *T* range 300-873 K using a commercially available heating stage with a stability of ± 0.1 K. The sample was excited using 532 nm light using a single-mode diode-pumped solid state laser (Innolight Diabolo 500). X-ray diffraction patterns as a function of temperature were obtained using an Edmund Buhler high temperature attachment. Magnetization (*M~H* loop) were obtained using a vibrating sample magnetometer (ADE EV9) up to a maximum field of ± 50 kOe at ambient and down to 4 K. The zero field cooled (ZFC) and field cooled (FC) magnetization were also measured as a function of temperature in the range 4-300 K. For *P-E* measurements, the pellets were silver-electroded on both sides and the measurements were carried out using an automatic *P-E* loop tracer (Marine India). The dielectric parameters (capacitance and dissipation factor) were measured in a wide range of frequency (100 Hz to 1 MHz) using a computer–controlled impedance analyzer (PSM: N4L 1735) in the temperature range 300-585 K.

Studies on Ferroelectric $NaNbO_3$

$NaNbO_3$-based ferroelectric systems such as $(Li_xNa_{1-x})NbO_3$, $(K_xNa_{1-x})NbO_3$ with ultrahigh piezoelectric response comparable to $Pb(Zr_xTi_{1-x})O_3$ has evoked considerable interest as next generation ecofriendly lead-free piezoelectric ceramics required for various applications. $NaNbO_3$ exhibits a large number of structural phase transition as a function of temperature.[8-10] It is reported to show a transition from paraelectric to antiferroelectric at 753 K,[10] antiferroelectric to antiferroelectric at 633 K[10] and then to a ferroelectric phase at 180 K.[8] The transition from anti-ferroelectric to ferroelectric phase is also accompanied a change in structure from orthorhombic to rhombohedral.[8] Although the phase transitions in $NaNbO_3$ have been studied by several researchers,[8-10] the two-phase coexistence has not been investigated using Raman spectroscopy. Furthermore, coexistence inferred from X-ray and neutron diffraction do not appear to be same.[8, 10]

In order to obtain better understanding of two-phase coexistence in this system, a detailed Raman spectroscopic study of $NaNbO_3$ was carried out both in cooling and heating cycles in the temperature range 10–300 K. For this, a single-phase polycrystalline sample was synthesized by solid state reaction method. The spectra were analyzed by fitting Lorenzian line shapes and mode wavenumber, line-width and integrated intensity were obtained. During cooling cycle, at room temperature, a total of 19 distinct Raman modes were identified in the frequency range 30-950 cm^{-1}. The observed modes were found to be less than those predicted by group theory ($15A_g + 17B_{1g} + 15B_{2g} + 13B_{3g}$). This could be either due to accidental degeneracy of phonon frequencies or due to the insufficient intensities arising from small polarizability of modes. On the other hand, at 10 K in the low-temperature ferroelectric phase only 12 distinct Raman modes could be found in the same frequency range. The intensities of modes characteristic of orthorhombic phase gradually decreased initially upon cooling and exhibited a marked change below 220 K. Similarly during heating cycle, spectral features begin to exhibit noticeable changes above 240

K. These observations clearly indicated that the phase transition from anti-ferroelectric to ferroelectric phase begins at 220 K on cooling while the reverse transition starts at 240 K upon heating. The normalized integrated intensities of the modes at 60, 123, 180, 274 cm^{-1} characteristic of orthorhombic phase and 556 cm^{-1} characteristic of rhombohedral phase were investigated to understand the temperature range of coexistence of anti-ferroelectric and ferroelectric phases during cooling and heating cycles. These findings suggested that both anti-ferroelectric and ferroelectric phases coexist between 220 and 160 K during cooling cycle and between 240 and 300 K during heating cycle.[7] From these results a hysteresis of about ~80 K was also evident. The reason for different coexistence regions found from different techniques could be either due to the sample volume probed by the technique or due to different synthesis procedures used by different researchers.

Understanding the dynamics and the nature of structural phase transitions have been important issues in ferroelectric materials.[11, 12] Many systems have been found to exhibit a central peak in the Brillouin spectrum near the phase transition temperature.[13] Appearance of central peak has been attributed to a relaxation process associated with microscopic ferroelectric polarization. A central peak in $NaNbO_3$ has also been found in the Raman spectrum in the vicinity of orthorhombic ($D_{2h}^{11}, Z = 8$) to the orthorhombic ($D_{2h}^{13}, Z = 24$) phase transition at 643 K.[14] In order to study the relaxation process in the vicinity of the phase transition, *in-situ* temperature dependent Brillouin scattering measurements were carried out on single crystal using large free spectral range of 3300 GHz over a wide temperature range from ambient to 773 K.

Single crystals of $NaNbO_3$ were grown by flux method and crystal plane was found to be (0-10) from Laue pattern. For Brillouin measurement, sample was excited using 532 nm light from a single-mode diode-pumped solid state laser. A broad central peak (CP) was found above

493 K. Upon heating it became weak and vanished above 743 K. Two low frequency optical phonons in the spectra were also present. The Brillouin spectra were quantitatively analysed by fitting to a sum of a damped harmonic oscillators and a relaxator function. The behaviour of mode frequencies, damping constant, inverse relaxation time and integrated intensities of the phonon modes and the central peak were examined as a function of temperature. The integrated intensity of CP and phonon mode were found to show similar temperature dependence suggesting that no intensity transfer occured between the CP and phonon mode. Maxima in the two intensities were found around $T_C \sim 643$ K. The inverse relaxation time of the CP decreased upon heating from 593 K to T_C and again increased in the orthorhombic ($D_{2h}^{13}, Z = 24$) phase. This suggested that the inverse relaxation time displays a critical slowing down in the vicinity of T_C and the nature of the phase transition being order-disorder type.

Investigations on PZN-PT relaxor single crystal

In last few decades, Lead-based relaxor ferroelectric materials have attracted the scientific community from the view points of fundamental physics aspects as well as industrial application.[15-17] $Pb(Zn_{1/3}Nb_{2/3})O_3$(PZN)-based relaxor ferroelectrics are known to be excellent piezoelectric materials. Upon doping PZN with $PbTiO_3$, $(PZN)_{1-x}(PT)_x$ exhibits ultrahigh electromechanical properties that makes these materials very important for industrial application.[18, 19] The central features of the complex behavior in these materials are the nucleation and growth of the polar nano regions (PNRs). Brillouin scattering study on PZN-PT single crystal over a wide temperature range was carried out to understand the dynamical behavior of PNRs and tetragonal (*P4mm*) to cubic (*Pm3m*) phase transition.

Single crystals of $Pb(Zn_{1/3}Nb_{2/3})_{0.85}Ti_{0.15}O_3$ ($x = 0.15$) were grown by flux method. The dielectric parameters (capacitance and dissipation factor) were measured in a wide range of frequency using an impedance analyzer in the temperature range 300-585 K. The temperature

dependence of the dielectric constant (ε) showed only one dielectric peak at ~490 K in the temperature range of investigation. The dielectric peak corresponded to the tetragonal-cubic (T_{tc}) phase transition. The observed phase transition temperature agrees well with that reported by others.[20] A weak frequency dispersion was observed at T_{tc} which suggested the relaxor nature of the sample.

Brillouin spectra were measured in backscattering geometry using a high-contrast 3 + 3-pass tandem Fabry-Perot interferometer. The spectra were recorded using two free spectral ranges (FSR) of 100 and 400 GHz. Brillouin spectra in the FSR of 100 GHz were measured between 300 and 873 K in heating cycle. A Brillouin doublet corresponds to the LA mode were found in each spectrum. Brillouin shift, full width at half maximum (FWHM), and intensity of each LA mode were obtained from analysis. Brillouin shift of the LA mode and its FWHM as a function of temperature showed clear anomalies at T_{tc} ~ 463 K. The anomalous behaviors of Brillouin shift, FWHM of LA mode and change in its intensity suggested the Burn's temperature T_B to be ~650 K. In addition, a narrow central peak (CP-n) was also found. Brillouin measurements were also made using a FSR of 400 GHz at elevated temperature to examine, if there existed a broad central peak (CP-b), characteristic of PNRs. The behavior of CP-b was similar to that of CP-n suggesting the existence of two relaxation processes.[21] The CPs disappeared above a characteristic temperature T^* ~525 K. The relaxation time τ_{LA} of the polarization fluctuations associated with acoustic phonons,[22, 23] was calculated in the relaxor-cubic phase region. In addition, above T_{tc} the relaxation times were also determined from CPs (CP-n and CP-b) assuming a Debye-relaxation process. A good agreement between relaxation time τ_{LA} obtained from LA phonon mode and that obtained from CP-b was found. This suggested that the relaxation of PNRs is determined by polarization fluctuations coupled with local strain fluctuations via LA phonon mode.[23]

In order to study the tetragonal-cubic phase transition and relaxor behaviour in the cubic phase, polarized Raman spectra were recorded in $X(YY)X'$ and $X(YZ)X'$ scattering geometries using the *micro*-Raman spectrometer up to 873 K. The spectra were fitted to multi-Lorenzian line shapes to determine the peak positions, FWHM and intensities. The assignment of Raman modes were carried out in accordance with the Raman selection rules. In the temperature dependence of mode frequencies, in both VV and VH geometries, a change in slope $d\omega/dT$ was found across the tetragonal-cubic transition around T ~473 K, similar to that obtained from Brillouin measurements. Disappearance of some modes was also found across the transition in both the geometries. Symmetry forbidden Raman modes found in cubic phase has been argued to be due to existence of PNRs.[24, 25] Other Raman parameters such as integrated intensity, line width of modes were also examined to understand the dynamics of PNRs in cubic relaxor phase.

Studies on multiferroic BLF-PT

This thesis also reports a detailed study on a typical multiferroic system: La-substituted BLF-PT. The mixed crystals of $BiFeO_3$-$PbTiO_3$ (BF-PT) with ratio around 50:50 have been reported to favor the formation of chemically ordered micro-regions in which spiral spin modulation decreases.[26] The effect of La-doping on magnetic and electrical behavior of $0.45(Bi_{1-x}La_xFeO_3)$-$0.55(PbTiO_3)$ has been studied[27] only in a limited range of $0.1 \leq x \leq 0.3$ and polarization and magnetization was found to be higher than those in pure $BiFeO_3$. Subsequently improved dielectric and magneto-electric properties were reported[28] for the system $0.50(Bi_{1-x}La_xFeO_3)$-$0.50(PbTiO_3)$ for $x = 0.5$ composition. However, the behaviors of phonons, magnetic and dielectric properties have not been investigated over a wide range of La-composition so far. In the present work, phonons, magnetic and ferroelectric ordering in La-substituted BLF-PT were investigated for $0 \leq x \leq 0.5$ ceramic samples using Raman, magnetization and polarization measurements as a function of temperature. The emphasis was to understand the nature of the

phonons in this mixed-crystal system and to probe the crystallographic phase transition as a function of La-composition and temperature. In addition, the effect of crystal-anisotropy on vibrational, magnetic, and ferroelectric properties are addressed.

Polycrystalline BLF-PT samples were synthesized for $0 \leq x \leq 0.5$ by the solid-state reaction technique. X-ray powder diffraction patterns of the sintered samples were measured to determine the structure and confirm the phase purity. *In-situ* temperature-dependent Raman measurements on pellets were made using the Linkam heating-cooling stage. The spectra were analysed by fitting to Lorenzian line shapes. Magnetization (*M~H* loop) measurements were carried out using a vibrating sample magnetometer up to a maximum field of ± 50 kOe at ambient and down to 4 K. The zero field cooled (ZFC) and field cooled (FC) magnetization were measured as a function of *T* in the range 4-300 K. The *P-E* measurements were carried out using automatic *P-E* loop tracer.

The compositions (final stoichiometry) estimated from EDAX were found to be in fair agreement with those of the starting compositions. The X-ray diffraction patterns were analysed and it was found that the lattice anisotropy (*c*/*a*) becomes smaller with increasing La-content. For $x \geq 0.4$, the diffraction patterns fitted to a cubic structure with space group *Pm3m*. This suggested that the structural change from tetragonal to cubic phase arises due to the homovalent substitution of Bi (ionic radius 1.34 Å) by La (ionic radius 1.36 Å).[29] Raman spectrum of pure BF-PT and also those of La-substituted compounds were analyzed using multi-Lorenzian fitting. A total of 10 Raman modes were identified for $x = 0$ and 7 modes for $x = 0.5$. The mode frequencies in the tetragonal phase were assigned by comparing with those of $PbTiO_3$. All the modes are found to broaden with increasing La-composition. The line-shape broadening was attributed to the substitutional disorder arising from the random occupancy of cation site *A* by Bi/Pb/La and of cation site *B* by Fe/Ti.[24] The modes in the cubic phase that have correspondence

with those of the tetragonal structure appear to arise due to the breakdown of the Raman selection rule due to the substitutional disorder and compositional fluctuations.[24] The compositional dependence of total Raman intensity was found to decrease rapidly as x approaches tetragonal-cubic transition boundary. Persistence of Raman intensity in the cubic phase suggested that the symmetry-forbidden scattering is significant. From the dielectric behavior, a relaxor nature of cubic phase was found.[24]

In-situ X-ray diffraction measurements at high-temperature were carried out to study the structural stability of tetragonal BLF-PT solid-solution for x = 0.0, 0.2 and 0.3. X-ray diffraction patterns as a function of temperature were obtained using an Edmund Buhler high temperature attachment. The X-ray diffraction patterns were analysed to obtain the unit cell parameters. The lattice parameters for x = 0.0, 0.2 and 0.3 show similar behavior with temperature and the tetragonal-cubic transition is found to occur at 988, 773 and 618 K, respectively.[30] It was found that the decrease in the tetragonal anisotropy of BLF-PT upon La-doping is essentially responsible for the lowering of T_C. This data was used to construct a x-T phase diagram.

The Raman spectra of pure and La-substituted BF-PT samples were also studied at elevated temperature up to 873 K. The parameters of the Raman spectra such as peak positions, line-widths and intensities of the modes were obtained using multi-Lorenzians curve fitting. At elevated temperature the spectra broadened further and the intensities were found to reduce. Less number of modes at high temperature arise due to insufficient intensity of weak bands. From the temperature dependence of spectral parameters a signature of the tetragonal-cubic structural transition was found at 628 K for x = 0.3 consistent with the X-ray diffraction results.

At room temperature all samples were in a paramagnetic state. On the other hand, at 4 K the M-H curves for all compositions showed a hysteresis loop, which did not saturate up to applied field of 6 T. This suggested the existence of magnetically ordered clusters in an overall

paramagnetic host. Formation of magnetically ordered clusters in solid solutions has been reported in other systems also.[26] The remnant magnetization appears to depend on *x*. This has been argued to be due to the incorporation of La^{3+} in *A* site of BLF-PT leading to destruction of spiral modulated spin structure and hence Dzyaloshinskii-Moriya type interaction is enhanced.[31, 32] In order to understand the nature of magnetic ordering, temperature dependence of magnetization (ZFC and FC) was investigated at applied field of 1 kOe for all the samples. The magnetization was found to decrease with temperature and depended on the thermal history of the samples exhibiting irreversibility effect. The irreversible temperature T_{irr} was found to shift towards higher temperature with increasing La-composition. This was attributed to change in cooperative magnetic interaction of Fe^{+3}-O-Fe^{+3}, arising from crystallographic anisotropy.[26] For $x = 0.2$ sample, the ZFC magnetization shows a cusp at low temperature. This could be due to a spin glass behavior.[25, 33] From the behaviour of peak temperature as a function of applied field an Ising-type spin glass was concluded. From the *P*-*E* loop measurement, well defined hysteresis loops were observed with increasing La-composition. The remnant polarization was found to increase as a function of La-composition.[34]

The thesis is organised in six chapters. **Chapter 1** gives an introduction to the subject and chapter 2 presents the details of synthesis, characterization and experimental techniques. C**hapters 3, 4 and 5** discuss the experimental results on $NaNbO_3$, PZN-PT single crystal and BLF-PT ceramic samples respectively. **Chapter 6** summarises the thesis and conclusion drawn from present study are presented. In addition, directions for possible future studies are also pointed out.

Chapter 1 gives a brief introduction to the fascinating world of ferroelectric materials and their unique properties and applications. The phenomenon of structural phase transitions is discussed in detail. The recent literature is reviewed and the current understanding of the subject

is presented. C**hapter 2** contains the details of the synthesis procedures for polycrystalline ceramic samples and single-crystals, and the experimental techniques used for their investigations. The technique of Raman spectroscopy for probing the optical phonons and that of Brillouin spectroscopy for probing the acoustic phonons are described in detail. A brief discussion on the characterization tools, i.e. EDAX, X-ray diffraction, TEM, and SEM are also presented. **Chapter 3** presents results of low temperature Raman spectroscopic investigation on $NaNbO_3$. In addition, the study on central peak in $NaNbO_3$ single crystal for antiferroelectric ($D_{2h}^{11}, Z = 8$)-antiferroelectric ($D_{2h}^{13}, Z = 24$) phase transition using Brillouin scattering at elevated temperature is presented. In **Chapter 4**, the Brillouin and polarized Raman spectroscopic studies on PZN-PT system are discussed in the context of tetragonal-cubic phase transition and the dynamics of polar nano regions in the relaxor-cubic phase. In **Chapter 5**, a composition-driven tetragonal-cubic transition in La-substituted system BLF-PT for $0.0 \leq x \leq 0.5$ is discussed on the basis of X-ray diffraction and Raman scattering results. The temperature-driven tetragonal–cubic transition is identified using Raman and X-ray diffraction. The results of magnetic and ferroelectric ordering obtained using magnetization and polarization measurements as a function of tetragonal anisotropy and temperature are also presented. In **Chapter 6**, a summary of the results obtained, highlights of the inferences drawn and the conclusions arrived at are presented. Possible directions of future studies are also discussed in brief.

The significant new results presented in this thesis are:

1. Hysteresis and two-phase coexistence were determined across orthorhombic-rhombohedral transition in $NaNbO_3$ (hysteresis ~80 K, coexistence ~60 K).
2. Anomalies in the intensity of the central peak and relaxation time in $NaNbO_3$ single crystal suggest order-disordered nature of antiferroelectric ($D_{2h}^{11}, Z = 8$)-antiferroelectric ($D_{2h}^{13}, Z = 24$) transition at ~643 K using Brillouin technique.

3. The behavior of relaxation times obtained from LA phonon and central peak in PZN-PT single crystal in the relaxor-cubic phase suggests coupling between strain and polarization fluctuations.
4. Polarized Raman measurements on PZN-PT across tetragonal-cubic transition (473 K) exhibit anomalies in mode frequencies.
5. BLF-PT is found to undergo a tetragonal-cubic transition at $x \geq 0.4$.
6. A x-T phase diagram of BLF-PT is obtained for the first time.
7. Remnant polarization increases with doping x.
8. Large polarization and forbidden Raman scattering in the cubic phase is attributed to symmetry breaking due to formation of polar nano regions leading to relaxor behavior.
9. Magnetic hysteresis suggests ferromagnetic clusters embedded in paramagnetic host. For $x = 0.2$ system an Ising type spin glass behavior was found.
10. Evidence of tetragonal-cubic transition found at 618 K from T-dependence of mode frequencies in $x = 0.3$ BLF-PT.

References

1. G. A. Samara, Solid State Phys. **56**, 239 (2001).
2. Manfred Fiebig, J. Phys. D: Appl. Phys. **38**, R123 (2005).
3. W. Eerenstein, N. D. Mathur, and J. F. Scott, Nature **442**, 05023 (2006).
4. Nicola A. Hill, J. Phys. Chem. B **104**, 6694 (2000).
5. S. Gentil, G. Robert, N. Setter, P. Tissot, and J.-P. Rivera, Jpn. J. Appl. Phys. **39**, 2732 (2000).
6. V. Sivasubramanian, V. R. K. Murty, B. Viswanathan, and M. Sieskind, J. Phys.: Condens. Matter **8**, 2447 (1996).
7. K. K. Mishra, V. Sivasubramanian, and A. K. Arora, J. Raman Spectrosc. **42**, 517 (2011).
8. C. N. W. Darlington and H. D. Megaw, Acta Cryst. B**29**, 2171 (1973).
9. Z. X. Shen, X. B. Wang, M. H. Kuok, and S. H. Tang, J. Raman Spectrosc. **29**, 379 (1998).
10. S. K. Mishra, N. Choudhury, S. L. Chaplot, P. S. R. Krishna, and R. Mittal, Phys. Rev. B **76**, 024110 (2007).
11. M. E. Lines and A. M. Glass 1977 *Principles and Applications of Ferroelectrics and Related Materials* (Oxford: Clarendon).
12. W. Cochran, Phys. Rev. Lett. **3**, 412 (1959).
13. A. Hushur, S. Gvasaliya, B. Roessli, S. Lushnikov, and S. Kojima, Phys. Rev. B **76**, 064104 (2007).
14. E. Bouziane, M. D. Fontana, and M. Ayadi, J. Phys.: Condens. Matter **15**, 1387 (2003).
15. D. Viehland, J. F. Li, S. J. Jang, L. E. Cross, and M. Wuttig, Phys. Rev. B **46**, 8013 (1992).
16. S. -E. Park and T. R. Shrout, J. Appl. Phys. **82**, 1804 (1997).

17. D. E. Cox, B. Noheda, G. Shirane, Y. Useu, K. Fujishiro, and Y. Yamada, Appl. Phys. Lett. **79**, 400 (2001).

18. A. A. Bokov and Z.-G. Ye, J. Mater. Sci. **41**, 31(2006).

19. L. E. Cross, Ferroelectrics **76**, 241 (1987).

20. D. La-Orauttapong, B. Noheda, Z.-G. Ye, P. M. Gehring, J. Toulouse, D. E. Cox, and G. Shirane, Phys. Rev. B **65**, 144101 (2002).

21. S. Tsukada, Y. Ike, J. Kano, T. Sekiya, Y. Shimojo, R. Wang, and S. Kojima, Appl. Phys. Lett. **89**, 212903 (2006).

22. S. Tsukada, Y. Ike, J. Kano, T. Sekiya, Y. Shimojo, R. Wang, and S. Kojima, J. Phys. Soc. Jpn. **77**, 033707 (2008).

23. S. Tsukada and S. Kojima, Phys. Rev. B **78**, 144106 (2008).

24. K. K. Mishra, V.Sivasubramanian, R. M. Sarguna, T. R. Ravindran, and A.K. Arora, J. Solid State Chem. **184**, 2381 (2011).

25. R. Martinez, R. Palai, H. Huhtinen, J. Liu, J. F. Scott, and R. S. Katiyar, Phys. Rev. B **82**, 134104 (2010).

26. W.-M. Zhu, H.-Y. Guo, and Z.-G. Ye, Phys. Rev. B **78**, 014401 (2008).

27. J. Cheng, S. Yu, J. Chen, and Z. Meng, Appl. Phys. Lett. **89**, 122911 (2006).

28. A. Singh, A. Gupta, and R. Chatterjee, Appl. Phys. Lett. **93**, 022902 (2008).

29. M. Gruyters, Phys. Rev. Lett. **95**, 077204 (2005).

30. K. K. Mishra, R.M. Sarguna, S. Khan, and A.K. Arora, AIP Advances **1**, 032126 (2011).

31. A. S. Bborovik-Romanov, Sov. Phys. JETP **11**, 786 (1960).

32. I. Sosnowska, R. Przenioslo, P. Fischer, and V. A. Murashov, J. Magn. Magn. Mater. **160**, 384 (1996).

33. R. Palai, H. Huhtinen, J. F. Scott, and R. S. Katiyar, Phys. Rev. B **79**, 104413 (2009).

34. K. K. Mishra, A. T. Satya, A. Bharathi, V. Sivasubramanian, V. R. K. Murthy, and A. K. Arora, J. Appl. Phys. **110**, 123529 (2011).

Contents

Certificate ii

Acknowledgments vi

List of Publications viii

Synopsis x

1 Introduction 1

1.1 Ferroelectricity 1

1.1.1 Relaxor ferroelectrics 4

1.1.2 Multiferroic materials 7

1.2 Perovskite structure 9

1.3 Phase transitions 10

1.3.1 Thermodynamic classification of phase transitions 11

1.3.2 Ferroelectric phase transitions 12

1.3.3 Order parameter of a ferroelectric phase transition 13

1.3.4 Different types of ferroelectric transition 14

1.3.5 Hysteresis in phase transitions 15

1.4 Experimental techniques for studying ferroelectric phase transitions 15

1.5 Scope of present thesis 16

1.6 Summary 18

References 19

2 Experimental details 24

2.1 Synthesis 24

2.1.1 Solid state reaction 24

2.1.2 Single crystal:Growth by flux method 25

2.1.3 Synthesis parameters for samples synthesized for present studies 26

2.2 Experimental techniques 28

2.2.1 Raman scattering 28

2.2.2 Quantum theory of Raman scattering 28

2.2.3 Brillouin scattering 31

2.3 Raman scattering set ups 32

2.3.1 SPEX Raman spectrometer 32

2.3.2 Renishaw *micro*-Raman spectrometer 34

2.4 Brillouin scattering set up 36

2.4.1 Fabry-Perot Interferometer 36

2.4.2 Tandem Interferometer 36

2.4.3 3+3-pass tandem Fabry-Perot Interferometer 38

2.4.4 Brillouin spectrometer 38

2.5 X-ray diffraction technique 40

2.6 Transmission electron microscopy 41

2.7 Scanning electron microscopy 42

2.8 Dielectric spectroscopy 42

2.9 Vibrating Sample Magnetometer (VSM) 43

References 44

3 Raman and Brillouin spectroscopic studies on phase transition in ferroelectric $NaNbO_3$ 45

3.1 Introduction 45

3.2 Experimental details 48

3.3 Results and discussion 49

3.3.1 Structural and microstructural characterization 49

3.3.2 Low temperature Raman spectroscopic results 50

3.3.3 Brillouin spectroscopic results on $NaNbO_3$ single crystal 58

3.4 Summary and conclusions 65

References 67

4 Brillouin and Raman spectroscopic studies on phase transition in relaxor Ferroelectric PZN-PT single crystal 70

4.1 Introduction 70

4.2 Experimental details 73

4.3 Results and discussion 74

4.3.1 Structural and dielectric studies 74

4.3.2 Brillouin spectroscopic results 77

4.3.3 Raman spectroscopic results 87

4.3.4 Summary and conclusions 95

References 96

5 Vibrational, structural, and magnetic properties of multiferroic $BLFPT_x$ 101

5.1 Introduction 101

5.2 Experimental details 103

5.3 Results and discussion 105

5.3.1 Microstructural and structural properties 105

5.3.2 Raman Scattering at ambient from La-substituted $BiFeO_3$-$PbTiO_3$ 108

5.3.3 *in-situ* X-ray diffraction at high temperature 116

5.3.4 *in-situ* Raman Scattering from $BLFPT_x$ at high temperature 120

5.3.5 Magnetic behaviour of $BLFPT_x$ 129

5.3.6 Ferroelectric properties 134

5.4 Summary and conclusions 135

References 137

6 Summary and conclusions 141

6.1 Summary 141

6.2 Conclusions 143

6.3 Directions for future studies 144

References 146

LIST OF FIGURES

		Page No.
Figure 1.1	Schematic *P-E* diagram of a ferroelectric material.	1
Figure 1.2	Properties of normal ferroelectric (a) hysteresis loop, (b) spontaneous polarization, and (c) dielectric response.	2
Figure 1.3	Temperature dependence of the real and imaginary parts of the relative dielectric permittivity in relaxor.	5
Figure 1.4	Properties of relaxor ferroelectric (a) hysteresis loop, (b) spontaneous polarization, and (c) dielectric response.	6
Figure 1.5	Schematic presentation of PNRs in relaxors.	7
Figure 1.6	ABO_3 Perovskite structure displaying BO_6 octahedron.	9
Figure 1.7	Schematic temperature dependence of the free energies of the two competing phases of a crystal.	11
Figure 1.8	Temperature dependence of P and inverse of susceptibility (χ) for first and second order phase transitions.	13
Figure 1.9	Evolution of free energy versus P with temperature for first and second order phase transitions.	14
Figure 2.1	Steps involved in solid state reaction.	25
Figure 2.2	Schematic configuration used for sintering of samples.	27
Figure 2.3	Schematic presentation of (a) creation (Stokes) and (b) annihilation (anti-Stoke) of phonon.	29
Figure 2.4	Schematic representation of phonon dispersion branches.	31
Figure 2.5	Block diagram of SPEX Raman spectrometer.	33

Figure 2.6	Schematic diagram of Renishaw *micro*-Raman spectrometer.	34
Figure 2.7	Principle of the tandem FPI scan.	37
Figure 2.8	Alignment optics.	39
Figure 2.9	Tandem optics.	39
Figure 2.10	(a) Optical system used for alignment in the reflection mode, (b) Reflected intensity for imperfectly aligned FP1 and FP2, and (c) Reflected intensity after alignment.	40
Figure 3.1	X-rays diffraction pattern of $NaNbO_3$.	50
Figure 3.2	Raman spectra of $NaNbO_3$ at various temperatures during the cooling cycle.	51
Figure 3.3	Raman spectra of $NaNbO_3$ at various temperatures during the heating cycle.	51
Figure 3.4	Temperature dependence of Raman modes during cooling cycle for (a) low- and (b) high-wavenumber region.	54
Figure 3.5	Temperature dependence of Raman modes during heating cycle for (a) low- and (b) high-wavenumber region.	54
Figure 3.6	Temperature dependence of the integrated intensity of modes at (a)60, (b) 123, (c) 182, (d) 274, and (e) 556 cm^{-1}.	56
Figure 3.7	(a) X-rays diffraction pattern of $NaNbO_3$ single crystal powder at ambient (b) Laue pattern on single crystal.	59
Figure 3.8	Brillouin spectra of $NaNbO_3$ measured using a FSR of 3300 GHz at selected temperatures.	60
Figure 3.9	Brillouin spectra fitted to a sum of damped harmonic oscillators and a Debye relaxation mode at selected	61

temperatures (a) 573K, (b) 623 K and (c) 693 K.

Figure 3.10 Temperature dependence of optical phonon frequencies and their line-widths (a) mode-1, (b) mode-2, and (c) Integrated intensities of CP and mode-1 as a function of temperature. 62

Figure 3.11 (a) The relaxation time τ and (b) the inverse relaxation time υ_r as a function of temperature. 64

Figure 3.12 Logarithmic relaxation time (τ) versus 1/*T*. The solid line is the fit using hopping model. 65

Figure 4.1 Powder X-rays diffraction pattern of PZN-PT crystal (*x* = 0.15). 74

Figure 4.2 Temperature dependence of the dielectric constant (ε_r) of PZN-PT single crystal measured at different frequencies. 75

Figure 4.3 Temperature dependence of the inverse of dielectric constant ($1/\varepsilon_r$) and its *T*-derivative (ξ) at 100 kHz. 76

Figure 4.4 (a) Brillouin spectra of PZN-PT measured using a FSR of 100 GHz at selected temperatures (b) Fitted spectrum at 363 K. 77

Figure 4.5 Temperature dependences of Brillouin shift and FWHM of the LA phonon mode. 78

Figure 4.6 Temperature dependences of (a) the intensity of LA phonon mode, and temperature derivative of the LA phonon mode (b) FWHM and (c) frequency. 79

Figure 4.7 (a) Brillouin spectra of PZN-PT measured using a FSR of 400 GHz at selected temperatures (b) Fitted spectrum at 523 81

K.

Figure 4.8 Temperature dependences of FWHM and the intensity of (a) narrow-CP and (b) broad-CP. 83

Figure 4.9 Temperature dependences of the relaxation time (τ_{LA}) and the relaxation times (τ_{ncp} and τ_{bcp}) determined from CPs. 83

Figure 4.10 Plot of $1/\tau_{bCP}$ as a function of temperature $(T-T_{tc})/T_{tc}$. 85

Figure 4.11 Temperature dependences of the integrated intensities of bCP in unpolarized and depolarized geometries. 87

Figure 4.12 Raman spectra at various temperatures in (a) unpolarized and in (b) VV and (c) VH polarized geometries. 88

Figure 4.13 Examples of multiple peak decomposition of Raman spectra in VV geometry at (a) 298 K and (b) 713 K. 90

Figure 4.14 Examples of multiple peak decomposition of Raman spectra in VH geometry at (a) 298 K and (b) 713 K. 90

Figure 4.15 Dependence of Raman mode frequencies on temperature in (a) VV and (b) VH geometries. 92

Figure 4.16 Temperature dependence of FWHM of 273 cm^{-1} mode in VV geometry. 93

Figure 5.1 EDAX spectra of $BLFPT_x$ for x = (A) 0.0, (B) 0.2, (C) 0.4, and (D) 0.5. 106

Figure 5.2 X-rays diffraction patterns of $BLFPT_x$ ($0 \leq x \leq 0.5$). 107

Figure 5.3 Lattice parameters (c and a) as a function of composition in $BLFPT_x$ ($0 \leq x \leq 0.5$). 108

Figure 5.4 (a) Raman spectra of $BLFPT_x$ at 300 and 77 K (For x = 0.0) 108

(b) Raman spectra for 0 2 ≤ x ≤ 0.5 at ambient.

Figure 5.5 Raman spectrum fitted to sum of 7 Lorenzian peaks for x = 0.4 composition. 111

Figure 5.6 Dependence of normalized integrated intensity on La-composition. 113

Figure 5.7 Temperature dependence of real part of relative dielectric permittivity at various frequencies for x = 0.5. 114

Figure 5.8 Dependence of Raman mode frequency on La-composition. 115

Figure 5.9 Dependence of mode splitting on *c/a* ratio. 116

Figure 5.10 X-rays diffraction patterns of $BLFPT_x$ powders measured at different temperatures. 117

Figure 5.11 Diffraction patterns, expanded in the 2θ regions, for x = 0.0 at elevated temperatures; (a) (001)-(100) doublet and (b) (101)-(110) doublet. 118

Figure 5.12 Variation of the *c* and *a* lattice parameters as a function of temperature; (a) x = 0.0, (b) x = 0.2, and (c) x = 0.3. 119

Figure 5.13 x-T phase diagram of the tetragonal $BLFPT_x$ solid-solution. 120

Figure 5.14 Raman spectra of $BLFPT_x$ at 83 K (a) for 0 ≤ x ≤ 0.5. (b) Fitted spectrum for x=0.0. (c) Fitted spectrum for x = 0.5. 122

Figure 5.15 Temperature evolution of Raman spectra of $BLFPT_x$ for, (a) x = 0.0, (b) x = 0.3, and (c) x = 0.5. 123

Figure 5.16 Raman spectrum fitted to sum of Lorenzian peaks for x = 0.0, (a) at 298 K and (b) at 673 K. 124

Figure 5.17 Dependence of Raman mode frequencies on temperature for, 127

(a) x = 0.0, (b) x = 0.2, (c) x = 0.3, (d) x = 0.4, and (e) x = 0.5.

Figure 5.18 Dependence of Raman line-widths on temperature for x = 0.3. 128

Figure 5.19 Magnetic hysteresis loop of $BLFPT_x$ (a) for x = 0.0 at 4 K, (b) for x = 0.5 at 4 K, and (c) for x = 0.5 at different T. 130

Figure 5.20 Dependant of FC and ZFC magnetization of $BLFPT_x$ at 1 kOe (a) for x = 0.2 (b) x = 0.3, and (c) x = 0.4. 131

Figure 5.21 (a) ZFC curves of $BLFPT_x$ x = 0.2, in different applied magnetic fields (b) $H^{2/3}$ versus T_g, fits to A-T critical line and (c) H^2 versus T_g, does not fit to G-T critical line. 132

Figure 5.22 Variation of c/a ratio for $BLFPT_x$ ($0 \leq x \leq 0.5$) with x. 134

Figure 5.23 (a) P-E loop of $BLFPT_x$ ($0 \leq x \leq 0.5$) at ambient temperature and (b) Effect of La-composition on the remanent polarization. 135

LIST OF TABLES

		Page No.
Table 1.1	Properties and applications of Perovskites.	10
Table 3.1	Wavenumbers of Raman bands at room temperature and 10 K.	53
Table 4.1	Raman mode frequencies in PZN-PT single crystal (x = 0.15) in different polarization configurations.	91
Table 5.1	Compositional dependence of grain size, relative density and tetragonal-cubic transition temperature for $BLFPT_x$.	105
Table 5.2	Mode frequencies of the Raman bands in for $BLFPT_x$ x = 0 and 0.5.	109
Table 5.3	Correlation diagram between irreducible representations of the C_{4v} (tetragonal) and O_h (cubic) point groups.	112
Table 5.4	Mode frequencies in $BLFPT_x$ ($0 \leq x \leq 0.5$) at 83 K.	121

Chapter 1

Introduction

1.1 Ferroelectricity

In a ferroelectric crystal the centre of positive charge does not coincide with the centre of negative charge and hence exhibits an electric dipole moment even in the absence of an external electric field.[1] Out of the 32 possible crystal classes (point groups) 11 are centrosymmetric and therefore can not exhibit polar properties. The remaining 21 crystal classes do not possess a centre of symmetry and thus can retain one or more polar axes. Out of these, 20 crystal classes are piezoelectric. Among these piezoelectric classes, 10 have a unique polar axis and therefore are spontaneously polarized. Crystal belonging to these 10 classes are pyroelectric. Ferroelectric crystals belong to the pyroelectric family, but they exhibit the unique properties, i.e. the direction of the spontaneous polarization (*P*) can be reversed by the application of an electric field (*E*). The key features of the ferroelectric crystals are (a) reversibility of the polarization and (b) existence of a hysteresis loop (Fig. 1.1).

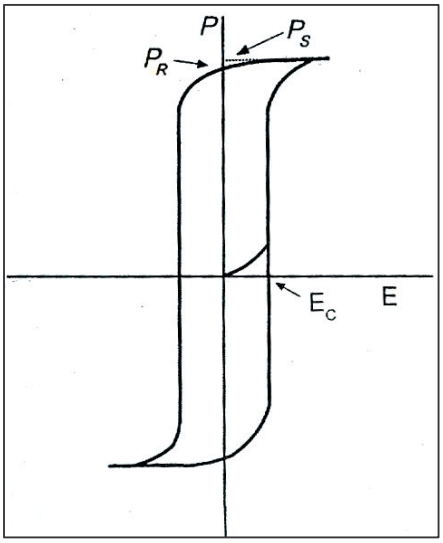

Figure 1.1 Schematic *P-E* diagram of a ferroelectric material exhibiting a hysteresis loop.

The direction of the polarization is not the same throughout the macroscopic dimension of a crystal. It is energetically more favorable for the crystal to have regions or domains, which are macroscopic regions of homogeneous polarization. In adjacent domains, the

polarization is in different direction. The dielectric constant (ε) and dielectric susceptibility (χ) are defined as the slope of the electric displacement *D vs*. *E* and *P vs*. *E* curves, respectively, at the origin.[2]

$$\varepsilon = \left(\frac{\partial D}{\partial E}\right)_{E=0} \qquad \text{and} \quad \chi = \left(\frac{\partial P}{\partial E}\right)_{E=0}$$

The general characteristic features of ferroelectric crystals are listed below.

- The hysteresis loop disappears at a certain temperature, the Curie temperature T_C, above which the crystal behaves as paraelectric.
- At T_C a ferroelectric crystal transforms to a phase of higher symmetry. In general, the high temperature phase is non-polar, or paraelectric.
- The polar crystal structure of a ferroelectric can be derived from the high temperature paraelectric structure by a slight distortion of the crystal lattice.
- In general, ferroelectrics have a large ε and χ, which rise to a maximum at T_C.
- Above T_C, ε obeys the Curie-Weiss law $\varepsilon = \dfrac{C}{T - T_O}$, where C and T_O are the Curie-Weiss constant and Curie-Weiss temperature, respectively.

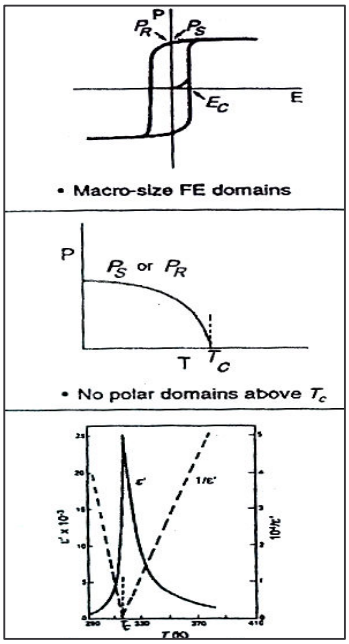

Figure 1.2 represents properties of normal ferroelectric (a) hysteresis loop, temperature dependence of (b) spontaneous polarization, and (c) dielectric response (Samara)[2].

Different theories have been put forth to describe the physical properties and the mechanism of ferroelectricity. Those theories are outlined below in brief.

(a) Phenomenological theory (Landau theory)

Many of the physical properties of ferroelectrics in the transition region can be correlated and interpreted successfully with this theory.[3, 4] To describe both the ferroelectric and paraelectric phases same free energy function is used. This assumption is based on the basis of the structure of the polar phase derived from that of the paraelectric phase by a slight distortation of the lattice. However, this theory does not describe the physical mechanism responsible for ferroelectricity. The Landau theory will be discussed later in section 1.3.3.

(b) Soft mode theory

Cochran[5] was first to introduce the concept of soft phonons and discussed in detail the mechanism of displacive ferroelectric phase transitions. A soft phonon mode means a mode whose frequency decreases and vanishes (for a second-order phase transition) at T_C. The decrease and ultimate vanishing of the frequency of the soft mode as the transition is approached is caused by cancellation between competing forces (short-range and long-range Coulombic forces). The soft mode frequency ω_S is related with temperature as $\omega_S{}^2 = K(T - T_C)$, where K is a positive constant, and T_C is the transition temperature. The temperature dependence of ω_S is responsible for the observed Curie-Weiss temperature dependence of the dielectric constant ε and for the divergence of ε at the transition. In this case, both ε and ω_S are related by the Lyddane-Sachs-Teller relation, i.e. $\varepsilon(T)\omega_S{}^2(T) = \text{constant}$. The soft mode theory has been extensively used in the analysis and interpretation of ferroelectric properties and understanding the mechanism in the case of displacive transitions.

(c) First-principle theory

In the ABO_3 type ferroelectric Perovskites, the microscopic origin of ferroelectricity is addressed by first-priciple theory. For instance, ferroelectric compounds such as $KTaO_3$ and $KNbO_3$ possess different ferroelectric behavior although the Ta and Nb ions have comparable ionic sizes and same valency. This type of differences of ferroelectric behaviors is understood by the first-principle electronic structure and total energy calculation. The major challenge in this approach is to calculate the finite temperature ferroelectric properties and to study the more complex mixed-Perovskites.[6]

1.1.1 Relaxor ferroelectrics

Relaxor ferroelectrics were discovered almost 50 years ago among the complex oxides with Perovskite structure. In recent year this field of research has experienced a revival of interest. Relaxors exhibit very large dielectric constant, exceptionally large electrostrictive coefficients and large electro-optic constants. Because of these properties relaxors are used in capacitors, actuators, micro-positioners, information storage, shutters and in optical modulators. Therefore, this class of materials is one of the most active current research areas of ferroelectricity.[7]

The disordered distribution of different ions on the equivalent lattice sites, i.e. compositional disorder, also known as chemical, ionic and substitutional disorder, is the essential feature of a relaxor. In ABO_3 oxides, substituting ions of different sizes, valences and polarizabilities at both *A* and *B* lattice sites produces dipolar defects and can introduces a sufficiently high degree of disorder. These disorders cause breaking translational symmetry and prevent the formation of a long-range ordered state.[2] The relaxor behaviour was first observed in the Perovskites with disorder of non-isovalent ions, including the stoichiometric complex Perovskite compounds, e.g. $Pb(Mg_{1/3}Nb_{2/3})O_3$(PMN)[8] or $Pb(Sc_{1/2}Ta_{1/2})O_3$[9] in which Mg^{2+}, Sc^{3+}, $Ta^{5+}$and Nb^{5+} ions are fully or partially disordered in the *B*-sublattice of the Perovskite structure. Recent studies have shown that many homovalent solid solutions, e.g. $Ba(Ti_{1-x}Zr_x)$[10, 11] and $Ba(Ti_{1-x}Sn_x)$[12] can also exhibit relaxor behaviour. Other examples of

relaxor feroelectrics are complex Perovskites solid-solutions of $Pb(Mg_{1/3}Nb_{2/3})O_3$-$PbTiO_3$[13] and $Pb(Zn_{1/3}Nb_{2/3})O_3$-$PbTiO_3$[14, 15]etc.

Relaxor ferroelectrics exist in a non-polar paraelectric (PE) phase at high temperature, which is similar to the PE phase of normal ferroelectrics. Upon cooling they transform into the ergodic relaxor (ER) in which polar regions of nanometer scale with randomly distributed directions of dipole moment appear below the Burns temperature (T_B). This transformation can not be considered a structural phase transition because it is not accompanied by any change of crystal structure on the macroscopic scale. However, the dymanics of polar nano regions (PNRs) affect the behaviour of the crystal significantly. Therefore, the state of the crystal at $T < T_B$ is often considered as the new phase different from the paraelectric one. Upon lowering T further below T_B, the dynamics of PNRs slow down enormously and at a temperature, T_F, the PNRs become frozen into a non-ergodic state. Freezing of the dipole dynamics is associated with a large and broad peak in the temperature dependence of the dielectric constant (ε) along with a characteristic dispersion with frequencies (Fig. 1.3).

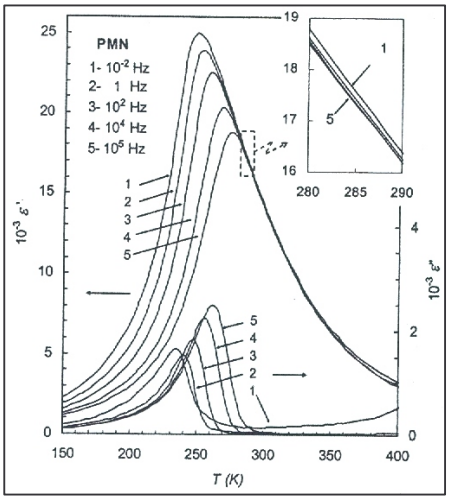

Figure 1.3 Temperature dependence of the real and imaginary parts of the relative dielectric permittivity measured at different frequencies in relaxor (Bokov and Ye).[13]

The relaxors are also called "ferroelectrics with diffuse phase transition" even though no transition into a ferroelectric phase really occurs because of the diffuseness of the dielectric anomaly. The non-ergodic freezing state existing below T_F can be irreversibly transformed into a ferroelectric state by a strong enough external electric field. Upon heating the FE phase transforms to the ergodic phase at the temperature T_C, close to T_F. In many relaxors the

spontaneous phase transition from ergodic relaxor into a low temperature ferroelectric phase occurs at T_C[16] and hence the non-ergodic state does not exist. The general characteristic properties of relaxor ferroelectrics are summarized below.

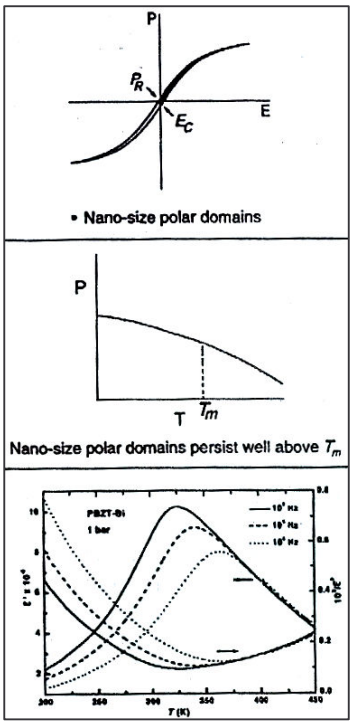

Figure 1.4 represents properties of relaxor ferroelectric (a) hysteresis loop, temperature dependence of (b) spontaneous polarization, and (c) dielectric response (Samara)[2].

- The P-E hysteresis loop exhibits slim-loop as shown in Fig. 1.4. For sufficiently high electric fields the nano-domains of the relaxor can be oriented along the field leading to large polarization; however, upon removing the field most of these domains reacquire their random orientations resulting in a small remanent polarization P_r.
- The field-induced polarization of relaxor decreases smoothly across the dynamic transition temperature T_C and retains finite values up to rather high temperatures due to the fact that polar nano-domains persist up to well above T_C.
- It exhibits a very broad $\varepsilon(T)$ peak and strong frequency dispersion in the peak parameter (T_C) and in the magnitude of ε below T_C.

- $\varepsilon(T)$ of a relaxor exhibits a deviation from the curie-Weiss law for temperatures of few 10s to 100s degree above T_C. At still higher temperatures, linear 1/ε *vs*. *T* response is observed.
- There is no structural phase transition across T_C in a relaxor. The peak in $\varepsilon(T)$ is simply a manifestation of the slowing down of the dipolar motion below T_B.

Origin and evolution of PNRs

The existence of PNRs in relaxors is well established[2, 13]. However, the cause and mechanism of their formation are not well understood. There exist different approaches to explain the formation of PNRs. These can be divided into two categories. In the first category[17, 18-21]the models consider the PNRs as a result of local "phase transitions" so that the crystal consists of nanosize polar islands embedded into a cubic matrix in which the symmetry remains unchanged (Fig. 1.5). On the other hand, the models of second category assume that the transition to occur in all regions of the crystal and the crystal consists of low-symmetry nanodomains separated by the domain walls but not by the regions of cubic symmetry.[22-25] Both these situations can hardly be distinguished experimentally from structural examinations[26] due to the fact that the local symmetry of cubic matrix is not expected to be cubic and the thickness of domain walls is comparable with size of nanodomains.

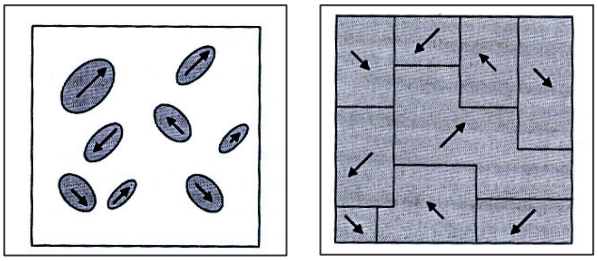

Figure 1.5 Schematic presentation of PNRs in relaxors

The experimental evidence for the existence of PNRs was obtained from the studies of the temperature dependences of the optical index of refraction,[27] elastic diffuse neutron and X-ray scattering around the reciprocal lattice points[28-31] and transmission electron microscopy.[32]

1.1.2 Multiferroic materials

Multiferroic materials[33, 34] with coexistence of at least two ferroic order (Ferroelectric, Ferromagnetic, Ferroelastic) have drawn increasing attention due to their potential for applications[35] as multifunctional devices. The classification of multiferroics has been extended to include antiferroic ordering also.[36] However, as a matter of trend, the materials which have both spontaneous magnetic and electrical ordering simultaneously are termed as 'multiferroic'.[37]In this class of materials, the coupling interaction between the different order parameters produce a new effect, called as magnetoelectric (ME) effect.[38-40] The magnetoelectric response is the influence of electric field on the magnetization and/or the influence of magnetic field on the electric polarization of the material.[36]Magnetoelectricity has been observed as an intrinsic effect in some systems at low temperature, which has been under intensive study.[41-43] This has opened a number of new applications such as switching of magnetic memory elements by electric fields.[44] In addition, the ME effect of the multiferroics is effectively utilized for potential applications in information storage, spintronics,[45, 46]and sensors.[47]

There have been only a few magnetic-ferroelectric compounds due to the so called "d^0 vs. d^n problem". This is because the ferroelectric materials have transition metal ions with empty d-shell (e.g. Ti^{4+} ions in $PbTiO_3$), whereas the ferro-, feri- and antiferro-magnetic materials require the presence of (3d) transition ions with partially filled d-shells.[48] However, against this well known scarcity of the magnetic ferroelctrics, incase of ABO_3 type perovskite oxide, the stereo-chemically active $6S^2$ lone pair electrons of Pb^{2+} (and Bi^{3+}) ions in the *A*-site offer an alternate way to get the ferroelectric ordering irrespective of the kind of (magnetic) ions present in the *B*-site.[48] A few examples of compounds such as $BiFeO_3$, $BiMnO_3$, Bi_2FeCrO_6 etc belong to this category.[49, 50]

In this context, rhombohedral $BiFeO_3$ (BF) is unique among other multiferroic materials due to the coexistence of two types of long-range order: antiferromagnetic order below the Neel temperature T_N = 643 K and the ferroelectric order below Curie temperature T_C

= 1100 K.[51, 52] However, the compound was not found to show the magnetoelectric effect, as an spiral modulated spin structure led to disappearance of overall magnetization.[53] In addition, the electric polarization was also found to be quite low.[54, 55] Furthermore, the synthesis of ideal Perovskite phase of pure BF is difficult because of comparable thermodynamic stability of Fe^{3+} and Fe^{2+} states of iron in this compound.[56, 57] In order to overcome these limitations, several solid-solutions have been synthesized and their properties investigated. The solid-solutions of BF with other ABO_3 compounds such as $PbTiO_3$ (PT), $PrFeO_3$ and $BaTiO_3$ stabilize the Perovskite phase and exhibit spontaneous magnetization.[58-63]

1.2 Perovskite structure

A great deal of attention has been paid to ABO_3 Perovskite oxides due to their excellent physico-chemical properties and wide range of applications. Some of the applications are listed in table 1.1. In an ideal Perovskite (ABO_3) structure, *A*-site cations occupy the corners of the cube, while *B*-site cations sit in the body center and the oxygen atoms occupy on the face centers. *A*-site could be accommodated with monovalent (Na, K etc.) divalent (Ca, Sr, Ba, Pb etc.) or trivalent (La) and *B*-site could be pentavalent (Nb, Ta etc.), tetravalent (Ce, Ti etc.), or trivalent (Mn, Fe etc.). The co-ordination number of *A*-site cation is 12 whereas that for the *B*-site cation is 6.[64]

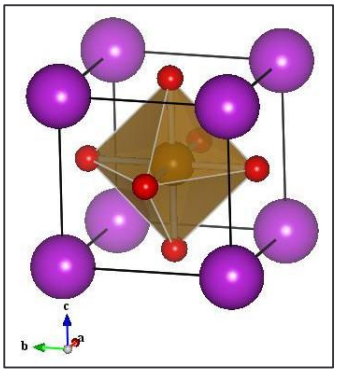

Figure 1.6 ABO_3 Perovskite structure displaying BO_6 octahedron.

The ideal Perovskite structure is cubic, but often the real structure deviates from the cubic structure. The degree of distortion in the Perovskite materials is found from the Goldschmidt

tolerence factor $t = \frac{r_A + r_O}{\sqrt{2}(r_B + r_O)}$, where r_A, r_B and r_O are the ionic radii of *A*, *B* and O ions respectively. In case of ideally packed Perovskite structure t has a value 1. The Perovskite structure occurs only within the t-range 0.75 to 1 where the cationic radii should be $r_A > 0.90$ Å and $r_B > 0.51$ Å.[65] Three structural degrees of distortions from the ideal Perovskite structure are considered to be possible from the point of view of topological and geometrical constraints. Those degrees of freedom are (i) displacement of *A*-site and *B*-site cations from the centers of the polyhedra, (ii) distortations of the anion octahedral and (iii) tilting of the BO_6 octahedra.[66, 67] Octahedral tilting is a more common distortation mechanism that can be realized by tilting the rigid BO_6 octahedra while maintaining their corner sharing connectivity.[68-70] This type of distortation is generally observed when the *A*-site cation is too small for the cubic BO_6 corner sharing octahedral network.

Table 1.1 Properties and applications of Perovskites

Property	Applications
Dielectric	Multilayer capacitor, dielectric resonator, Thin film resistor
Optical	Electro optical modulator, Laser host, switch
Ferroelectric/piezoelectric	Piezoelectric transducers, P. T. C. thermister, electrostrictive actuators
Magnetic	Magnetic bubble memory, Ferromagnet
Ionic/proton conducting	Solid-electrolyte, hydrogen sensor

1.3 Phase transitions

A unique structure of matter which is stable is called as a phase. The stable structure or phase possessed by a solid at a given temperature and pressure (and at given values of other control parameters such as electric field and magnetic field etc.) can be understood in terms of its thermodynamic free energy. A stable phase has the lowest free energy.[64] The temperature

dependence of the free energies of two competing phase of a crystal is schematically shown in Fig. 1.7. For $T > T_C$, phase-I has a lower free energy than phase-II and is therefore more stable. For $T < T_C$, phase-II has a lower free energy and is stable. The two free energy curves intersect at transition point T_C. A solid undergoes a phase transition when a particular phase of the solid becomes unstable under a given set of thermodynamic conditions.

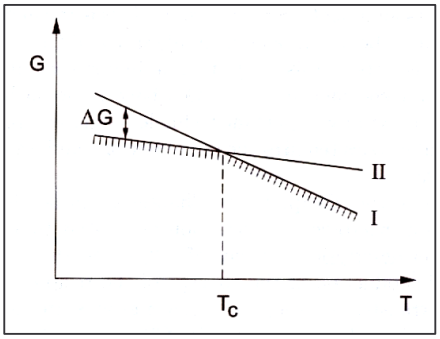

Figure 1.7 Schematic presentation of temperature dependence of the free energies of the two competing phases (I and II) of a crystal.

1.3.1 Thermodynamic classification of phase transitions

The free energy of the system remains continuous while thermodynamic quantities such as entropy, volume, heat capacity etc. undergo discontinuous changes during a phase transition. Ehrenfest[71] classified phase transitions by taking into account the relation between the free energy function and the thermodynamic quantity exhibiting discontinuity. The order of derivative of the free energy which shows a discontinuous change at the transition is the order of the phase transition. Gibbs free energy G is given in terms of pressure and temperature as,

$$G = U + PV - TS$$

The first derivative of the free energy with respect to P and T are:

$$\left(\frac{\partial G}{\partial P}\right)_T = V \qquad \left(\frac{\partial G}{\partial T}\right)_P = -S$$

The second derivatives of the free energy are

$$\left(\frac{\partial^2 G}{\partial P^2}\right)_T = \left(\frac{\partial V}{\partial P}\right)_T = -V\beta, \qquad \left(\frac{\partial^2 G}{\partial T^2}\right)_P = -\left(\frac{\partial S}{\partial T}\right)_P = -\frac{C_P}{T}$$

Here, β and C_P are the compressibility and heat capacity respectively.

First order phase transition – The transition in which a discontinuous change occurs in volume and entropy (latent heat of transformation involved). First-order phase transitions in solids are associated with latent heats, discontinuities in volume and changes in structure at the transition and leading to the Clapeyron-Clausius equation $\left(\frac{dP}{dT}\right) = \frac{\Delta S}{\Delta V} + \frac{\Delta H}{T\Delta V}$. Change in crystal symmetry along with latent heat effect could be taken as a necessary criterion for a first-order transition. The symmetry of the two phases is not related in this order of transition.

Second order phase transition – The transition in which a discontinuous change occurs in heat capacity (C_P) and compressibility (β). Transitions belonging to second-order are almost always associated with some kind of disordering process.[72] The symmetry of the two phases are related in second-order transition.

1.3.2 Ferroelectric phase transitions

In case of ferroelectrics, there is a long-ranged cooperative interaction of the spontaneous polarization, generally extending over macroscopic distances. This interaction, or ordering, exists in opposition to the depolarizing fields and the thermal disordering processes, up to a temperature T_C, above which the disordering forces overcome the ordering forces. When this situation occurs, a ferroelectric phase transition takes place. Furthermore, the disordered phase has higher point-group symmetry. Upon cooling, crystal with such a phase, splits into domains to minimize the overall depolarizing field and undergo a ferroelectric phase transition. In typical ferroelectrics, the spontaneous polarization decreases as temperature increases and it goes to zero continuously or discontinuously at T_C. Hence spontaneous polarization is considered as the order parameter of the transition. The behavior of the order parameter at T_C depends on the order of the phase transition. There is an abrupt drop in order parameter to zero at T_C for the first-order transition. For the second order transition, the order parameter goes to zero continuously at T_C. Figure 1.8 shows typical variation of order parameter with temperature for the first and second order phase transition at zero field.

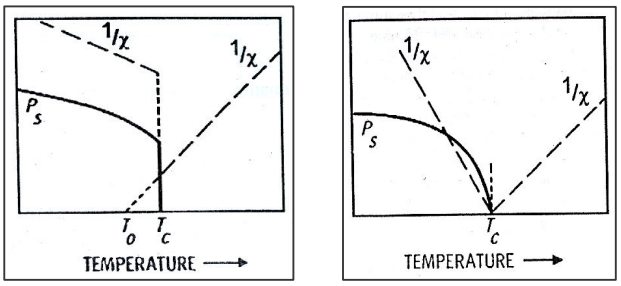

Figure 1.8 Temperature dependence of *P* and inverse of susceptibility (χ) for 1st and 2nd order transitions (Samara).[2]

1.3.3 Order parameter of a ferroelectric phase transition

According to Landau theory of phase transition the free energy of the system can be expressed in terms of a power series in order parameter *P* as,

$$A = \frac{1}{2}\gamma P^2 + \frac{1}{4}\lambda P^4 + \frac{1}{6}\xi P^6 + ...$$

where the coeficient γ, λ and ξ (especially γ) are functions of temperature. The nature of the transition and the behaviour of the ferroelectric properties in the immediate vicinity of T_C is determined by the signs and magnitudes of the coefficients γ, λ and ξ. In the paraelectric phase the coefficients γ and ξ are positive, whereas λ can be either positive or negative.[3, 4] In the ferroelectric phase γ becomes negative. Therefore, two cases can be discussed, i.e. case-1 λ (+)ve and case-2 λ (-)ve.

Case-1: Since all coefficients are (+)ve, the only stable state corresponds to $P = 0$, i.e a non-polar state. When γ becomes negative in ferroelectric phase, the free energy function will develop a maximum at $P = 0$ and a pair of minima at $\pm P_S \neq 0$. Thus the stable states of crystal corresponds to $P = 0$ for $\gamma > 0$ and to $P_S \neq 0$ for $\gamma < 0$. In this case the change in γ, and therefore in P_S with temperature is continuous, and the transition is of the second order.

Case-2: In this case, the free energy function have one minimum for $P = 0$ and two symmetric minima for $P \neq 0$ at the same *T*. At $T = T_C$, the three minima becomes equal, and the stable state of the crystal will jump discontinuously from one with $P = 0$ to one with $P = \pm P_S$. Therefore, P_S exhibits a discontinuity at T_C and the transition is of first order. The evolution of

free energy *vs*. order parameter with temperature is shown in Fig. 1.9 for first and second order transitions.

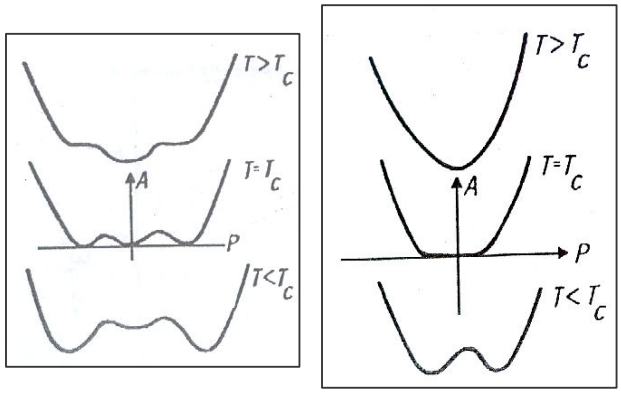

Figure 1.9 Evolution of free energy (A) versus *P* with temperature for 1st and 2nd order phase transition, respectively (Samara).[2]

1.3.4 Different types of ferroelectric transition

According to the phenomenological behaviour of the ferroelectric crystals, one can classify them into displacive type or order-disorder type. A detail discussion on classifying the ferroelectrics crystals has been given by Lines and Glass.[4] In this section characteristic features of the displacive and order-disorder ferroelectrics are discussed briefly.

(1) *Displacive type* – A displacive ferroelectric undergoes a phase transition accompanied by small and in principle continuous, spontaneous displacements of some of the ions within the unit cell from their equilibrium positions in the high-symmetry phase to yield the structure of the lower-symmetry phase. Few examples of Perovskite ferroelectric belong to this category are $BaTiO_3$, $PbTiO_3$, $LiNbO_3$, $BiFeO_3$ etc. The typical ferroelectric Perovskite $BaTiO_3$ happens to be the first known displacive type ferroelectric Perovskite.

(2) *Order-disorder type* – There is no sharp demarcation between the displacive and order-disorder phase transitions in terms of structural phase transitions. In case of order-disorder phase transition, there is a change in the crystal symmetry as a result of the redistribution of the ions over equiprobable positions at the transition temperature. In comparision with the displacive ones, the crystal structure of order-disorder ferroelectrics is more complex. The typical examples of order-disorder ferroelectrics are KH_2PO_4 (KDP), $NaNO_2$ etc.

1.3.5 Hysteresis in phase transitions

Hysteresis is a common feature of the first-order transition. The difference in the transition temperatures or pressures in the forward and reverse directions[73, 74] is called hysteresis of the transition. Observation of hysteresis suggests that the transformation does not occur at the point where the free energies are exactly equal. The possible causes for the hysteresis could be (i) formation of a hybrid single crystal,[72, 75] (ii) kinetics and (iii) existence of an activation barrier to transition.[76]. Factors such as particle size, rate of heating, and impurities appear to affect the magnitude of thermal hysteresis.[73, 77]

Several of the known transitions do not strictly belong to either type of transition i.e. neither strictly first order nor second order.[73] For example, the phase transition of well known compound $BaTiO_3$, which has second-order character, also shows a small first order effect (a small latent heat). In case of ferroelectric transition of KH_2PO_4, theoretically it should be of the first order, but it conforms closely to the second order. Therefore, it is possible that some transitions may be of mixed character.

1.4 Experimental techniques for studying ferroelectric phase transitions

Primary technique to study ferroelectricity in any system is dielectric spectroscopy and measurement of polarization (hysteresis loop). Often ferroelectric phase transitions are accompanied with structural changes. These can be probed using X-ray and neutron diffraction. The structural phase transitions always have change in local atomic arrangements and bond lengths etc. These changes influence the vibrational spectrum of the material, which can be probed using Raman, Brillouin, and infrared spectroscopy. The changes in the magnetic order can be probed using magnetization measurements. Depending on the order of the phase transition, there can be a latent heat associated with the structural transition. This aspect can be studied using differential scanning calorimetry or differential thermal analysis. Similarly, thermal properties such as specific heat, thermal conductivity and thermal expansion coefficient can also be investigated across phase transition.

1.5 Scope of present thesis

This thesis reports Raman and Brillouin spectroscopic investigations of phase transitions in one representative system of each type: (a) ferroelectric $NaNbO_3$, (b) relaxor-ferroelectric $Pb(Zn_{1/3}Nb_{2/3})_{0.85}Ti_{0.15}O_3$ (PZN-PT) and (c) multiferroic $(Bi_{1-x}La_x)_{0.5}Pb_{0.5}Fe_{0.5}Ti_{0.5}O_3$, $0 \leq x \leq 0.5$ (BLF-PT). Temperature is used as a primary thermodynamic parameter to take the system across phase transition(s). Where ever possible, both polycrystalline ceramic samples and single crystals are investigated. In the case of BLF-PT, tetragonal-cubic structural transition induced by La-composition as well as by temperature is studied using *in-situ* high temperature X-ray diffraction. Supporting dielectric and magnetic measurements are also carried out, where ever necessary and correlation of these properties to structural changes are discussed.

Chapter 1 gives a brief introduction to the fascinating world of ferroelectric materials and their unique properties and applications. The phenomenon of structural phase transitions is discussed in detail. The reasons / motivation for choosing the present systems are discussed in the respective chapters. C**hapter 2** contains the details of the synthesis procedures for polycrystalline ceramic samples and single-crystals, and the experimental techniques used for their investigations. The technique of Raman spectroscopy for probing the optical phonons and that of Brillouin spectroscopy for probing the acoustic phonons are described in detail. A brief discussion on the characterization tools, i.e. EDAX, X-ray diffraction, TEM, and SEM are also presented. **Chapter 3** presents results of low temperature Raman spectroscopic investigation on $NaNbO_3$. In this work, A detailed Raman spectroscopic studies of $NaNbO_3$ in the temperature range 10–300 K to study the antiferroelectric to ferroelectric transition both in cooling and heating cycles were carried out. The temperature dependence of integrated intensities of the modes has been examined in detail to obtain information about coexistence and hysteresis. In addition, an study on central peak in $NaNbO_3$ single crystal for antiferroelectric ($D_{2h}^{11}, Z = 8$) to antiferroelectric ($D_{2h}^{13}, Z = 24$) (P to R phase) phase transition

using Brillouin scattering at elevated temperature is presented. The spectra were recorded using a large free spectral range (FSR) of 3300 GHz from ambient to 773 K using a commercially available heating stage with a temperature stability of ± 0.1 K. The measurements were performed at successively higher temperature during a heating cycle. In **Chapter 4**, the Brillouin and polarized Raman spectroscopic studies on PZN-PT single crystal system are discussed in the context of tetragonal-cubic phase transition and the dynamics of polar nano regions in the relaxor-cubic phase. Brillouin measurements on $Pb(Zn_{1/3}Nb_{2/3})_{0.85}Ti_{0.15}O_3$ (PZN-PT) single crystal were carried out from ambient to 873 K to understand the dynamical behavior of PNRs in relaxor phase. Single crystals were synthesized by flux method and relaxor behavior was confirmed from dielectric spectroscopy. Polarized Raman spectra were measured upon heating from room temperature to 873 K in $X(YY)X'$ and $X(YZ)X'$ scattering geometries. The *T*-dependence of mode frequencies was examined for possible signatures of the phase transition. In **Chapter 5**, a composition-driven tetragonal-cubic transition in La-substituted system BLF-PT for $0.0 \leq x \leq 0.5$ is discussed on the basis of X-ray diffraction and Raman scattering results. The emphasis is to understand the nature of the phonons in this mixed-crystal system and to probe the crystallographic phase transition. The structural stability of these technologically important solid-solutions has not been investigated so far at elevated temperature. Therefore, the *x*-*T* phase diagram of $0.50(Bi_{1-x}La_xFeO_3)$-$0.50(PbTiO_3)$ solid-solution using *in-situ* X-ray diffraction at high temperature was established for the first time. Furthermore, phonons, magnetic and ferroelectric ordering in La-substituted $BLFPT_x$ are investigated for $x = 0.0$, 0.2, 0.3, 0.4 and 0.5 samples using Raman, magnetization and polarization measurements as a function of temperature. The Raman spectra are analyzed quantitatively to obtain mode frequencies, their line widths and intensities. Magnetization measurements are made from ambient down to 4 K in field-cooled and zero-field cooled conditions. The field dependence of magnetization is also studied to examine the possibility of a spin-glass like magnetic ordering. From the ferroelectric hysteresis loop, the composition

dependence of remnant polarization is also obtained. The observed results are discussed in the context of anisotropy and tetragonal-cubic structural transition. In C**hapter 6**, a summary of the results obtained, highlights of the inferences drawn and the conclusions arrived at are presented. Possible directions of future studies are also discussed in brief.

1.6 Summary

Ferroelectricity arises because of mismatch in positive and negative charge centers in the unit cell. The disordered distribution of different ions on the equivalent sites is the essential feature of a relaxor ferroelectric material. Multiferroic materials exhibit more than one ferroic order (ferroelectric + magnetic order). A stable phase has the lowest free energy. Phase transition from one structure to another take place under the influence of thermodynamic parameters such as temperature, pressure, external stimulus such as electric and magnetic field etc. Many properties such as phonon, dielectric, structural and magnetic exhibit changes across phase transitions. The phase transitions can be investigated using a variety of techniques such as Raman, Brillouin, dielectric and diffraction.

References

1. C. Kittel, *Introduction to Solid state Physics*, 7th ed. (Wiley, New York, 1976).
2. G. A. Samara, *Ferroelectricity Revisited, Solid State Physics*, Vol. **56**, 239.
3. E. Jona and G. Shirane, *Ferroelectric Crystals* (NY: The McMillan Company, 1962).
4. M. E. Lines and A. M. Glass, *Principles and Applications of Ferroelectrics and Related Materials* (Oxford: Clarendon Press, 1977).
5. W. Cochran, Phys. Rev. Lett. **3**, 412 (1959).
6. R. E. Cohen, J. Phys. Chem. Solids **61**, 139 (2000).
7. "Proceedings of the Second international Seminar on Relaxor Ferroelectrics," Ferroelectrics **235** (1999).
8. G. A. Smolenskii, V. A. Isupov, A. I. Agranovskaya and S. N. Popov, Sov. Phys. Solid State **2**, 2584 (1961).
9. F. Chu, N. Setter and A. K. Tagantsev, J. Appl. Phys.**74**, 5129 (1993).
10. Ph. Sciau, G. Calvarin and J. Ravez, Sol. Stat. Commun.**113,** 77 (2000).
11. A. Simon, J. Ravez and M. Maglione, J. Phys.: Condens. Matter **16**, 963 (2004).
12. N. Yasuda, H. Ohwa and S. Asano, Jpn. J. Appl. Phys. (Part 1) **35**, 5099 (1996).
13. A. A. Bokov and Z. -G. Ye, J. Material Sc. **41**, 31 (2006).
14. K. K. Mishra, V. Sivasubramanian, A.K. Arora and D. Pradhan, manuscript submitted.
15. Jae-Hyeon Ko, Do Han Kim, Seiji Kojima, Phys. Rev. B **77**, 104110 (2008).
16. V. Sivasubramanian, and S. Kojima, Phys. Rev. B **85**, 054104 (2012).
17. G. A. Smolenskii, J. Phys. Soc. Jpn. **28** (Supl.), 26 (1970).
18. M. D. Glinchuk and R. Farhi, J. Phys.: Condens. Matter **8**, 6985 (1996).
19. A. A. Bokov, JEPT **84**, 994 (1997).
20. P. N. Timonin, Ferroelectrics **199**, 69 (1997).
21. A. A. Bokov, Phys. Solid State **36**, 19, 1994; Ferroelectrics **190**, 197 (1997).
22. V. Westphal, W. Kleemann and M. D. Glinchuk, Phys. Rev. Lett. **68**, 847 (1992).

23. V. M. Ishchuk, Ferroelectrics **255**, 73 (2001).

24. W. Kleemann, Int. J. Mod. Phys. B **7**, 2469 (1993).

25. Y. Imry and S. -K. Ma, Phys. Rev. Lett. **35**, 1399 (1975).

26. N. De Mathan, E. Husson, G. Calvarin, J. R. Gavarri, A. W. Hewat and A. Morell, J. Phys. Condens.Matter **3**, 8159 (1991).

27. G. Burns and F. H. Dacol, Sol. Stat. Commun. **48**, 853 (1983).

28. S. B. Vakhrushev, B. E. Kvyatkovsky, A. A. Nabereznov, N. M. Okuneva and B. P. Toperverg, Ferroelectrics **90**, 173 (1989).

29. A. Nabereznov, S. Vakhrushev, B. Dorner, D. Strauch and H. Moudden, Eur. Phys. J. **11**, 13 (1999).

30. K. Hirota, Z. -G. Ye, S. Wakimoto, P. M. Gehring and G. Shirane, Phys. Rev. B **65**, 104105 (2002).

31. S. Vakhrushev, A. Nabereznov, S. K. Sinha, Y. P. Feng and T. Egami, J. Phys. Chem. Solids **57**, 1517 (1996).

32. M. Yoshida, S . Mori, N. Yamamoto, Y. Uesu and J . M. Kiat, Ferroelectrics **217**, 327 (1998).

33. H. Schmid, Ferroelectrics **162**, 317 (1994).

34. M. Fiebig, J. Phys. D **38**, R123 (2005).

35. M. Fiebig, T. Lottermoser, D. Frohlich, A. V. Goltsev, and R. V. Pisarev, Nature **419**, 818 (2002).

36. W. Eerenstein, N. D. Mathur, and J. F. Scott, Nature (London) **442**, 759 (2006).

37. Daniel Khomskii, Physics **2**, 20 (2009).

38. Magnetoelectric Interaction Phenomena in Crystals, Proceedings of the MEIPIC-2, edited by H. Schmid, Ascona, Switzerland, 13–18 September 1993, Ferroelectrics **161**–**162** (1994).

39. Magnetoelectric Interaction Phenomena in Crystals, Proceedings of the MEIPIC-3, edited by M. Bichurin, Novgorod, Russia, 16–20 September 1996 Ferroelectrics **204**, (1997).

40. *Magnetoelectric Interaction Phenomena in Crystals*, Proceedings of the MEIPIC-4, edited by M. Bichurin, Novgorod, Russia, 16–19 October 2001 Ferroelectrics **279**–**280**, (2002).

41. N. A. Hill, J. Phys. Chem. B **104**, 6694 (2000).

42. T. Kimura, T. Goto, H. Shintani, K. Ishizaka, T. Arima, and Y. Tokura, Nature (London) **426**, 55 (2003).

43. J. Wang, J. B. Neaton, H. Zheng, V. Nagarajan, S. B. Ogale, B. Liu, D. Viehland, V. Vaithyanathan, D. G. Schlom, U. V. Waghmare, N. A. Spaldin, K. M. Rabe, M. Wuttig, and R. Ramesh, Science **299**, 1719 (2003).

44. E. Ascher, H. Rieder, H. Schmid, and H. Stössel, J. Appl. Phys. **37**, 1404 (1966).

45. Ch. Binek and B. Doudin, J. Phys.:Condens. Matter **17**, L39 (2005).

46. H. Béa, M. Gajek, M. Bibes, and A. Barthélémy, J. Phys.: Condens. Matter **20**, 434221 (2008).

47. J. Wang, J. B. Neaton, H. Zheng, V. Nagarajan, S. B. Ogale, B. Liu, D. Viehland, V. Vaithyanathan, D. G. Schlom, U. V. Waghmare, N. A. Spaldin, K. M. Rabe, M. Wuttig, R. Ramesh, Science **299**, 1719 (2003).

48. Nicola A. Hill, J. Phys. Chem. B **104**, 6694 (2000).

49. Pio Baettig, Claude Ederer, and Nicola A. Spaldin, Phys. Rev. B **72**, 214105 (2005).

50. T. Atou, H. Chiba, K. Ohoyama, Y. Yamaguchi, and Y. Syono, J. Solid State Chem. **145**, 639 (1999).

51. Yu. N. Venevtsev, G. Zhdanov, and S. Solov'ev, Sov. Phys. Crystallogr. **4**, 538, (1960).

52. G. Smolenskii, V. Isupov, A. Agranovskaya, and N. Krainik, Sov. Phys. Solid State **2**, 2651 (1961).

53. F. Kubel and H. Schmid, Acta Crystallogr., Sect. B: Struct. Sci. **46**, 698 (1990).

54. M. M. Kumar, V. R. Palkar, K. Srinivas, and V. Suryanarayana, Appl. Phys. Lett. **76**, 2764 (2000).

55. S. T. Zhang, M. H. Lu, D. Wu, Y. F. Chen, and N. B. Ming, Appl. Phys. Lett. **87**, 262907 (2005).

56. X. Qi, J. Dho, R. Tomov, M. G. Blamire, and J. L. MacManus-Driscoll, Appl. Phys. Lett. **86**, 062903 (2005).

57. W. M. Zhu, Z.–G. Ye, Ceram. Int. **30**, 1435 (2004).

58. V. V. S. S. Sai Sunder, A. Halliyal, and A. M. Umarji, J. Mater. Res. **10**, 1301 (1995).

59. M. M. Kumar, A. Srinivas, S. V. Suryanarayana, and T. Bhimasankaram, Phys. Status Solidi A **165**, 317 (1998).

60. K. Balamurugan, N. H. Kumar, and P. N. Santhosh, J. Appl. Phys. **105**, 07D909 (2009).

61. W.-M. Zhu, H.-Y. Guo, and Z.-G. Ye, Phys. Rev. B **78**, 014401 (2008).

62. J. Cheng, S. Yu, J. Chen, and Z. Meng, Appl. Phys. Lett. **89**, 122911 (2006).

63. A. Singh, A. Gupta, and R. Chatterjee, Appl. Phys. Lett. **93**, 022902 (2008).

64. Vinod K. Wadhawan, *Introduction to Ferroic Materials*, (Gordon and Breach Science, 2000).

65. V. M. Goldschmidt, Geochemische Verteilungsgesetze der elements VII, VIII, 1927/28.

66. K. S. Knight, Solid State Ionics **74**, 109 (1994).

67. J. H. Yang, W. K. Choo, J. H. Lee, and C. H. Lee, Acta Cryst. B **55**, 348 (1999).

68. H. D. Megaw and C. N. W. Darlington, Acta Cryst. A **31**, 161 (1975).

69. A. M. Glazer, Acta Cryst. B **28**, 3384 (1972).

70. A. M. Glazer, Acta Cryst. A **31**, 756 (1975).

71. P. Ehrenfest, Proc. Amsterdam Acad. **36**, 153 (1933).

72. A. R. Ubbelohde, Quart. Rev. (London) **11**, 246 (1957).

73. K. J. Rao and C. N. R. Rao, J. Materials Sci. **1**, 238 (1966).

74. A. J. Dornell and W. A. McCollum, High Temp. Sci. **2**, 331 (1970).

75. A. R. Ubbelohde, Brit. J. Appl. Phys. **7**, 313 (1956).

76. D. G. Thomas, and L. A. K. Staveley, J. Chem. Soc. **1420**, 2572 (1951).

77. M. Natarajan, A. R. Das, and C. N. R. Rao, Trans. Faraday Soc. **65**, 3081 (1969).

Chapter 2

Experimental details

2.1 Synthesis

Ceramic materials are playing a major role in the material science because of their direct and indirect applications in day to day life. Therefore, the synthesis of ceramic powders as well as single crystals is of great importance in the progress of material science. There are several methods of powder sample synthesis; those are solid state reaction, chemical method which includes wet-dry, sol-gel and polymer-sol-gel etc. Each method has its own advantages and disadvantages in achieving a quality product with respect to purity, homogeneity and particle size etc. These are important from the point of view of performance, reliability, reproducibility and economy. The solid state reaction method is a simple, convenient and low cost technique. A discussion on powder sample synthesis is outline below. Growth of single crystal by flux method is discussed in the next section.

2.1.1 Solid state reaction

In the present work, raw chemicals with high purity were used for the sample synthesis. The various steps in solid-state reaction methods are shown as a flow chart in Fig. 2.1. The starting materials were weighed in stoichiometric proportion. First a dry mixing followed by wet mixing in ethanol was done. Agate motor and pestle was used for mixing. The amount of ethanol used was just enough to form slurry to prevent the selective sedimentation of the reagents. The mixed powders were then calcined at certain temperature depending upon the composition. After calcination, the powders were again ground and mixed thoroughly. The cylindrical pellets of dimension 10.5 mm diameter and 1.5 mm thickness were prepared using uniaxial isostatic cold press employing tungsten carbide die and plunger. In order to increase the density of the sample, the pellets were sintered. In sintering coordinated changes in all grains occur in a powder

compact to promote space filling, i.e. the grain centres move towards each other, thereby reducing the size of the compact and eliminating the pores. The reduction of surface and interface area is the driving force for the process. The sintering is influenced by the particle size, its distribution and agglomeration of the particles both before and after calcinations. Thus calcination essentially determines the quality of sintering. The calcination temperature and its duration should be chosen carefully to ensure that the reagents react well. At each stage of calcinations and final sintering, the phases were confirmed using X-ray diffraction.

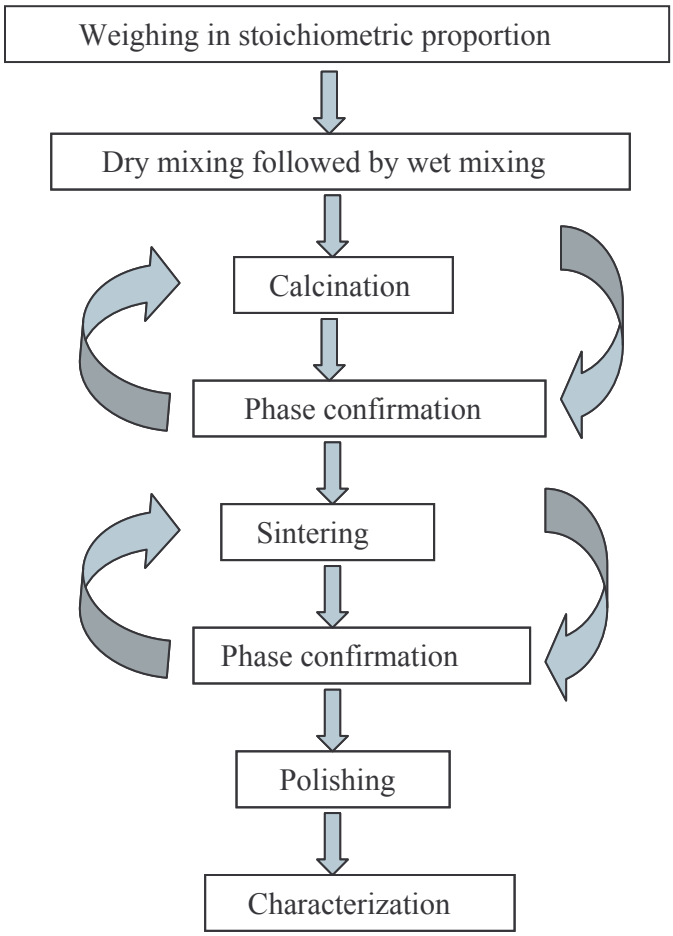

Figure 2.1 Various steps involved in solid state reaction.

2.1.2 Single crystal: Growth by flux method

Flux method is a common method for growth of single crystal because it is simple and less expensive than other techniques. A high temperature solvent is referred to as a flux because it

permits growth to proceed at temperatures well below the melting point of the solute phase. The essential requirements of a flux are that it should have a high solubility for the solute, without forming a stable compound. Good quality crystals can be grown by this method.

2.1.3 Synthesis parameters for samples synthesized for present studies

This thesis reports synthesis of both polycrystalline ceramics as well as single crystals of several ferroelectric system such as (a) ferroelectric $NaNbO_3$, (b) relaxor-ferroelectric $Pb(Zn_{1/3}Nb_{2/3})_{0.85}Ti_{0.15}O_3$ (PZN-PT) and (c) multiferroic $(Bi_{1-x}La_x)_{0.5}Pb_{0.5}Fe_{0.5}Ti_{0.5}O_3$, $0 \leq x \leq 0.5$ (BLF-PT) for investigation of their phase transitions. The procedures followed in synthesizing these ferroelectric systems have been discussed below.

(a) Synthesis of polycrystalline $NaNbO_3$

A single phase polycrystalline $NaNbO_3$ sample was prepared by solid state reaction method. A stoichiometric ratio of Na_2CO_3 and Nb_2O_5 were calcined at 1123 K for 3 hrs. The powder was pressed into pellet and sintered at 1373 K for 3 hrs.

(b) Synthesis of single crystal of $NaNbO_3$

Transparent and colourless single crystals of $NaNbO_3$ were grown by flux method with Na_2CO_3 and B_2O_3 as fluxes. The charge and fluxes were taken in the molar ratio 14.3 $NaNbO_3$: 40.5 Na_2CO_3 : 45.2 B_2O_3 mol%. The crystals were grown by cooling from 1448 to 1048 K at a rate of 1.5 K / h and then from 1048 K to ambient temperature at a rate of 100 K / h. The typical sample dimensions were 2 × 2 × 0.5 mm^3. The Perovskite phase was confirmed using powder X-ray diffraction analysis.

(c) Synthesis of single crystal of PZN-PT

Transparent and yellow coloured single crystals of $Pb(Zn_{1/3}Nb_{2/3})_{0.85}Ti_{0.15}O_3$ were grown by flux method with Pb_3O_4 as flux.[1] The charge and flux were taken in 40:60 ratio by weight. The crystals were grown by cooling from 1473 to 1203 K at a rate of 0.8 K / h and then from 1203 K

to room temperature at a rate of 300 K / h. The Perovskite phase was confirmed using X-ray diffraction analysis. The typical sample dimensions were 3 × 2 × 0.5 mm^3.

(d) Synthesis of polycrystalline BLF-PT

Polycrystalline $(Bi_{1-x}La_x)_{0.5}Pb_{0..5}Fe_{0.5}Ti_{0.5}O_3$ samples were synthesized for x = 0.0, 0.2, 0.3, 0.4 and 0.5 by the solid-state reaction technique. High purity starting materials (Bi_2O_3, La_2O_3, PbO, Fe_2O_3, and TiO_2) of 99.9% purity (Alfa Aesar) weighed in stoichiometric proportion were mixed and ground together. Powders were then calcined in a closed platinum crucible for 3 hours at 773 K in air, reground and calcined again for 4 hours at 1073 K. The calcined powders were pressed into pellets and sintered at 1373 K for 2 hours. Precaution was taken to avoid loss of PbO from the sample (Evaporation starts at 1023 K), which creates vacancies at Pb and O sites.[2, 3] This considerably affects the physical properties of the system. This was done by placing $PbZrO_3$ powder around the pellet which maintains a high partial pressure over the sample.[4] The sintering were carried out within a special arrangement as shown in Fig. 2.2. The pellet was about 10.5 mm in diameter and 1.5 mm thick. X-ray powder diffraction patterns of the sintered samples were measured to determine the structure and confirm the phase purity.

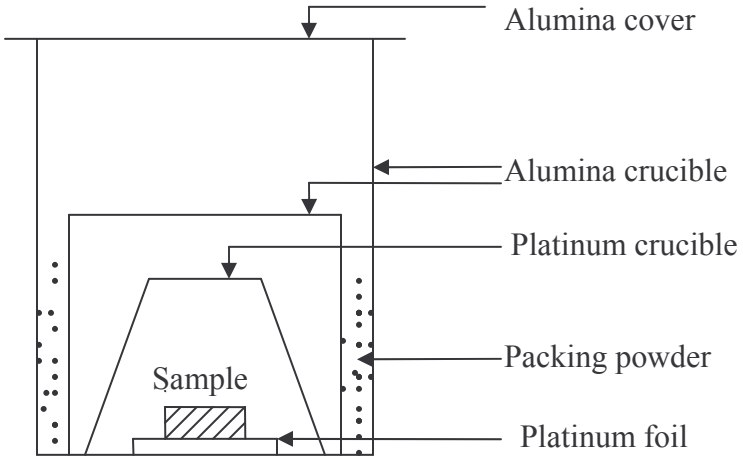

Figure 2.2 Schematic configuration used for sintering of samples.

2.2 Experimental techniques

Various experimental techniques have been employed for characterization and investigations of the phase transitions in these systems. The characterization techniques include X-ray diffraction, Transmission electron microscopy, Scanning electron microscopy, and Energy dispersive X-ray analysis. The investigations of vibrational, structural, dielectric and magnetic properties are carried out using Raman and Brillouin spectroscopy, X-ray diffraction, dielectric, and magnetization measurement.

2.2.1 Raman scattering

Inelastic scattering of light by atomic vibrations in molecules, liquids and solids, discovered by C. V. Raman in 1928, is known as Raman scattering. In Raman spectroscopy, the sample is irradiated by intense laser beam of frequency ω_o in the UV-Visible region, and the scattered light is collected and analysed. The scattered light consists of two parts: one is the Rayleigh scattering part which is intense and has the same frequency as the incident beam ω_o. On the other hand, the second part is called Raman scattering which is very weak (10^{-10} of the incident beam) and has frequencies $\omega_O \pm \omega_P$, where ω_p is characteristic vibrational frequency of system. The $\omega_O - \omega_P$ is called the Stokes line whereas the $\omega_O + \omega_P$ is the anti-Stokes lines. Hence, in Raman spectroscopy, the vibrational frequency ω_P is measured as a shift from the incident photon frequency ω_O. At normal condition, the population of phonons in a solid at ground state is much larger than that at first excited state which is governed by Maxwell-Boltzmann distribution law. Therefore, the Stokes lines are stronger than anti-Stokes lines. Since both the lines give the same information, it is practice to measure only the Stokes side of the Raman spectrum.

2.2.2 Quantum theory of Raman scattering

The lattice vibrations are quantized and are called phonons. There exist several discrete excited states above the ground state of a vibrational energy level. When a photon of incident energy

$\hbar\omega_0$ and momentum $\hbar k_0$ undergoes inelastic scattering, a phonon of energy $\hbar\omega_P$ and momentum $\hbar q$ is either created or annihilated. However, the total energy and momentum before and after the scattering is conserved. During the creation of a phonon the system goes to a higher excited vibrational state from the ground state by absorbing energy from the incident photon. On the other hand, in phonon annihilation process, the system returns to ground state from excited vibrational state by releasing energy. The energy and momentum conservation process can be written as follow,[5]

$$\hbar\omega_S = \hbar\omega_0 \mp \hbar\omega_P \qquad (2.1)$$

$$\hbar\vec{k}_S = \hbar\vec{k}_0 - \hbar\vec{q} \qquad (2.2)$$

where + sign indicates, phonon is annihilated (anti-Stokes), and – sign indicates, phonon is created (Stokes). $\hbar\omega_S$ and $\hbar k_S$ are scattered photon energy and momentum, respectively. Here the energy and momentum equations are scalar and vector equations, respectively. Both creation and annihilation of phonon is schematically shown in Fig. 2.3. Anti-Stokes scattering depends on the phonon population in the excited state of the material before the light is incident. The

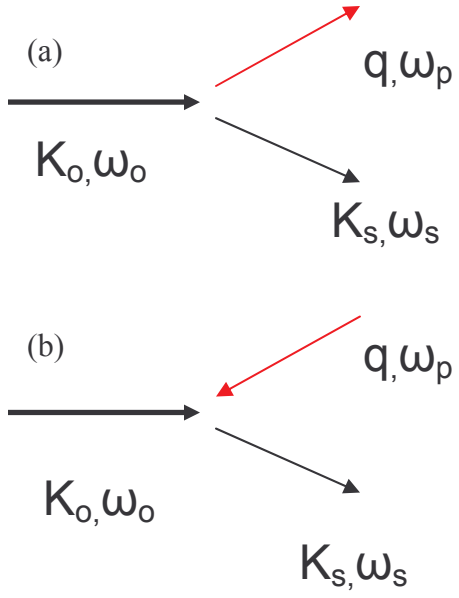

Figure 2.3 Schematic presentation of (a) creation (Stokes) and (b) annihilation (anti-Stoke) of phonon(q, ω_p).

probability for anti-Stokes scattering therefore decreases on lowering the temperature, because of a decrease in the phonon population. On the other hand, Stokes scattering does not require a phonon to be present and can, therefore, occur at any temperature. From the quantum mechanical theory the ratio of Stokes to anti-Stokes scattering events is given by: [5]

$$\frac{I_s}{I_{as}} = \exp\left(\frac{\hbar\omega_P}{k_B T}\right). \tag{2.3}$$

As mentioned earlier, the magnitude of scattering vector q depends on the scattering angle.[5]

$$\left|\vec{q}\right| = \left|\vec{k}_0 - \vec{k}_S\right| \tag{2.4}$$

The wavevector of the photon is directly proportional to its frequency $q = \omega/c$. Since the maximum phonon energy is less than ~5% of the visible photon energy, the scattered photon energy and hence its wavevector is nearly same as that of incident photon. One can therefore make the approximation $\left|\vec{k}_0\right| \approx \left|\vec{k}_S\right|$. From the vector diagram, the expression for the phonon momentum can be given by,[5, 6]

$$\left|\vec{q}\right| = 2\left|\vec{k}_0\right| Sin\frac{\theta}{2} \tag{2.5}$$

where θ is the scattering angle. In a back scattering geometry, $\left|\vec{q}\right| = 2\left|\vec{k}_0\right|$. Hence, the maximum value of q that can be accessed in an inelastic light scattering experiment or Raman scattering is of order 10^5 cm^{-1}. This is very small compared to the Brillouin zone boundary in a typical crystal (~ 10^8 cm^{-1}). Inelastic light scattering is thus able to probe phonons only near the centre of the Brillouin zone as shown in Fig. 2.4. However, the conservation of wave vector (Eq. 2.2) is violated in case of imperfect crystals such as solid solutions and amorphous solids because of

lack of translational symmetry. Therefore phonons other than zone center also take part in Raman scattering process.[7, 8] The experimental details of Raman spectrometer will be discussed in later part of this chapter.

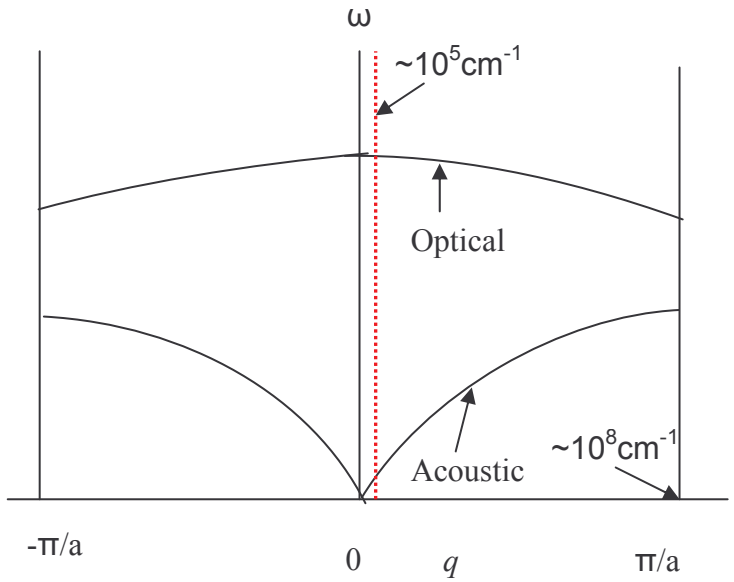

Figure 2.4 Schematic representation of two dispersion branches.

2.2.3 Brillouin scattering

Brillouin scattering is the inelastic scattering of light from acoustic phonons. The energy and momentum conservation equations (Eqs. 2.1 and 2.2) are valid here also and can be rewritten as

$$\hbar\omega_S = \hbar\omega_0 \mp \hbar\omega_B \qquad (2.6)$$

$$\hbar\vec{k}_S = \hbar\vec{k}_0 - \hbar\vec{q} \qquad (2.7)$$

where + sign indicates, phonon is annihilated (anti-Stokes shift), and – sign indicates, phonon is created (Stokes shift). ω_B is the Brillouin shift representing the acoustic phonon frequency. For $q \sim 10^5$, the acoustic phonon frequency is very small (1-2 cm^{-1}). In this limiting value of q, the lattice behaves as an elastic continuum and the acoustic phonon frequency depends linearly on q, i.e, $\omega_B(q) = v_S q$, where v_S is the sound velocity in lattice. From Eq. (2.5) one gets

$$\omega_B(q) = 2v_S k_0 \mathrm{Sin}\theta/2 \qquad (2.8)$$

where $k_0 = \eta\omega_0/c$, where η is the refractive index and c is the velocity of light. Hence the Brillouin shift depends on θ. In backscattering geometry, $\omega_B = 2v_S k_0 \sim 1\text{-}2\ \mathrm{cm}^{-1}$. Therefore the relative shift ω_B/ω_0 is very small and the resolving power of the spectrometer to obtain an accurate measurement of acoustic phonon should be $\sim 10^7$. This can not be achieved in a dispersive monochromator. Hence a Fabry-Perot interferometer is used. This technique is discussed in later part of this chapter.

Brillouin scattering can also be used for studying quasi-elastic light scattering arising from relaxation processes in solids.[9-11] In particular, in case of relaxor, a central peak in the Brillouin spectrum is found due to relaxation dynamics of polar nano regions (PNRs).[12-14] The anomalous behaviour of acoustic phonon and central peak across the phase transitions in ferroelectric materials have been studied using the Brillouin scattering technique.[12-14] The spectra shape of the Brillouin scattered light contains contributions from the instrumental resolution function and the phonon life-time. The normalized spectral line shape contributed by the phonon lifetime τ_q is a Lorenzian function whereas for instrumental broadening a Gaussian function is used.[7] Hence it is possible to study various damping mechanisms by measuring the natural line-width using this technique.

2.3 Raman scattering set ups

In the present study, SPEX double monochromator-based Raman spectrometer and Renishaw *micro*-Raman spectrometer were used.

2.3.1 SPEX Raman spectrometer

Figure 2.5 shows the schematic diagram of the SPEX Raman spectrometer used for measurements. It consists of a laser excitation source, focusing lens, sample holder, collection optics, dispersing monochromator and a detector.

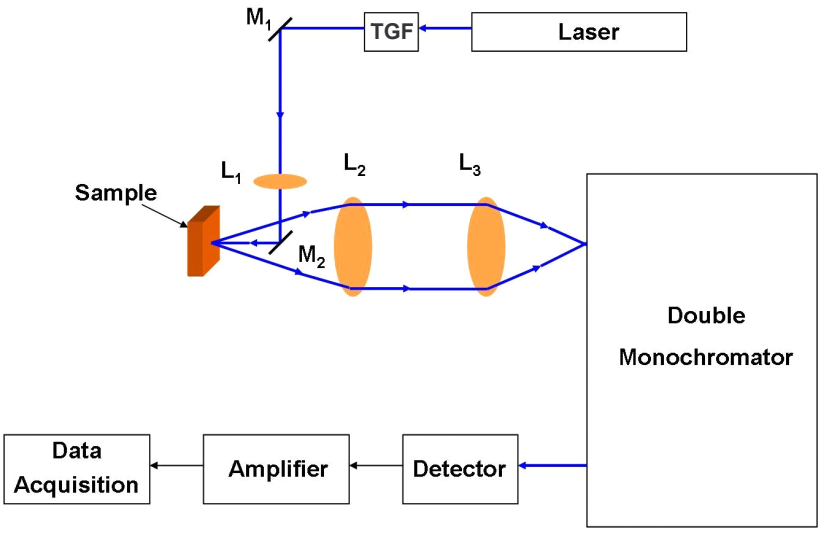

Figure 2.5 Block diagram of SPEX Raman spectrometer.

(a) Light source and sample illumination system: The light source was a 5 W Ar^+ laser (model I-90 Coherent). 488 nm wavelength was used. The laser beam is filtered to eliminate other spontaneous emissions lines using a tunable grating filter (TGF). Mirror M1 is at 45° angle to the incident laser beam and directs it to fall on the focusing lens L1 of focal length 70 mm. Another small mirror M2 is mounted at 45° to the incident laser beam so that the beam can be made to illuminate the sample. Mirror M2 also blocked the reflected spot from the sample and prevented it from going towards monochromator. The scattered light was collected by the camera lens L2 of focal length 50 mm and made into a parallel beam, which was focused in to the entrance slit of the double monochromator using a third lens L3 of focal length 400 mm.

(b) Monochromator: Monochromator is used for analyzing the scattered light. Scattered light from the sample was dispersed using 0.85 m focal length double monochromator (model 14018 SPEX). Two holographic grating with 1800 grooves/mm are used for dispersion. After the first stage of dispersion, the beam is focused and passed through an intermediate slit. Opening of the this intermediate slit is optimized so as to permit the selected wavelength as well as to perform a good rejection of Rayleigh light. The gratings are rotated by stepper motor controlled cosecant

drive which ensures that the rotation of the lead-screw is linear in wavenumber. Furthermore, the dispersion of the two gratings is in additive mode. Therefore, it offers high resolution and also high Rayleigh rejection. The Raman spectra down to 10 cm^{-1} could be recorded with this spectrometer. Although the spectrometer resolution at minimum slits was 0.15 cm^{-1}, much larger slits were used to allow sufficient light intensity for obtaining the spectra with reasonable signal to noise ratio.

(c) Detector: The scattered light coming out from the exit slit was focused on Photomultiplier tube (Hamamatsu R943-02) using a lens. PMT converts photons into sharp voltage pulses. Output pulses from the PMT are processed by a pre-amplifier, amplifier and discriminator stage in order to reject the noise from dynode chain emission.

2.3.2 Renishaw *micro*-Raman spectrometer

Figure 2.6 shows the schematic block diagram of the Renishaw *micro*-Raman spectrometer. It consists of a laser, a system unit, a microscope unit, monochromator and a CCD (charged coupled device) cemera detector. The working of this spectrometer is briefly described below.

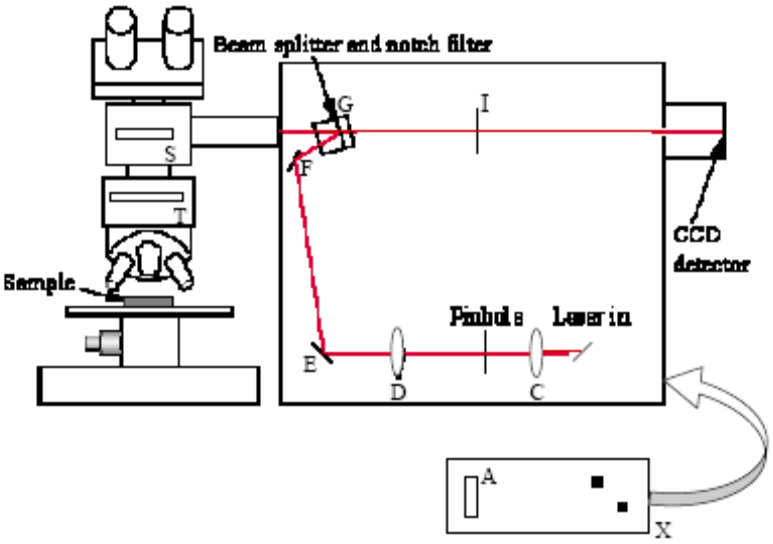

Figure 2.6 Schematic diagram of Renishaw *micro*-Raman spectrometer.

(a) Light source: An Ar^+ laser light of wavelength 514.5 nm has been used as a source. The laser unit is mounted behind the system unit. It contains a delivery optics tube consisting of alignment

mirror X and a laser attenuation filter wheel A. The filter wheel contained several neutral density filters, which are used to attenuate the power of the laser beam. The alignment mirror is to align and send the laser beam into the system unit through delivery optics tube.

(b) System unit: As shown in Fig. 2.6, the laser light entering the system unit is aligned by a mirror B and then followed by fixed objective lens C which converge the light beam to a ~10 μm pinhole. A second movable objective lens D, is used to make a well collimated parallel beam. Two mirrors E and F are used to reflect the light onto the holographic filter. The angle of holographic filter is adjusted in such a way that the laser beam can pass the microscope, and into the optical path of the microscope, located out of the spectrometer.

(c) Microscope unit: In this unit, a mirror is used to reflect the laser light and make it pass through the microscope objective lens to illuminate the sample placed on a mechanical stage. The sample is observed through the microscope eyepieces by moving the mirror out of the beam using the control S. A beam splitter is located below the mirror, which can be moved in and out of the path by control T. It allows the sample to be illuminated with light and can be viewed through the eyepieces and hence it helps in positioning and focusing of the sample. The scattered light from the sample also contains Rayleigh line. The scattered light passes through the set of holographic filters G located in system unit to remove the Rayleigh line.

(d) Monochromator: The scattered light is passed through the slit I to enter the single monochromator using 1800 grooves/mm. The light gets dispersed here.

(e) Charged couple device (CCD) camera: The CCD camera has a two dimensional arrays of pixels. Finally, the dispersed light is focused on the CCD where it converts the light into charges. The charge is proportional to the integrated intensity and it is read by a readout electronics. Data acquisition was carried out by computer using the WIRE 3.2 software. This software allows the user to set the spectral range, accumulation time and laser power. A rapid recording of spectrum

is facilated with its help. The spectra up to 30 cm^{-1} could be measured without loosing the signal. The spectrometer resolution for 1800 grooves/mm grating was ~1.5 cm^{-1}. The Raman shift in wavenumbers was calibrated using the 520.5 cm^{-1} Raman line from Si- single crystal.[15]

2.4 Brillouin scattering set up

Brillouin scattering measurements were performed using a high contrast 3+3-pass tandem Fabry-Perot interferometer (JRS Scientific Instruments).

2.4.1 Fabry-Perot Interferometer

A Fabry-Perot interferometer (FP) is used in spectroscopy to obtain a resolution from MHz to GHz. It consists of two plane mirrors mounted parallel to one another. For a particular spacing L_1, the interferometer can transmit only certain wavelength λ as written as, $L_1 = n\lambda/2$, where n is integer and λ is the wavelength of transmitted light. The spacing between successive transmitted wavelengths is called as free spectral range (FSR = $c/2L_1$, where c is velocity of light). The quality factor also known as finesse $F = 4R/(1-R)^2$, which depends primarily on the mirror reflectivity (R) and flatness, determines the width δλ (resolution) of a given transmission peak as

$$\delta\lambda = \mathrm{FSR}/F \qquad (2.9)$$

The FSR of the interferometer can be made large by decreasing L_1, but with increase in FSR, δλ also increases and hence the resolution decreases. In order to have a large FSR without affecting its resolution, a tandem interferometer is used.

2.4.2 Tandem Interferometer

In tandem interferometer, the FSR can be increased at a fixed resolution by the use of two FPs in series. To use the tandem interferometer as a spectrometer, it is necessary to obtain a synchronous operation of two interferometer and both interferometer must satisfy

$$\delta L_1/\delta L_2 = L_1/L_2, \qquad (2.10)$$

where δL_1 and δL_2 are the changes in mirror spacing in FP1 and FP2 simultaneously and L_1 and L_2 are the respective spacing of FP1 and FP2. Further the typical spacing L_1 and L_2 are related[16] by $L_2 \sim 0.95L_1$.

The principle of the tandem scan is shown schematically in Fig. 2.7. The first interferometer FP1 is located in the direction of the translation stage movement. However, the second interferometer FP2 is located with its axis at an angle θ to the scan direction. When the translational stage moves to the right, it sets both the spacing of FP1 and FP2 as L_1 and $L_1\text{Cos}\theta$ respectively.

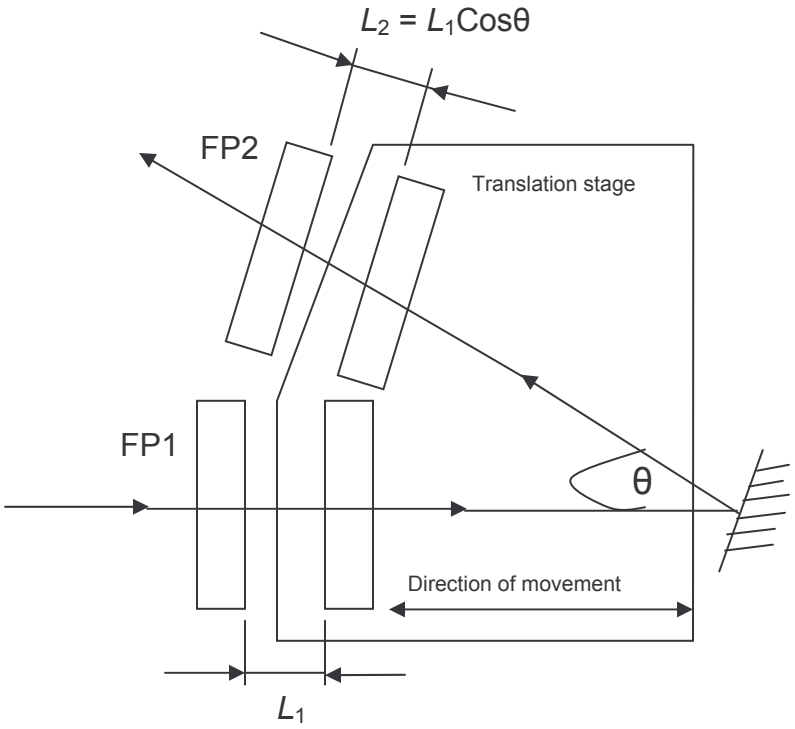

Figure 2.7 Principle of the tandem scan.

A scan δL_1 of the translational stage produces a change of spacing δL_1 in FP1 and $\delta L_1\text{Cos}\theta$ in FP2 and it gives $\delta L_1/\delta L_1\text{Cos}\theta = L_1/L_1\text{Cos}\theta$ as in Eq.(2.10). Therefore both the FP Interferometers scan synchronously. The main features of this system can be summarizes as (a) Complete dynamic synchronization over a large scanning range and (b) Good static synchronization due to the compact design which provides both FP interferometers to share the same environment.

Furthermore, in order to achieve a large FSR, and high contrast without affecting the resolution, 3+3-pass tandem Fabry-Perot Interferometer is used.

2.4.3 3+3-pass tandem Fabry-Perot Interferometer

The high contrast is achieved by multiple passing of transmitted light through FP1 and FP2 (3+3-pass). In designing a multi-pass system and selecting the most suitable plate reflectivity, the prime parameter is the required contrast. It depends on the nature of the sample and the likely strength of elastic scattering. For transparent and strongly scattering sample, a contrast of ~10^7-10^9 is required, whereas for opaque and strong surface scattering samples a value of 10^{10} - 10^{12} is needed. For single pass of transmitted light through the FP, the contrast[17] C_1 is ~ 10^3. For n-passes, the net contrast becomes $C_n \sim (C_1)^n$. Thus for 6-passes the contrast $C_6 \sim (C_1)^6 \sim 10^{18}$, but practically a contrast ~10^{14} is achieved in this instrument.

2.4.4 Brillouin spectrometer

It consists of a laser source, the 3+3–pass tandem Fabry-Perot interferometer, PMT detector and control electronics.

(a) Laser source: A 532 nm single-mode diode-pumped solid state laser (Innolight Diabolo 500) has been used to obtain a monochromatic and well collimated beam.

(b) 3+3-pass tandem Fabry-Perot Interferometer: The spectrometer consists of two sets of optical systems, i.e. (a) alignment optics and (b) tandem optics. The optical system is such that it allows the interferometer to be used both in the alignment and tandem modes as shown schematically in Figs. 2.8 and 2.9.

Alignment mode: The system is normally used in a multipass tandem mode. Prior to operation in this mode, one should ensure that both FP1 and FP2 have been pre-alligned parallel and with the correct relative spacing. This mode is based on the fact that when a FP is transmitting, the reflected intensity tends to zero. Hence a minimum value of reflected intensity is obtained when

the interferometer is optimally aligned. Therefore, on scanning the interferometer the photomultiplier signal show a background intensity punctuated by minima whenever either FP1 or FP2 transmits. The basic optical system used for alignment and the measured reflected intensity are shown in Fig. 2.10.

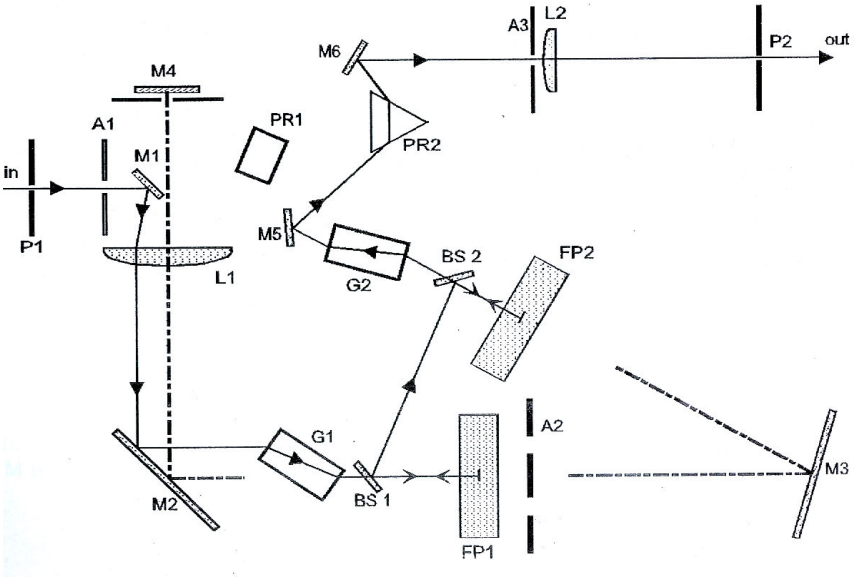

Figure 2.8 Alignment optics.

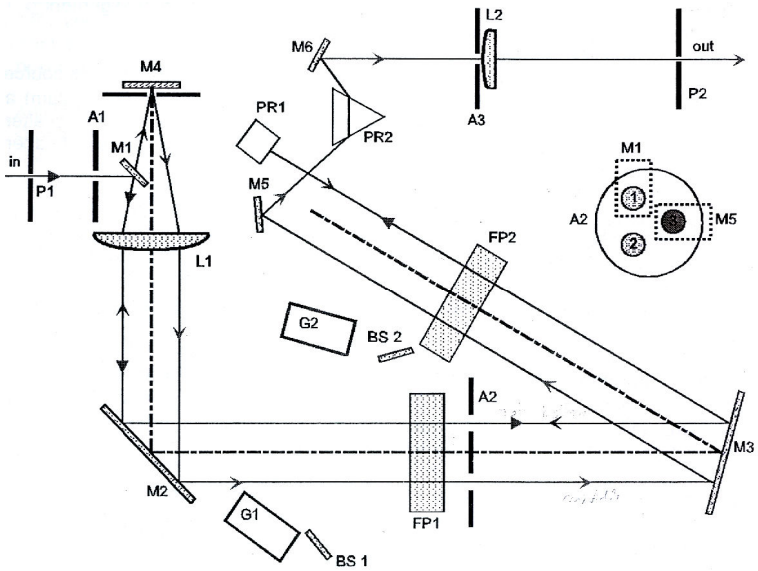

Figure 2.9 Tandem optics.

Tandem mode: After aligning the interferometer using the optical configuration as shown in Fig. 2.8, the spectrometer is set in the tandem mode. In this mode, the optical arrangements have been shown in Fig. 2.9 to facilitate the 3+3-pass transmitted light. The scattered light from the

sample obtained in a backscattering experiment is focused on the input pinhole and is allowed to pass through the spectrometer. The external optical arrangement using mirrors and lens are used to direct the scattered light inside the spectrometer through the entrance aperature. The spectrometer is scanned and the transmitted signal is measured as a function of L_1 using the photon detector, to cover the FSR in 1024 channels. Scanning of L_1 is done piezoelectrically. Data is accumulated synchronously over 1000 or more scans depending on the signal to noise ratio.

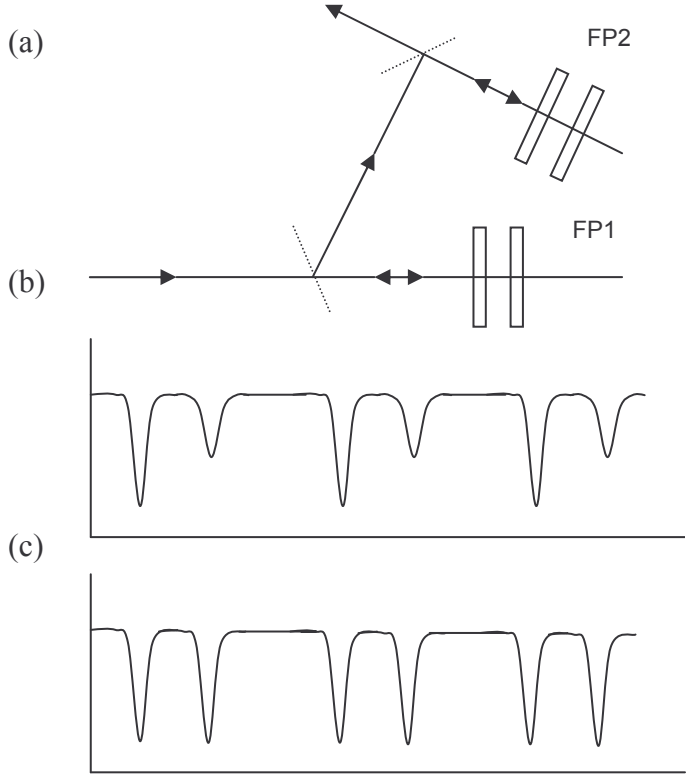

Figure 2.10 (a) Basic optical system used for obtaining alignment in the reflection mode, (b) Measured reflected intensity for imperfectly aligned FP1 and FP2, and (c) Measured reflected intensity after correct alignment of both FP1 and FP2.

2.5 X-ray diffraction technique

Room temperature powder XRD patterns of samples were recorded using a computer controlled X-ray diffractometer (STOE, Germany). *in-situ* high temperature X-ray diffraction patterns were recorded using computer controlled X-ray diffractometer (Siemens D500). A Cu target was used for X-ray generation. The diffractometer consists of flat pyrolitic graphite secondary

monochromator that selects the Cu K_α (λ=1.5418 Å) radiation and the detector was NaI:Tl scintillation counter. Si (911) single crystal was used as sample holder. The diffraction pattern was recorded in a θ-2θ Bragg-Brentano geometry. X-ray diffraction patterns as a function of temperature were obtained using an Edmund Buhler high temperature attachment. A tantalum strip with a radiation shield was used as sample holder and temperature was controlled within ± 0.1 ^oC. Laue pattern was obtained using Phillips X-ray generator with white spectrum from Tungsten target. The pattern was recorded using an imaging plate and scanned in a home-built scanner to obtain a digital image.

2.6 Transmission electron microscopy

Selected Area Electron Diffraction (SAED) studies were carried out using a JEOL - 2000 EX II transmission electron microscope (TEM) operated at 200 kV to analyze the phase and crystalline nature of the samples. A stream of electrons is obtained from an electron source and made to accelerate (100-300 kV) towards the sample in vaccum. The electron beam is confined and focused by using apertures and magnetic lenses. The interaction between electron beam and specimen generates elastic and inelastic scattering. The objective lens forms a diffraction patterns in the back focal plane. The diffraction technique is used to measure the spacing of the atomic crystalline lattice and determine the crystal structure. The diffraction phenomenon is based on the diffraction of the electron beam by a crystalline lattice. The crystalline lattice diffracts electrons to form bright spots on the viewing screen and the image will consists of central bright spot surrounded by a series of spots, which are reflections. The central bright spot represent undiffracted rays while the peripheral spots represents rays diffracted at various angles. The distance of the spots from the bright central spot is inversely proportional to the *d*-spacing of the crystalline lattice. For preparing TEM samples, the sintered samples were powdered. A small quantity of the powder was ultrasonicated in methanol and allowed to stand for ~ 10 minutes. A

single drop from the top of the suspension was then deposited on a carbon coated grid using a syringe and dried under infrared lamp to carry out the SAED studies.

2.7 Scanning electron microscopy

The scanning electron microscopy was used to study the microstructure (i.e., grain size, grain distribution, voids etc.) with high resolution and for obtaining the compositions of the sample. In this technique, a beam of energetic electrons bombard the sample leading to emission of X-rays, secondary, and back-scattered electrons from the sample. These electrons are collected by the detector and convert into signal. SEM micrographs were obtained from the gold coated fractured surface of the sintered sample. The chemical compositions of the sample were determined using energy dispersive X-ray spectrometer attached to SEM. In the present investigations, Energy dispersive X-ray analysis and microstructural analysis of the samples were carried out using a Cam Scan (CS 3200) scanning electron microscope.

2.8 Dielectric spectroscopy

The macroscopic behaviour of a dielectric can be studied by making it as a parallel plate capacitor. The capacitance (C) of such a capacitor is written as $C = \varepsilon_o\varepsilon_r A/d$, where ε_o is the dielectric permittivity of free space, ε_r is the real part of relative permittivity of the dielectric, A and d are the area and thickness of the sample respectively. Further, the dielectric loss or dissipation factor of the dielectric is written as $\tan\delta = \varepsilon_r'/\varepsilon_r$, where ε_r' is the imaginary part of the relative dielectric constant. In the present work, the samples were electroded with silver paint by firing at 400 ^oC for 1 hr. The dielectric parameters (capacitance and dissipation factor) were measured in a wide range of frequency (100 Hz to 1 MHz) using a computer–controlled LCR meter/ impedance analyzer (PSM: N4L (Model: 1735, UK)) as a function of temperature. The temperature was measured by a thermocouple placed near the sample. The hysteresis loop (P~E

loop) measurements were carried out by using an automatic *P~E* loop tracer. The measurements were carried out at ambient under the applied AC field with amplitude 5 kV/cm at 50 Hz.

2.9 Vibrating Sample Magnetometer (VSM)

The VSM works under the principle of Faraday's law of electromagnetic induction. The sample is magnetized by a homogeneous applied magnetic field and is vibrated with respect to a stationary pick-up coil. The change in magnetic flux because of vibration of magnetized sample induces an emf in the pick-up coil. The induce emf *V* is proportional to the magnetic moment of the sample. In this work, the magnetization (*M~H* loop) measurements were done using a VSM (Cryogenics) up to a maximum field of ± 50 kOe at ambient and down to 4 K. The zero-field cooled (ZFC) and field-cooled (FC) magnetization were measured as a function of *T* in the 4-300 K range with different applied magnetic fields.

References

1. S. Gentil, G. Robert, N. Setter, P. Tissot, and J-P Rivera, Jap. J. Appl. Phys., **39**, 2732 (2000).
2. D. M. Smyth, M. P. Harmer, and P. Peng, J. Am. Ceram. Soc., **72**, 2276 (1989).
3. E. S. Cho, J. Kim, S. L. Kang, Jap. J. Appl. Phys., **36**, 5562 (1997).
4. V. Sivasubramanian, V. R. K. Murty, B. Viswanathan, and M. Sieskind, J. Phys.: Condens. Matter **8**, 2447 (1996).
5. M. Fox, *Optical Properties of Solids*, (Oxford University Press, New York, 2001).
6. N. W. Aschroft and N. D. Mermin, *Solid State Physics*. (Holt, Rhinehart and Winston, New York, 1976).
7. M. Cardona, *Light Scattering in Solids* (Sringer-Verlag, Berlin, 1975).
8. K. K. Mishra, V.Sivasubramanian, R. M. Sarguna, T. R. Ravindran, and A.K. Arora, J. Solid State Chem. **184**, 2381 (2011).
9. A. Hushur, S. Gvasaliya, B. Roessli, S. Lushnikov, and S. Kojima, Phys. Rev. B **76**, 064104 (2007).
10. R. Ohta, J. Zushi, T. Ariizumi, and S. Kojima, Appl. Phys. Lett. **98**, 092909 (2011).
11. A. Hushur, H. Shigematsu, and Y. Akishige, Appl. Phys. Lett. **86**, 112903 (2005).
12. V. Sivasubramanian, and S. Kojima, Phys. Rev. B **85**, 054104 (2012).
13. S. Tsukada and S. Kojima, Phys. Rev. B **78**, 144106 (2008).
14. Shabbir and S. Kojima, Appl. Phys. Lett. **91**, 062911 (2007).
15. D. A. Long, *Raman Spectroscopy* (Mcgraw Hill NewYork, 1977).
16. J. R. Sandercock, *Tandem Fabry-Perot Interferometer TFP-1* (Operator manual, CH-8909).
17. J. M. Vaughan, *The Fabry-Perot Interferometer* (Adam Hilger UK, 1988).

Chapter 3

Raman and Brillouin spectroscopic studies on phase transition in Ferroelectric $NaNbO_3$

3.1 Introduction

Lead zirconate titanate is most widely employed in many electromechanical components such as actuators, ultrasonic transducers and sensors because of its strong piezoelectric response. However, in view of the toxicity and environmental impact[1] of this material due to high lead content, researchers have been trying to develop alternative lead-free materials. Among these, $NaNbO_3$ and its solid-solutions with Li and K exhibit unique electrical and mechanical properties, which are of interest for practical applications.[2-4] $NaNbO_3$-based solid solutions such as (K-Na)NbO_3, (Li-Na)NbO_3 are promising for practical applications due to their high piezoelectric coefficients. $NaNbO_3$ exhibits a complex sequence of structural phase transition as a function of temperature.[5-16] It exhibits a transition from paraelectric to antiferroelectric and then to ferroelectric phase and therefore is of particular interest from the point of view of sequence of phase transitions. At room temperature, $NaNbO_3$ makes transition to the ferroelectric phase under modest electric field. This property makes it important for various applications including high-density optical data storage.[2, 17] $NaNbO_3$ has excellent nonlinear optical properties and finds significant applications in hologram recording materials.[5-6]

Extensive studies on the various aspects of phase transitions in $NaNbO_3$ have been reported using a variety of experimental techniques including X-ray absorption fine structure,[7] transmission electron spectroscopy,[8] electron paramagnetic resonance,[9] nuclear magnetic resonance,[10] etc. An extensive Raman study combined with X-ray diffraction and dielectric measurements confirmed the presence of an incommensurate phase in $NaNbO_3$ in the temperature interval 410-460 K.[6] Low frequency Raman studies on $NaNbO_3$ single crystal revealed the occurrence of a quasi-elastic peak and the phase transition was attributed to the

order-disorder process due to the relaxation response of Nb ion in the temperature interval 513-713 K.[11] Shen *et al.* based on the temperature variation of phonon modes during cooling and heating cycles of measurement suggested that both ferroelectric and antiferroelectric phases coexist in the temperature range 40-180 K[12] during cooling cycle. However it is not clear from these studies[6, 12] how the temperature range of coexistence was obtained as no detailed intensity analysis had been done. Temperature dependent Raman scattering studies in $NaNbO_3$ by Lima *et al*. suggested that the orientation of NbO_6 group plays important role in stabilizing the low temperature ferroelectric phase.[14] Using Raman scattering Lin *et al*. found that the antiferroelectric-ferroelectric phase transition occurs at about 160 K during cooling while the reverse transition near 260 K on heating.[15] Recent neutron diffraction studies revealed the coexistence of both anti-ferroelectric (AFE) and ferrolelectric (FE) phases over wide range of temperature from 12 to 280 K with hysteresis of ~170 K between cooling and heating cycles.[13] X-ray diffraction (XRD) analysis reveals that the structure is rhombohedral below 173 K.[18] In spite of the extensive studies on the phase transitions in $NaNbO_3$ as discussed above, evolution of antiferroelectric-ferroelectric phase transition is not clearly understood. The temperature evolution of intensities of Raman modes have been employed to study the structure and phase transition behaviour of amorphous and crystalline materials.[19, 20, 21] In order to obtain a better understanding of the coexistence of phases, a detailed study of the temperature dependence of various modes can be helpful.

Understanding the nature and the dynamics of structural transitions in ferroelectric materials has been the aim of several studies.[2, 22-24] The mean-field approximation suggests that a second-order displacive phase transition is associated with a soft phonon. The temperature dependence of the soft phonon mode frequency is given by[2, 22]

$$\omega^2(T) \propto |T - T_C|, \qquad \text{for } T<T_C \qquad (3.1)$$

and it vanishes as the temperature approaches a transition temperature T_C. On the other hand, in the case of an order-disorder transition, no soft phonon is observed. Instead, a central peak is found to appear in the vicinity of T_C in low frequency Raman and Brillouin spectra.[25-27] Deviations from the soft mode picture of the phase transition has been reported in the system such as $SrTiO_3$[23] and KH_2PO_4[24] using inelastic scattering technique. In ferroelectric materials, appearance of central peak (CP) represents existence of a microscopic relaxation process related to the ferroelectric polarization. The intensity and line-width of a relaxation mode diverges near T_C. The relaxation time τ of a relaxation mode shows a critical slowing down with temperature.[2] In order to clarify the origin of ferroelectricity, it is important to know whether the transition is primarily displacive or order-disorder type.[26] In this context, Brillouin scattering is useful for understanding the lattice dynamics and also the phase transition mechanism. Relaxation phenomena could be directly probed by this method. In this respect, CP, which is the manifestation of the characteristic time scales of the polarization fluctuation of polar nano clusters, is found in the Brillouin spectrum. In order to understand the dynamics of polar nano cluster, the temperature dependence of the relaxation times of CP is often found to be useful. Furthermore, from the point of view of instrumental resolution, Fabry-Perot interferometer yields accurate lineshape of CP due to its high resolution ~0.2 GHz.

In this work, we have carried out detailed Raman spectroscopic studies of $NaNbO_3$ in the temperature range 10–300 K to study the antiferroelectric to ferroelectric transition both in cooling and heating cycles. The spectra are analyzed to obtain the temperature dependence of mode wavenumbers. The temperature dependence of integrated intensities of low as well as high wavenumber modes has been examined in detail to obtain information about coexistence and hysteresis. In addition, Brillouin scattering measurements were carried out on $NaNbO_3$ single crystal from ambient to 773 K to study the central peak across the anti-ferroelectric orthorhombic

($D_{2h}^{11}, Z = 8$) to anti-ferroelectric orthorhombic ($D_{2h}^{13}, Z = 24$) transition (P to R phase). Single crystals were grown by flux method. The spectra were analyzed using PeakFit (Jandel 4.12) software. The behaviours of the low-frequency Raman modes and the CP were obtained as a function of temperature. The temperature-dependence of the relaxation time was analysed to obtain the activation energy of the relaxation process.

3.2 Experimental details

A single phase polycrystalline $NaNbO_3$ sample was prepared by solid state reaction method. A mixture of Na_2CO_3 and Nb_2O_5 in stoichiometric ratio was calcined at 1123 K for 3 hrs. The powder was pressed into pellet and sintered at 1373 K for 3 hrs. Single phase of $NaNbO_3$ was confirmed from the X-ray diffraction analysis. Raman spectra were recorded in the back-scattering geometry using 350 mW power of the 488 nm line from an Ar ion laser. Spectra were recorded in the temperature range 10 -300 K using a closed cycle helium refrigerator (APD 202) during cooling and heating cycles. Scattered light was analyzed using a double monochromator (SPEX 14018) and detected using a photomultiplier tube (Hamamatsu R943-02) operating in the photon counting mode. The spectra were fitted to Lorenzian line shapes by using PeakFit software to determine the wavenumber, line-width and integrated intensity of the modes. The temperature dependence of the mode wavenumbers and the integrated intensities of the modes during cooling and heating cycles were analyzed to understand the phase transition and coexistence behavior of antiferroelectric and ferroelectric phases. Transparent and colourless single crystals of $NaNbO_3$ were grown by flux method with Na_2CO_3 and B_2O_3 as fluxes. The charge and fluxes were taken in the molar ratio 14.3($NaNbO_3$) : 40.5(Na_2CO_3) : 45.2(B_2O_3) mol%. The crystals were grown by cooling from 1448 to 1048 K at a rate of 1.5 K/h and then from 1048 K to ambient temperature at a rate of 100 K/h. The typical sample dimensions were 2×2×0.5 mm^3. The Perovskite phase was confirmed using powder X-ray diffraction analysis.

Laue pattern was obtained using Phillips X-ray generator with white spectrum from a Tungsten target. The pattern was recorded using an imaging plate and scanned in a home-built scanner to obtain a digital image. The surfaces were polished to optical quality. The Energy dispersive X-ray analysis of the sample was carried out using a scanning electron microscope (CARL ZEISS, SUPRA 55). Brillouin spectra were measured in backscattering geometry using a high-contrast 3+3-pass tandem Fabry-Perot interferometer (JRS Scientific Instruments). For probing CP, the spectra were recorded using a large free spectral range (FSR) of 3300 GHz in order to cover a wide frequency range. By choosing large FSR, the acoustic modes would lie in the cut-off region and hence only CP was present. In addition, the low frequency optical mode could also be detected. Sample was excited using 532 nm light using a single-mode diode-pumped solid state laser (Innolight Diabolo 500). The spectra were recorded from ambient to 773 K using a commercially available heating stage with a temperature stability of ±0.1 K. The measurements were performed at successively higher temperature during a heating cycle.

3.3 Results and discussion

3.3.1 Structural and microstructural characterization

Figure 3.1 shows the powder X-ray diffraction patterns of $NaNbO_3$. No impurity peaks were found and the observed reflections could be satisfactorily matched with those of the standard JCPDS card #33-1270, confirming formation of single phase compound with orthorhombic structure. The well-sintered nature of the sample was confirmed from the uniform distribution of grains as seen in the scanning electron micrograph (inset (a)) taken on the surface of sintered pellet. EDAX measurements were carried out on sintered pellet to study the chemical composition. The EDAX spectrum (inset (b)) of the sample shows the presence of all the cationic elements, which were in agreement with the expected stoichiometry within the experimental error.

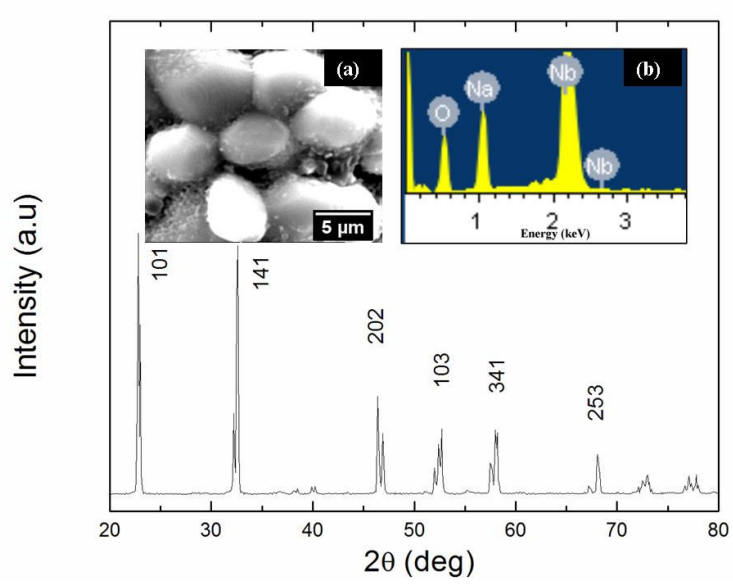

Figure 3.1 X-rays diffraction pattern of $NaNbO_3$. Inset (a) shows the SEM image and inset (b) shows EDAX spectrum.

3.3.2 Low temperature Raman spectroscopic results

The low temperature rhombohedral phase of $NaNbO_3$ has six formula units per unit cell (point group C_{3v}^6)[5] that results in 90 fundamental vibrational degrees of freedom. Out of them 3 constitute the acoustic mode and remaining contributes to the optical phonons. Group theoretical analysis of the rhombohedral phase has not been reported so far. Hence we have obtained the number of modes corresponding to each irreducible representation from factor group analysis. The optical phonons are: $\Gamma_{opt} = 20A_1 + 9A_2 + 29E$, where the A_1 and E modes are both Raman and Infrared active, whereas the A_2 mode is inactive both in Raman and Infrared. Hence 49 Raman-active phonons are expected. On the other hand, the ambient temperature orthorhombic phase (point group D_{2h}^{11}) has eight formula units per unit cell.[5] From the group theoretical analysis the irreducible representations of the vibrational modes of orthorhombic phase at room temperature as reported earlier are:[11] $\Gamma_{opt} = 15A_g + 17B_{1g} + 15B_{2g} + 13B_{3g} + 13A_u + 14B_{1u} + 16B_{2u} + 14B_{3u}$, where A_g, B_{1g}, B_{2g} and B_{3g} modes are Raman active, whereas the mode A_u is inactive both in Raman and Infrared and modes B_{1u}, B_{2u} and B_{3u} are only Infrared active. Hence 60 Raman-active optical phonons are expected.

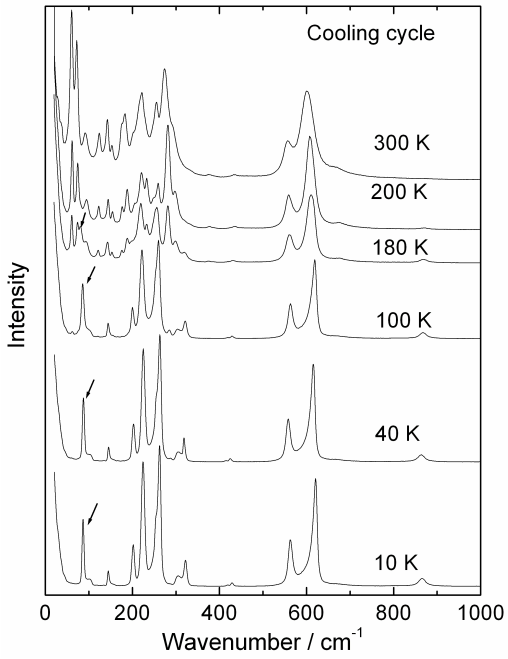

Figure 3.2 Raman spectra of $NaNbO_3$ at various temperatures during the cooling cycle. The new mode at 80 cm^{-1} is labeled using an arrow.

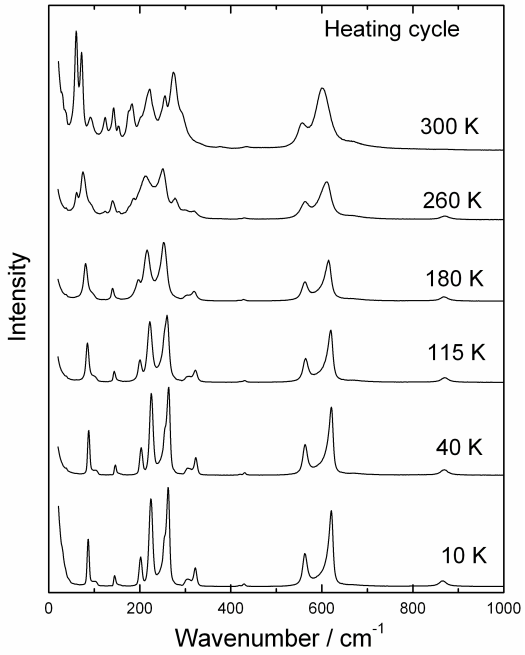

Figure 3.3 Raman spectra of $NaNbO_3$ at various temperatures during the heating cycle.

Figures 3.2 and 3.3 show the Raman spectra of $NaNbO_3$ at various temperatures during cooling and heating cycles, respectively. At room temperature a total of 19 distinct Raman modes were identified in the wavenumber range 30–950 cm^{-1}. The observed modes are less than the actually predicted one, which could be either due to accidental degeneracy of phonon

wavenumber or insufficient intensities arising from small polarizability of several modes. On the other hand, at 10 K, only 12 distinct Raman modes could be found in that same wavenumber range. The less number of modes at 10 K is due to higher symmetry of the rhombohedral phase. Table 3.1 lists the wavenumbers of observed Raman modes in the orthorhombic and rhombohedral phases. One can see that most of the modes in the orthorhombic phase have large temperature coefficients than those of the modes in the rhombohedral phase. This suggests that the anharmonicity of the AFE phase is higher than that of the FE phase. The bands appearing in the low-wavenumber range 50–100 cm^{-1} have been assigned to the external vibrations of Na ion and while in the range 100–180 cm^{-1} to the librations (rotational vibrations) of NbO_6 octahedra.[12] The wavenumber regime 160–950 cm^{-1} is associated with the internal vibrations of NbO_6 octahedra.[12]

The Raman spectra shown in Figs. 3.2 and 3.3 exhibit significant change upon passing through the antiferroelectric-ferroelectric transition in the temperature range from 10-300 K in cooling and also across the reverse transition in the heating cycle. The intensities of the several modes 60, 72, 123, 182, 274 and 556 cm^{-1} gradually decrease initially upon cooling and exhibit a marked change at 180 K. A new mode at 80 cm^{-1} also begins to appear at 180 K and its intensity increases continuously from 180 to 10 K during cooling. Furthermore, the intensity of the mode at 556 cm^{-1} increases monotonically during cooling and reaches a maximum at 10 K. In the heating cycle, as it can be seen from Fig. 3.3, the spectral features remains the same till 240 K. Above this temperature, the intensity of the modes at 60, 123, 182 and 274 cm^{-1} exhibit a large increase while that of the mode at 556 cm^{-1} exhibits a rapid drop in the intensity. These observations clearly indicate that the phase transition from antiferroelectric to ferroelectric phase occurs at 180 K on cooling while the reverse transition at 260 K upon heating. The observed reverse phase transition at 260 K is in contrast to the earlier reports.[12, 13]

Table 3.1 Wavenumbers of Raman bands at room temperature and 10 K. The numbers in the parenthesis are the standard errors in the least significant digit.

Orthorhombic phase 295 K (AFE)		Rhombhohedral phase 10 K (FE)	
Mode Wavenumber (cm^{-1})	*T*-coefficient (10^{-3} $cm^{-1}K^{-1}$)	Mode Wavenumber (cm^{-1})	*T*-coefficient (10^{-3} $cm^{-1}K^{-1}$)
60.1	-	-	-
72.1	-48(5)	86.6	-13(5)
92.2	-	-	-
123.6	22	-	-
142.4	-18(5)	144.9	-11(2)
153.7	-15	-	-
174.8	-	-	-
182.8	-20	-	-
201.5	-20(10)	201.3	4(6)
220.2	-39(9)	224.4	-19(4)
253.8	-40(7)	261	-22(4)
274.5	8	-	-
293.4	-22(10)	305.3	-44(5)
-	-	321.7	-4(7)
378.6	-	-	-
-	-	418.4	10(2)
433.7	7(6)	428.8	25(5)
555.9	-1(4)	563.3	-26(7)
601.7	-44(3)	619.3	-65(7)
674	0(1)	-	-
871.3	17(2)	865.7	17(5)

Figure 3.4 shows the dependences of mode wavenumbers on temperature during cooling cycle. Note the disappearance of a few modes and appearance of new modes at ~180 K as the sample undergoes the structural phase transition. Several modes of orthorhombic phase merge together due to transformation to higher symmetry rhombohedral phase. For some modes the intensities decrease and they merge with the background. Out of the 19 modes, only 12 could be followed up to 10 K in the rhombohedral phase (table 3.1). The dependence of mode wavenumbers on temperature during the heating cycle is shown in Fig. 3.5. Almost all modes of the rhombohedral phase continue to exist up to ~ 300 K during heating cycle. In addition, the

modes at 60, 123, 182 and 274 cm^{-1} that exhibited significant changes at 180 K during cooling cycle begin to reappear only at ~ 260 K during heating cycle. This suggests that in the heating cycle, the reverse transition occurs at 260 K.

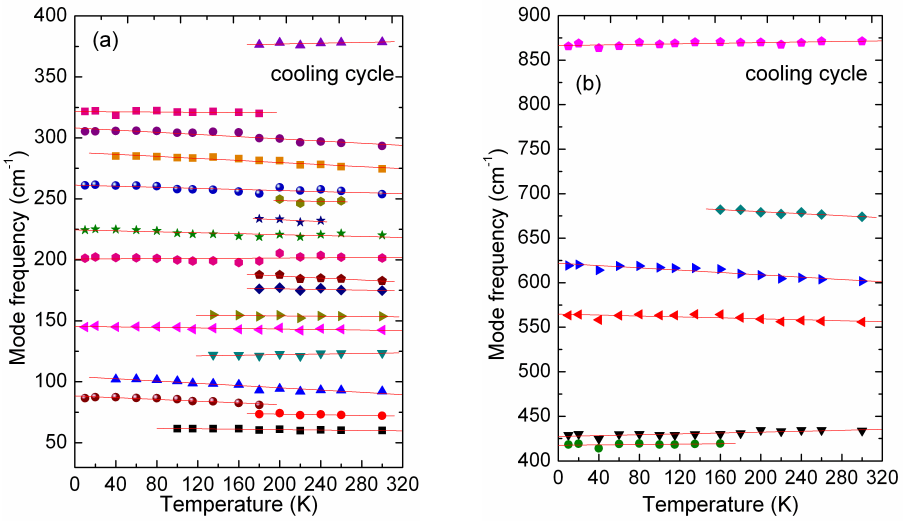

Figure 3.4 Temperature dependence of Raman modes during cooling cycle for (a) low and (b) high-wavenumber region. Straight lines are linear least square fits to the data.

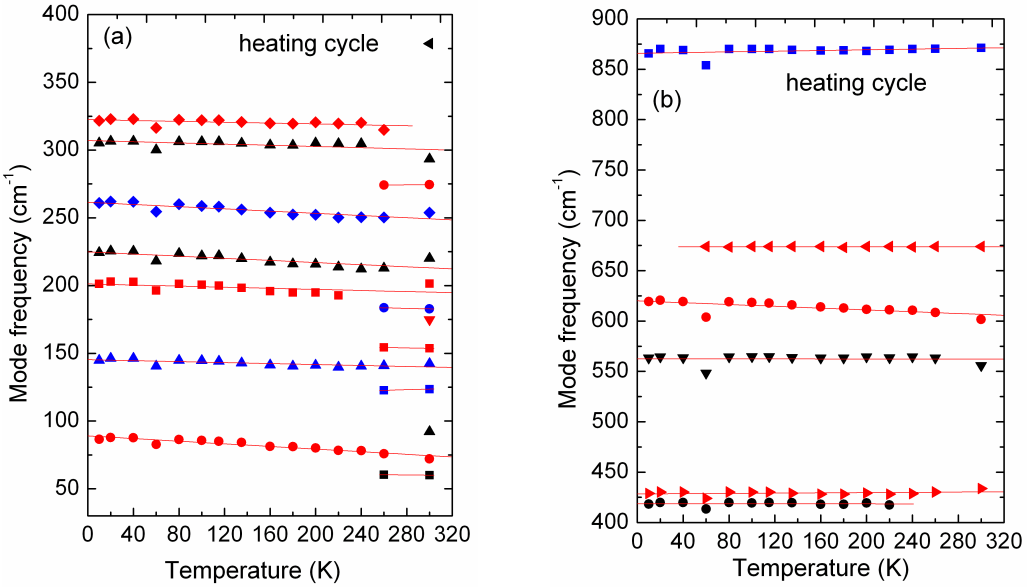

Figure 3.5 Temperature dependence of Raman modes during heating cycle for (a) low and (b) high-wavenumber region. Straight lines are linear least square fits to the data.

In analogy with the X-ray intensities, quantitative analyses of intensities of the Raman modes, that are unique to different phases, have been useful in obtaining phase fractions and regions of coexistence.[19, 20, 21] Hence the normalized integrated intensities of the modes 60, 123, 180, 274 and 556 $cm^{-1}$are investigated to understand the temperature range of coexistence of antiferroelectric and ferroelectric during cooling and heating cycles. The integrated intensities of the modes at 60, 123, 180, 274 and 556 cm^{-1} are normalized against the intensity of the mode at 601 cm^{-1}. This mode is associated with the symmetric stretching (ν_1) vibration of the NbO_6 group[12] and it persists both in cooling and heating cycle over the complete temperature range without much change in its intensity. Hence we use the intensity of this peak for normalization of the intensities of other modes. The temperature dependence of the intensities of these five modes are shown in Fig. 3.6. One can notice that the intensity of the mode 182 cm^{-1} (Fig. (3.6(c)) begins to exhibit a sharp decrease in the range of 220-180 K. Similarly the intensity of 274 cm^{-1} mode as shown in Fig 3.6(d), also shows a sharp decrease in the intensity in the temperature range 220–160 K. However, in the heating cycle, both 182 and 274 cm^{-1} modes begin to show a sharp increase in the temperature range 240–300 K. The behavior exhibited by the 182 and 274 cm^{-1} modes suggest that these are unique to orthorhombic phase and essentially represent the fraction of the orthorhombic phase. It should also be noted that both 60 and 123 cm^{-1} modes show a change in slope in the temperature range 220–160 K during cooling cycle. On the other hand, intensities of these modes exhibit a rapid rise in the temperature range 240–300 K during heating cycle. The intensity of 556 cm^{-1} mode on the contrary gradually increases during cooling. During heating, its intensity exhibits a small decrease till 260 K and a rapid fall above this temperature. These findings suggest that both anti-ferroelectric and ferroelectric phases coexist between 220 and 160 K during cooling cycle and between 240 and 300 K during heating cycle. It can be seen from the figure that these modes attain their full intensity in the heating cycle at 300 K. Also as it

can be seen from the Figs. 3.2 and 3.3 the spectral features at 300 K are same for both cooling and heating cycles. This suggests that the system transforms completely to anti-ferroelectric phase at 300 K.

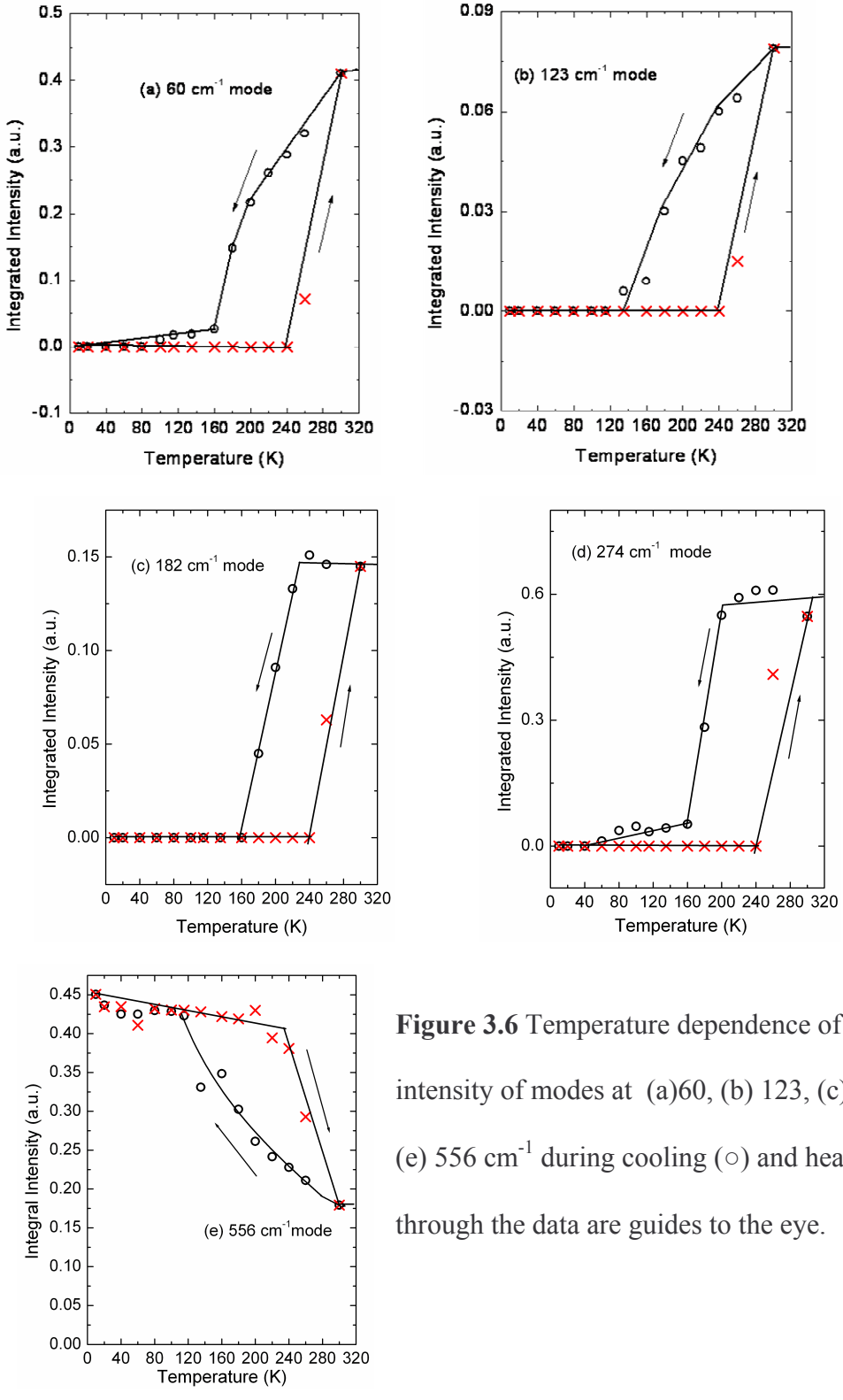

Figure 3.6 Temperature dependence of the integrated intensity of modes at (a)60, (b) 123, (c) 182, (d) 274, and (e) 556 cm^{-1} during cooling (○) and heating cycle (×). Lines through the data are guides to the eye.

The present observation of coexistence of both AFE and FE phases can be correlated with the respective structural distortions. In the high temperature paraelectric phase, both Na and Nb ions occupy the geometrical centre of cuboctahedral and octahedral positions respectively. The sequence of phase transition in $NaNbO_3$ is brought out by the tilt of NbO_6 octahedra and the displacement of Nb ion.[5] In the anti-ferroelectric phase NbO_6 octahedra are tilted in alternate manner and are described in the Glazer's notation as $a^-b^+a^-$ and $a^-b^-a^-$ while in the ferroelectric phase, the tilting is described by $a^-a^-a^-$.[28] The main difference between the antiferroelectric and ferroelectric phases with respect to the tilting is the absence of anti-phase tilting of NbO_6 along *b* axis in the latter phase. The modes 60 and 123 cm^{-1} is associated with the translation of Na ion and rotational (tilting) vibrations of NbO_6 octahedra respectively. As $NaNbO_3$ undergoes phase transition from AFE to FE at 180 K, Na ion gets displaced along the same axis due to the three axis tilt of NbO_6 octahedra and Nb ion gets shifted from the geometrical centre of the octahedra by 0.23 Å along the triad axis.[5] The similarity in the temperature dependence of the integrated intensity of 60 and 123 cm^{-1} modes clearly reflect changes in the direction of displacement of Na ion due to the changes in the direction of tilting of oxygen octahedra (loss of antiphase tilting). Therefore the gradual decrease (increase) in the intensity of 123 cm^{-1} mode and increase (decrease) in the intensity of 556 cm^{-1} mode during cooling (heating) cycle clearly reflects the gradual phase transition from anti-ferroelectric to ferroelectric phases. It is instructive to compare this phase transition behaviour of $NaNbO_3$ with other perovskite ferroelectrics. It is well known in the case of ABO_3 Perovskite ferroelectrics such as $BaTiO_3$, $PbTiO_3$ and $KNbO_3$, the ferroelectric phase is due to the displacement of Ti/Nb ions from its equilibrium position of oxygen octahedra. This displacement is strongly correlated such that a long range ferroelectric order is established and these materials show a normal FE behavior. On the other hand, in $PbZrO_3$ paraelectric to antiferroelectric phase transition at 508 K is brought out by anti-parallel

displacement of Pb ion from its equilibrium position.[29] This anti-parallel displacement of Pb ion arises from the tilt of ZrO_6 octahedra at the phase transition temperature.[29] However a long range ferroelectric state (as in the case of $KNbO_3$) or anti-ferroelectric state (as in the case of $PbZrO_3$) could not be established due to the competing AFE and FE phases arising from the tilting of oxygen octahedra and the displacement of Nb ions. In the present study, the competing interactions between AFE and FE phases are clearly reflected in the hysteresis behaviour of low frequency modes involving the translation motion of Na ion, librations of NbO_6 octahedra and high frequency modes associated with the internal vibrations of NbO_6 octahedra. The competing AFE and FE phases lead to the smearing of the dielectric response and exhibit relaxor like behaviour as in the case of $(Sr_{1-x}Ca_x)TiO_3$.[30] In $NaNbO_3$ a relaxor like behaviour was observed in the low temperature range.[31] On the other hand, disorder due to hopping between equivalent off-center cation sites occurs near P-R transition at 643 K.[11]

3.3.3 Brillouin spectroscopic results on $NaNbO_3$ single crystal

Figure 3.7(a) shows the X-ray diffraction pattern of the powdered crystals of $NaNbO_3$. All the diffraction peaks match with the standard JCPDS card #33-1270 confirming formation of a single phase with orthorhombic structure. Energy dispersive X-ray analysis on single crystal confirmed the presence of all the cationic elements in agreement with expected stoichiometry within experimental error. Figure 3.7(b) shows the Laue patterns of $NaNbO_3$ single crystal. The orientation of the crystal was found by generating theoretical patterns using software (Orient express 3.3 application). The simulated patterns were matched with the experimental pattern to determine the crystal orientation. It was found that the pattern matched with that for (0 -1 0) direction.

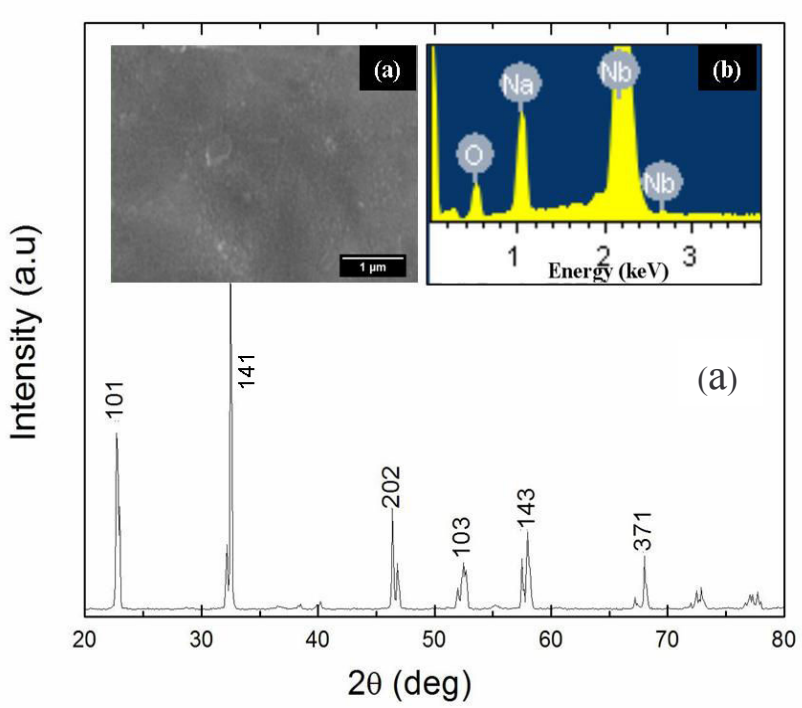

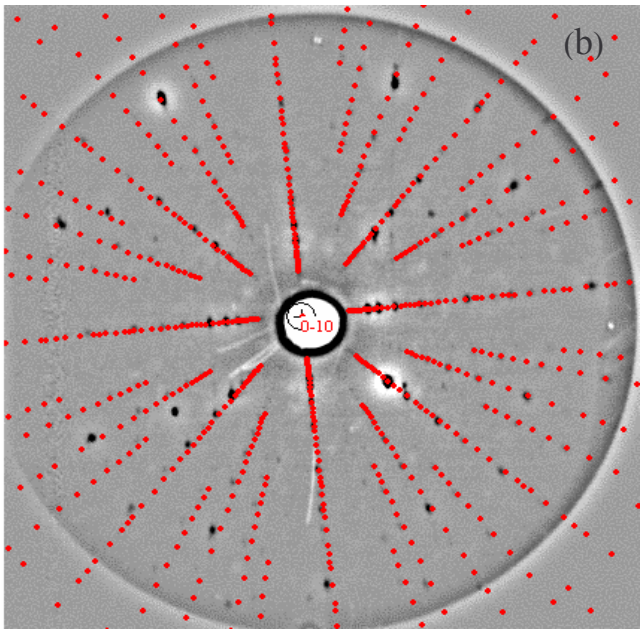

Figure 3.7 (a) X-rays diffraction pattern of $NaNbO_3$ single crystal powder at ambient. Inset (a) shows the SEM image and inset (b) shows the EDAX spectrum (b) Laue pattern on $NaNbO_3$ single crystal confirming the [0 -1 0] orientation. Black dots represent experimental pattern, Red dots constitute the theoretically simulated pattern.

Figure 3.8 shows the Brillouin spectra at selected temperatures. A broad central peak (CP) was found to appear above 493 K. Upon heating it became weak and vanished above 743 K. The appearance of CP is evident from the change in line shape and the slope of the low frequency scattering below 1500 GHz. It can be pointed out that Brillouin spectroscopy has not

been employed earlier to study the CP in $NaNbO_3$. Therefore a quantitative analysis is necessary to study the behaviour of CP.

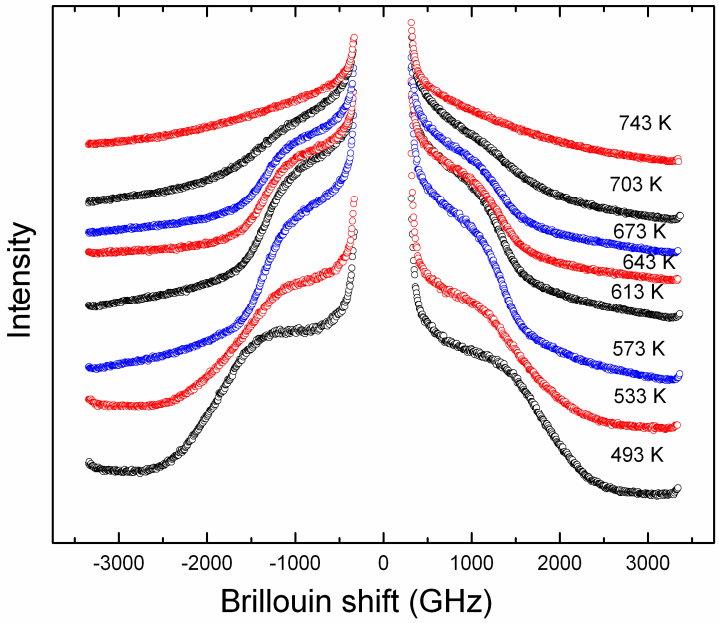

Figure 3.8 Brillouin spectra of $NaNbO_3$ measured using a FSR of 3300 GHz at selected temperatures.

In the damped oscillator model, the spectral response $I(\omega)$ of optical modes is given by

$$\frac{I(\omega)}{F(\omega,T)} = \sum \frac{C_j \omega_j^2 \Gamma_j}{\left(\omega_j^2 - \omega^2\right)^2 + \omega^2 \Gamma_j^2}, \qquad (3.2)$$

where $I(\omega)$ is the experimental scattered intensity, C_j, ω_j and Γ_j are the intensity factor for the oscillator j, the frequency and damping of j^{th} phonon, respectively. The thermal population factor is $F(\omega,T) = n(\omega,T) = \left(\frac{1}{\left(\exp^{\hbar\omega/k_BT}\right)-1}\right)$ or $F(\omega,T) = n(\omega,T)+1$ for the anti-Stokes or Stokes components of the spectrum, respectively. The intensity is divided by the thermal population factor to eliminate the contribution of temperature on the intensity of Brillouin spectra. On the other hand, for a relaxation process, the spectral response $I(\omega)$ is usually approximated by the Debye relaxation, $\frac{I(\omega)}{F(\omega,T)} = \frac{C_R \upsilon_r}{\omega^2 + \upsilon_r^2}$; where C_R is the relaxator strength

and υ_r is the inverse relaxation time. We analyse the spectra from 463 K to 773 K to a sum of damped harmonic oscillators and a relaxation mode under the assumption that the CP arises from a Debye relaxation and that it does not couple with the low frequency phonon. In a recent study on $LiNbO_3$,[32] light scattering spectra were analysed using the same assumption. However, we will test the validity of the assumption in a later discussion. Figure 3.9 shows the examples of the fit for a few selected temperatures. A good agreement between the data and calculated spectra is evident from the figure.

The frequencies and damping of the phonons are plotted in Figs. 3.10(a) and 3.10(b). One can see that the mode frequencies and the damping of phonon mode-1 and mode-2 remain constant up to 680 K and begin to increase only above this temperature, while T_C is only 643 K. No evidence of any anomaly or mode softening is observed around T_C. On the other hand, as mentioned in the introduction, for a displacive transition a softening of the type given by Eq.(3.1) is expected. Thus the present behaviour does not support a displacive mechanism.

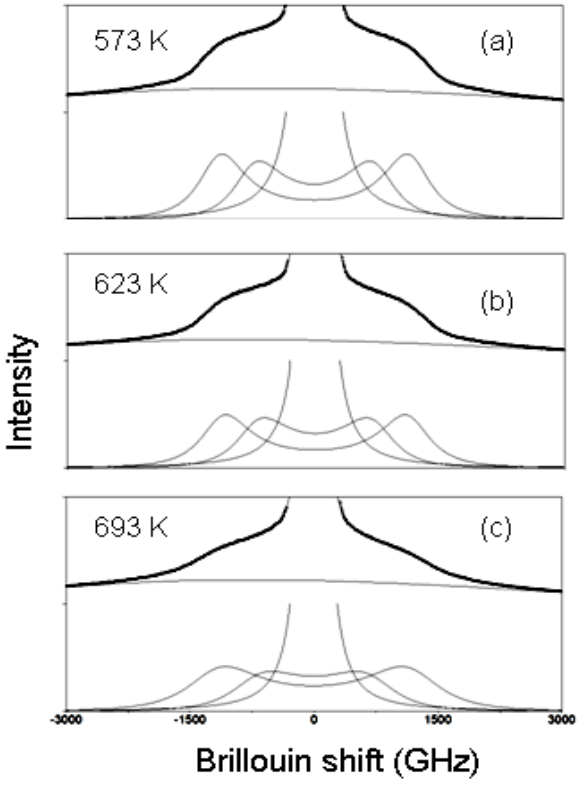

Figure 3.9 Brillouin spectra fitted to a sum of damped harmonic oscillators and a Debye relaxation mode at selected temperatures (a) 573K, (b) 623 K and (c) 693 K. The total fitted spectrum and individual calculated peaks are also shown.

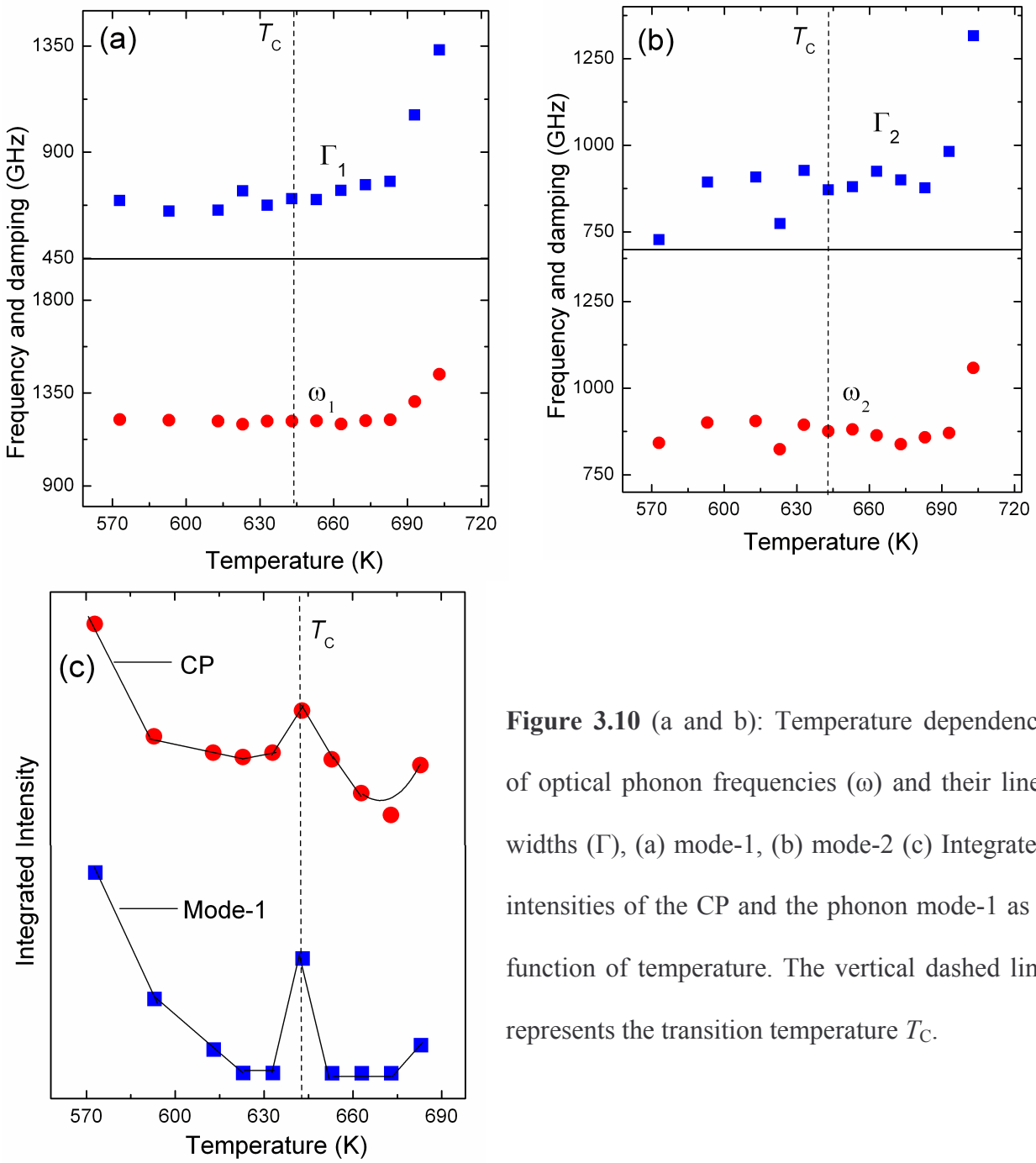

Figure 3.10 (a and b): Temperature dependence of optical phonon frequencies (ω) and their line-widths (Γ), (a) mode-1, (b) mode-2 (c) Integrated intensities of the CP and the phonon mode-1 as a function of temperature. The vertical dashed line represents the transition temperature T_C.

As mentioned in the introduction, presence of central peak in Brillouin spectrum is an evidence of relaxation processes in the system. CP has been found in low-frequency Raman spectra also.[11, 25] CP can originate either from static or from dynamic fluctuations. An elastic

unresolved and temperature independent CP arises due to fluctuations of static nature whereas the dynamic fluctuations result in a relatively broad and temperature dependent CP. Several different dynamic mechanisms such as entropy and phonon density fluctuations, ion hopping, tunnelling, precursor clusters have been argued to result in the appearance of CP.[33, 34] One of the widely accepted mechanism is that of temperature-dependent dynamical polar fluctuations.[35, 36] Raman scattering studies on several classical pure ferroelectric $NaNbO_3$,[11] $KNbO_3$,[37] $LiNbO_3$,[25] anti-ferroelectric $PbZrO_3$,[38]and $AgNbO_3$[39] and other mixed Perovskite compounds such as $KTa_{1-x}Nb_xO_3$[40] and Brillouin scattering studies on ferroelectric $BaTi_2O_5$[26] and $KTa_{1-x}Nb_xO_3$[41] have exhibited the CP. For a Debye relaxation process the CP has a Lorenzian-type shape centered at the zero-frequency shift.

The integrated intensities of the central peak and the low frequency phonon modes are calculated using $K = \int_a^b \frac{I(\omega)}{F(\omega,T)} d\omega$; where *a* and *b* are the low and high frequency limits of the peak respectively. Figure 3.10(c) shows the plot of integrated intensities of CP as well as that of phonon mode-1. Upon heating, the integrated intensity of both CP and phonon mode-1 show gradual decrease up to 622 K and then exhibit dramatic increase as the temperature approaches T_C. The maxima for both the intensities occur at the same temperature that corresponds to the P-R phase transition temperature T_C = 643 K, in agreement the previous Raman investigations.[11] The two features exhibiting similar behaviour with temperature suggests that no intensity transfer occurs between the CP and phonon mode, and validates the earlier assumption of no coupling between the two.

Figure 3.11(a) shows the temperature dependence of the relaxation time (τ) obtained from single Debye relaxation mode-fitting as discussed earlier. One can see that the relaxation time remains constant up to 593 K and then increases rapidly (diverges) as the temperature

approaches T_C. The inverse relaxation time in the vicinity of T_C is shown in Fig. 3.11(b). One can notice that below T_C, the inverse relaxation time is approximately proportional to $|T - T_C|$. This can be attributed to a critical slowing down associated with an order-disorder phase transition.[2] Therefore, the transition mechanism appears to be order-disorder type.

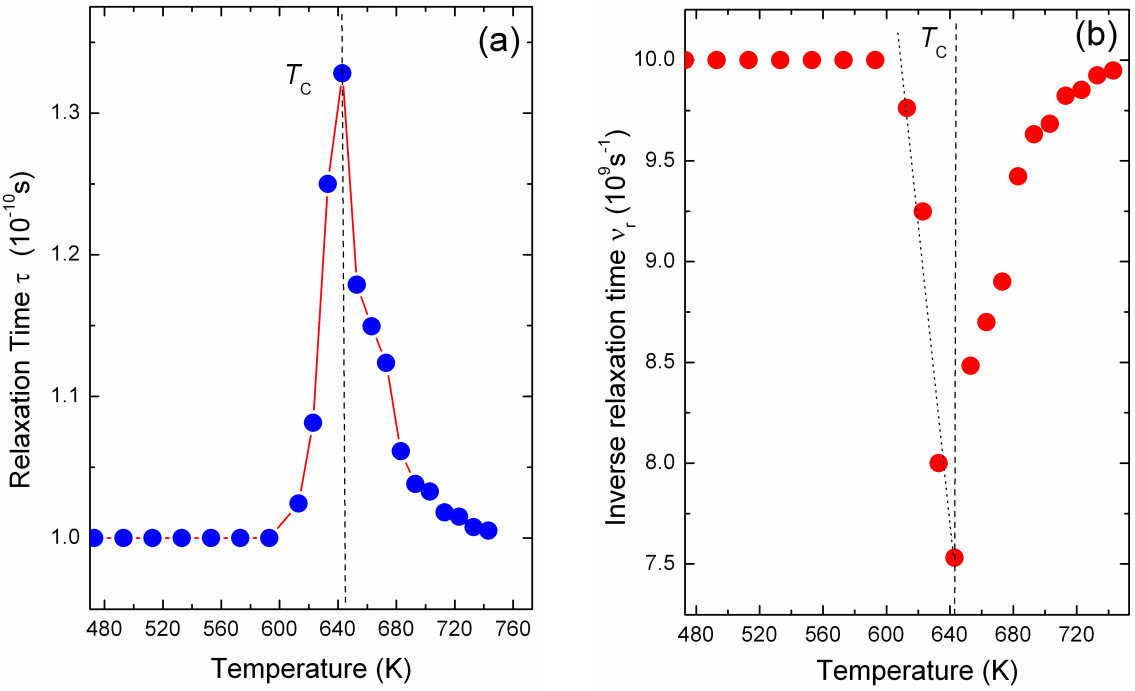

Figure 3.11 (a) The relaxation time τ(T) and (b) the inverse relaxation time $\upsilon_r(T)$ as a function of temperature. The vertical dashed line represents the transition temperature T_C. Dotted straight line in (b) represents linear dependence of τ^{-1} on $|T - T_C|$ near T_C.

It has been argued that the temperature-dependence of the width of the central peak can be understood using a semi classical eight-site order-disorder model.[40] The model has been used for explaining the relaxation modes in ABO_3 type Perovskite ferroelectric materials. According to this, the thermally excited *B*-ion gets disorder between its normal sites and the normally

vacant eight sites. The hopping rate of *B*-ion between different sites leading to the relaxation process is governed by the activation barrier between the sites. The relaxation time in this case can be written as

$$\tau = \tau_o \exp(\Delta V/k_B T), \qquad (3.3)$$

where ΔV is the activation energy of the *B*-ion needed to hop from one well to another. Figure 3.12 shows Arrhenius plot of the relaxation time using Eq.(3). The slope of the fitted line yields $(\Delta V/k_B)$ = 1224±125 K, which in turn gives the activation energy as 105±10 meV. A similar magnitude of activation energy was found for other ferroelectrics, for example, 98±6 meV for $LiTaO_3$.[27]

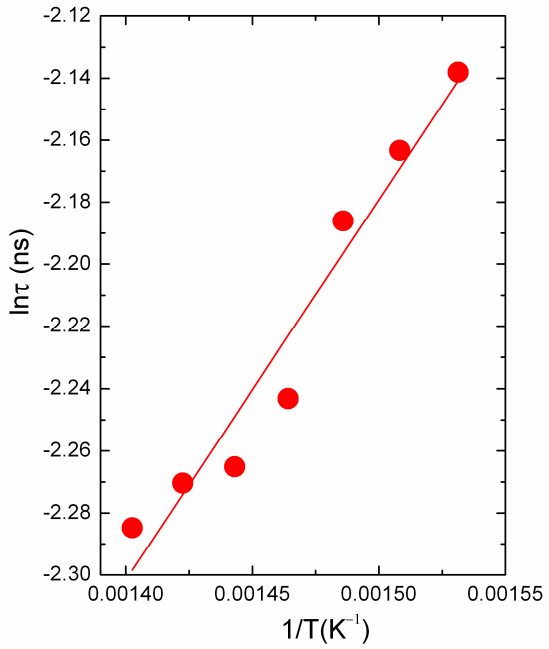

Figure 3.12 Logarithmic relaxation time (τ) versus $1/T$. The solid line is the fit using hopping model.

3.4 Summary and conclusions

The aniferroelectric to ferroelectric phase transition in $NaNbO_3$ was studied using Raman spectroscopy. The detailed analysis of the Raman data indicated that the transition from antiferroelectric to ferroelectric phases occurs at 180 K during cooling and the reverse transition at 260 K during heating cycles. The transition is found to be a two step process involving

coexistence of both phases in the intermediate temperatures during cooling and heating cycles. Both antiferroectric and ferroelectric phases are found to coexist between 220 K to 160 K during cooling cycle and 240 K to 300 K during heating cycle. The present analysis of the intensities of the modes suggests that the coexistence region and the reverse transition temperature are different from those reported earlier. The coexistence of phases is probably related to simultaneous structural distortion caused by displacement of Na and Nb ions from its equilibrium position.

Transparent and colourless single crystals of $NaNbO_3$ were grown by flux method. The central peak in both P and R phases and across the P-R phase transition at 643 K has been investigated using Brillouin scattering. An anomaly around 643 K is found from the temperature dependence of its integrated intensities and relaxation times suggesting the phase transition to be order-disorder type. The activation energy for hopping of Nb ion between allowed and vacant sites is estimated to be ~105 meV.

References

1. Lead Free Piezoceramics Based on Alkaline Niobates, EU-funded project GRD1-2000-25682 (Fifth framework Project: Mar, 1, 2001 to Feb. 29, 2004).
2. M. E. Lines and A. M. Glass 1977 *Principles and Applications of Ferroelectrics and Related Materials* (Oxford: Clarendon).
3. E. Cross, Nature (London) **432**, 24 (2004).
4. Y. Saito, H.Takao, T.Tani, T. Nonoyama, K.Takatori, T. Homma, T. Nagaya, and M. Nakamura, Nature (London) **432**, 84 (2004).
5. C. N. W. Darlington and H. D. Megaw, Acta Cryst. B**29**, 2171 (1973)**.**
6. Yu. I. Yuzyuk, P. Simon, E. Gagarina, L. Hennet, D. Thiaudiere, V. I. Torgashev, S. I. Raevskaya, I. P. Raevskii, L. A. Reznitchenko, and J. L. Sauvajol, J. Phys. Condens. Matter **17**, 4977 (2005).
7. V. A. Shuvaeva, Y. Azuma, K. Yagi, K. Sakaue, and H. Terauchi, J. Synchrotron Radiat. **8**, 833 (2001).
8. J. Chen, D. Feng, Phys. Status Solidi *A* **109**,171, 1988; **109**, 427 (1988).
9. A. Avogadro, G. Bonera, F. Borsa, and A. Rigamont, Phys. Rev. B **9**, 3905 (1974).
10. G. D'Ariano, S. Aldrovandi, and A. Rigamonti, Phys. Rev. B **25**, 7044 **(**1982); S. E. Ashbrook, L. Le Polles, R. Gautier, C. J. Pickard, and R. I. Walton, Phys. Chem. Chem. Phys.**8**, 3423, 2006.
11. E. Bouziane, M. D. Fontana, and M. Ayadi, J.Phys. Condens. Matter. **15**, 1387 (2003).
12. Z. X. Shen, X. B. Wang, M. H. Kuok, and S. H. Tang, J. Raman Spectrosc. **29**, 379 (1998).
13. S. K. Mishra, N. Choudhury, S. L. Chaplot, P. S. R. Krishna, and R. Mittal, Phys. Rev. B **76**, 024110 (2007).

14. R. J. C. Lima, P. T. C. Freire, J. M. Sasaki, A. P. Ayala, F. E. A. Melo, J. Mendes Filho, K. C. Serra, S. Lanfredi, M. H. Lente, and J. A. Eiras, J. Raman Spectrosc. **33**, 669 (2002).
15. S. J. Lin, D. P. Chiang, Y. F. Chen, C. H. Peng, H. T. Liu, J. K. Mei, W. S. Tse, T. -R. Tsai, and H.-P. Chiang, J. Raman Spectrosc. **37**, 1442 (2006).
16. Y. Shiratori, A. Magrez, W. Fischer, C. Pithan, and R. Waser, J. Phys. Chem. C **111**, 18493 (2007).
17. L. G. Tejuca and J. L. G. Fierro, *Properties and Applications of Perovskite -Type Oxides,* Dekker, New York, 1993.
18. G. Shirane, R. E. Newman, and R. Pepinsky, Phys. Rev. **96**, 581 (1954) and references therein.
19. A. Slodczyk, P. Colomban, and M. Pham-Thi, J. Phys. Chem. Solids **69**, 2503 (2008).
20. P. Colomban, and A. Slodczyk, Optical Materials **31**, 1759 (2009).
21. T. R. Ravindran, V. Sivasubramanian, and A. K. Arora, J. Phys. Condens. Matter **17**, 277 (2005).
22. W. Cochran, Phys. Rev. Lett. **3**, 412 (1959).
23. T. Riste, E. J. Samuelsoen, K. Olsen, and J. Feder, Solid State Commun. **9**, 1455 (1971).
24. R. A. Cowley, G. J. Coombs, R. S. Katiyar, J. F. Ryan, and J. F. Scott, J. Phys. C **4**, L203 (1971).
25. A. Ridah, M. D. Fontana, and P. Bourson, Phys. Rev. B **56**, 5967 (1997).
26. A. Hushur, H. Shigematsu, Y. Akishige, and S. Kojima, Appl. Phys. Lett. **86**, 112903 (2005).
27. A. Hushur, S. Gvasaliya, B. Roessli, S. Lushnikov, and S. Kojima, Phys. Rev. B **76**, 064104 (2007).

28. Yu. I. Yuzyuk, E. Gagarina, P. Simon, L. A. Reznitchenko, L. Hennet, and D. Thiaudiere, Phys. Rev. B **69**, 144105 (2004).

29. R. W. Whatmore and A. M. Glazer, J. Phys. C: Solid State Phys. **12**, 1505 (1979).

30. R. Ranjan, D. Pandy, and N. P. Lalla, Phys. Rev. Lett. **84**, 3726 (2000).

31. S. Lanfredi, M. H. Lente, and J. A. Eiras, Appl. Phys. Lett. **80**, 2731 (2002).

32. N. V. Surovtsev, A. M. Pugachev, V. K. Malinovsky, A. P. Shebanin, and S. Kojima, Phys. Rev. B **72**, 104303 (2005).

33. Y. Tsujimi, T. Matsui, H. Furuta, and T. Yagi, Phys. Rev. B **59**, 28 (1999).

34. J. P. Sokoloff, L. L. Chase, and D. Rytz, Phys. Rev. B **38**, 597 (1988).

35. A. F. Penna, A. Chaves, and S. P. S. Porto, Solid State Commun. **19**, 491 (1976).

36. A. F. Penna, S. P. S. Porto, and E. Wiener-Avnear, Solid State Commun. **23**, 377 (1977).

37. M. D. Fontana, A. Ridah, G. E. Kugel, and C. Carabatos-Nedelec, J. Phys. C: Solid State Phys. **21**, 5853 (1988).

38. K. Roleder, M. Maglione, M. D. Fontana, and J. Dec, J. Phys.: Condens. Matter **8,** 10669 (1996).

39. A. Kania, K. Roleder, G. E. Kugel, and M D Fontana, J. Phys. C: Solid State Phys. **19**, 9 (1986).

40. J. P. Sokoloff, L. L. Chase, and L. A. Boatner, Phys. Rev. B **41**, 2398 (1990).

41. R. Ohta, J. Zushi, T. Ariizumi, and S. Kojima, Appl. Phys. Lett. **98**, 092909 (2011).

Chapter 4

Brillouin and Raman spectroscopic studies on phase transition in relaxor Ferroelectric PZN-PT single crystal

4.1 Introduction

Lead-based relaxor ferroelectric materials have attracted the scientific community from the point of view of fundamental physics as well as industrial application.[1-6] Relaxor ferroelectrics are characterized by high dielectric constant, slim hysteresis loop, and broad frequency and temperature dependent dielectric maximum indicative of multiple scales of relaxation. In the high temperature paraelectric phase, the cations are expected to move freely among the available equivalent off-center positions in the cell and hence the crystal has an average $Pm\bar{3}m$ structure.[7] The occupation of the *B*-site by cations of different atomic radii and valencies can lead to the formation of chemically ordered nano-regions with $Fm\bar{3}m$ symmetry.[8-10] Therefore in a paraelectric state the symmetries of the chemically ordered and disordered regions are $Fm\bar{3}m$ and $Pm\bar{3}m$, respectively.[11,12] Upon cooling, the correlation between the off-center cations gives rise to the formation of polar nano regions (PNRs). The temperature evolution of PNRs is characterized by three temperatures.[13] Below the Burns temperature T_B, the nucleation of PNRs begins. In addition, at this temperature, the lifetime of PNRs exceeds the period of the optical phonon and are in quasi-dynamic state.[13] At an intermediate temperature T^* the originally formed PNRs coalesce to form large PNRs or in other words, the T^* marks the appearance of static or permanent correlations of the off-center ion displacements.[13,14] Finally at freezing temperature (T_F/T_C), the off-center ions are arrested in one position. At T_F, PNRs becomes static for a canonical relaxor or undergo a transition to normal ferroelectric state at the Curie temperature T_C for relaxors, which develop long-range ferroelectric order.[14] (1-*x*)$Pb(Zn_{1/3}Nb_{2/3})$-*x*($PbTiO_3$) (1-

x)PZN-*x*PT relaxor ferroelectrics are known to possess excellent piezoelectric and dielectric properties.[15] The (1-*x*)PZN-*x*PT solid-solutions belong to the family of Perovskite structure. The sublattice *A* is occupied by Pb^{2+} ions and the *B*-site is randomly occupied by Zn^{2+}, Nb^{5+}, and Ti^{4+} ions. The individual components of the solid-solution are different in their structural behaviour. PZN is a relaxor ferroelectric. It undergoes a sequence of phase transition from high temperature cubic to rhombohedral phase at low temperature with an intermediate relaxor state consisting of PNRs embedded in a non-polar matrix.[16,17] On the other hand, PT is a well known classical ferroelectric material and shows a cubic to tetragonal phase transition. The doping of PT in PZN influences the structural and relaxor properties.[11,18] The phase diagram of the (1-*x*)PZN-*x*PT shows a sequence of structural phases with temperature and the composition *x* of PT. For $x \leq 8\%$ the crystals show rhombohedral symmetry whereas for x = 11-15%, crystals are found to be in tetragonal phase with increasing lattice anisotropy with *x*. For x = 15%, which is located away from the morphotropic phase boundary (MPB), the system exhibits tetragonal–cubic phase transition around 490 K[18] and shows relaxor ferroelectric character.[18]

In order to understand the microscopic origin of the complex behavior of relaxor ferroelectric materials, different theoretical models have been proposed.[4-6] It is widely accepted that the central feature to the complex behavior in these materials is the nucleation and growth of the PNRs. The PNRs possess local and randomly oriented finite ferroelectric polarizations. Obtaining an understanding of such nanoscopic PNRs and their consequences on macroscopic properties such as ferroelectric phase transition has been addressed in many studies.[19-25] Because of formation of PNRs a deviation from Curie-Weiss law is also found below T_B.[26-28] In order to understand the dynamical aspects of PNRs many investigations such as dielectric spectroscopy, neutron scattering, far-infrared transmission spectroscopy, Raman and Brillouin spectroscopy have been carried out on many relaxor systems.[19,20,29-34] A central peak in the Brillouin spectrum

has been reported to arise due to relaxation dynamics of PNRs. In addition, other manifestation of dynamical features is the coupling of strain and polarization fluctuations leading to a softening of the acoustic phonon.[29-32]

In the present work, we focus on the Brillouin and Raman spectroscopic study of tetragonal-cubic phase transition and the dynamical behaviour of the PZN-PT single crystal over a wide range of temperature. As mentioned earlier, the phase diagram of the (1-*x*)PZN-(*x*)PT solid solution shows a sequence of structural phases with temperature and PT content.[18] Brillouin studies on (1-*x*)PZN-(*x*)PT below and around the MPB composition[18] have been reported earlier.[19,20,35,36] Systems with $x = 4.5$[21] and 7%[20] show typical relaxor character, whereas occurrence of long-range ferroelectric order was found at $x = 9\%$.[21] However, the solid solution far away from MPB such as that for $x = 15\%$ has not been investigated yet. Since the increase in PT content influences the structural[18] and relaxor behaviour,[37,38] it is also expected to modify the central peak and the acoustic phonon mode. Furthermore, it is of interest to examine the differences in the behaviours of solid solutions near and away from MPB. Such study on a broad compositional range is expected to improve the understanding of relaxation dynamics of PNRs. Raman spectroscopy is known to be a sensitive technique for studying phase transitions and short-range order in Perovskite ferroelectric crystals.[12,39-41] Phonon anomalies induced by temperature changes are associated with phase transitions.[39-43] Furthermore, it has the advantage that light couples directly with the ferroelectric order parameter (polarization) and is therefore useful in the study of PNR dynamics also.[13,14,44-46] Raman spectroscopic studies have been carried out for $x = 4.5\%$,[11] which is on the rhombohedral side of the phase diagram and also for $x = 8\%$,[47,48] 9%,[49] and 10%,[12] which are at the MPB. To our knowledge polarized *micro*-Raman study on PZN-PT with temperature across tetragonal-cubic phase transition has not been reported

which is on the tetragonal side of phase diagram. Since the increase in PT content influences the structural and relaxor behaviour,[11,13] it is expected to reflect in phonon spectra also.

The aim of the present work is to study the behaviour of acoustic phonon and the central peak across tetragonal-cubic phase transition and the dynamical behaviour of PNRs in $Pb(Zn_{1/3}Nb_{2/3})_{0.85}Ti_{0.15}O_3$ single crystal. In addition polarized *micro*-Raman spectroscopy has been employed in the temperature range 298-873 K to study the behaviour of phonon across tetragonal-cubic phase transition. Single crystals were synthesized by flux method and relaxor-like behavior was examined using dielectric spectroscopy.

4.2 Experimental details

Transparent and yellow coloured single crystals of $Pb(Zn_{1/3}Nb_{2/3})_{0.85}Ti_{0.15}O_3$ were grown by flux method with Pb_3O_4 as flux. The charge and flux were taken in 40:60 ratio by weight. The crystals were grown by cooling from 1473 to 1203 K at a rate of 0.8 K/h and then from 1203 K to room temperature at a rate of 300 K/h. The confirmation of Perovskite phase was obtained using X-ray diffraction analysis. The typical sample dimensions were $3\times2\times0.5$ mm^3. The surfaces were polished to optical quality. The Energy dispersive X-ray analysis of the sample was carried out using a scanning electron microscope (CARL ZEISS, SUPRA 55). The dielectric parameters (capacitance and dissipation factor) were measured over a range of frequencies (2 kHz to 1 MHz) using a computer–controlled LCR meter/ impedance analyzer (PSM: N4L (Model: 1735, UK)) in the temperature range 300-585 K. Brillouin spectra were measured in backscattering geometry using a high-contrast 3+3-pass tandem Fabry-Perot interferometer (JRS Scientific Instruments). The sample was excited using 532 nm light using a single-mode diode-pumped solid state laser (Diabolo 500). The spectra were recorded using the free spectral ranges (FSR) of 100 and 400 GHz in the temperature range 300-873 K using a commercially available heating stage with a stability of ± 0.1 K. The exact sample temperature was monitored using a

thermocouple placed adjacent to the sample inside the heating stage. The measurements were performed at successively higher *T* during heating cycle. Raman spectra were recorded using a Ranishaw *micro*-Raman spectrometer (model InVia) equipped with a Leica microscope and a 20× long-working distance objective. The measurements were conducted in backscattering geometry using the 514.5 nm line of an Ar-ion laser. The spectrometer resolution for 1800 l/mm grating was ~1.5 cm^{-1}. The *in-situ* temperature-dependent experiments were carried out using a Linkam heating-cooling stage ensuring a temperature stability of ± 0.1 K. Data acquisition time and the laser power were adjusted for obtaining a good signal to noise ratio. Polarized Raman spectra were measured from 298 to 873 K in $X(YY)X'$ (VV) and $X(YZ)X'$ (VH) scattering geometries (Porto's notation), where X, Y and Z are parallel to the tetragonal [100], [010] and [001] crystallographic directions, respectively. The spectra were fitted to Lorenzian line shapes to determine the peak positions, full widths at half maximum (FWHM) and integrated intensities, using PeakFit software (JANDEL).

4.3 Results and discussion

4.3.1 Structural and dielectric studies

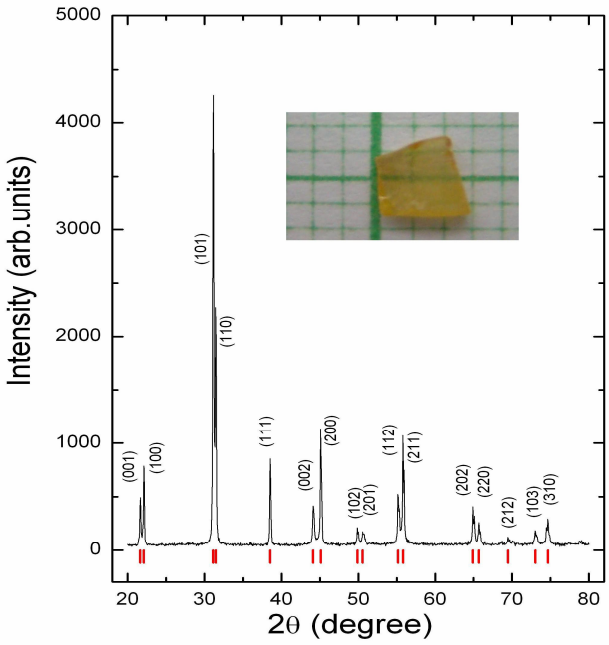

Figure 4.1 Powder X-rays diffraction pattern of PZN-PT crystal (x = 0.15). The tick pattern is the calculated peak positions for the tetragonal phase (*P4mm*). Inset shows a photograph of the single crystal.

Figure 4.1 shows the X-ray diffraction pattern of the powdered crystals of PZN-PT. All the diffraction peaks could be indexed to the tetragonal crystal system with space group *P4mm*, with lattice parameters a = 4.0165(6) Å, c = 4.1027(9) Å, and V = 66.184(16) Å^3. The tick pattern shown at the bottom of the figure is the calculated peak positions for the tetragonal phase. These lattice parameters are in good agreement with those reported in the phase diagram data on (1-x)PZN-xPT,[18] for x = 0.15. Energy dispersive X-ray analysis on single crystal confirmed the presence of all the cationic elements in agreement with expected stoichiometry within experimental error.

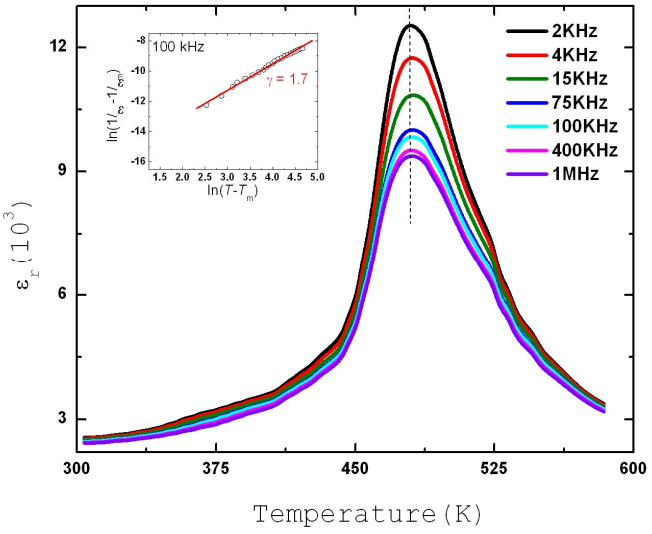

Figure 4.2 Temperature dependence of the dielectric constant (ε_r) of PZN-PT single crystal measured at different frequencies. Inset: log(1 / ε_r - 1 / ε_{max}) as a function of log(T - T_m). Straight line is a linear fit to the data.

Figure 4.2 shows the variation of dielectric constant (ε_r) with temperature at different frequencies. The dielectric constant exhibited only one dielectric anomaly/peak in the temperature range of investigation. The dielectric peaks observed around T_m ~480 K exhibit a clear but weak frequency dispersion. This dielectric anomaly (peak) can be attributed to the ferroelectric to paraelectric phase transition (i.e., tetragonal-cubic phase). In order to find the order of diffusivity of phase transition, the high temperature side of the dielectric peak was fitted with the modified Curie-Weiss law,[50]

$$1/\varepsilon_r - 1/\varepsilon_{max} = (T-T_m)^{\gamma}/C, \qquad (4.1)$$

where γ is the diffusivity and C is the Curie-Weiss constant, and ε_{max} is the maximum value of ε_r at T_m. The value of γ is estimated from the slope of log $(1/\varepsilon_r - 1/\varepsilon_{max})$ versus log $(T-T_m)$ plots. We obtained the parameter γ as 1.7 from fitting the data at 100 kHz, as shown in inset of Fig. 4. 2. This confirms the relaxor nature of the system. Similar relaxor nature of the sample has been reported from the inelastic neutron scattering studies.[18]

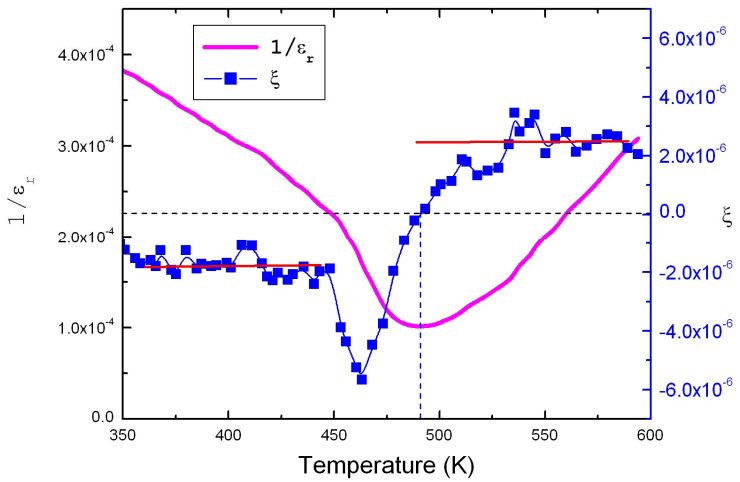

Figure 4.3 Temperature dependence of the inverse of dielectric constant $(1/\varepsilon_r)$ and its derivative (ξ) with respect to temperature for 100 kHz.

In order to get an idea about the order of the phase transition, the reciprocal of permittivity as a function of temperature has been plotted at a selected frequency 100 kHz and is shown in the Fig. 4.3. The effect of interfacial capacitance (which often occurs at low frequencies) of the dielectric material was avoided by selecting a high frequency (i.e., 100 kHz). The plot of $1/\varepsilon_r$ versus T shows different slopes below and above the phase transition temperature. The corresponding derivative $\xi = d/dT(1/\varepsilon_r)$ (Fig. 4.3) has been argued to give information about the order of phase transition and the transition temperature.[51] The temperature at which $\xi = 0$ is known as ferroelectric to paraelectric transition temperature which is found to be T_m = 480 K in the present case. At low temperature T < 450K, ξ (~-1.6×10^{-6}) remains temperature independent representing the ferroelectric state, and at high temperature T > 550K

also ξ (~2.65×10^{-6}) remains independent of temperature, which corresponds to paraelectric state. In the neighborhood of transition (T_m = 480 K), the derivative value drops from 1.34×10^{-6} (505K) to -2.85×10^{-6} (475K). The change in the derivative ratio is found to be 2.12 which is in an agreement with the theory of second order phase transition.[51,52]

4.3.2 Brillouin spectroscopic results

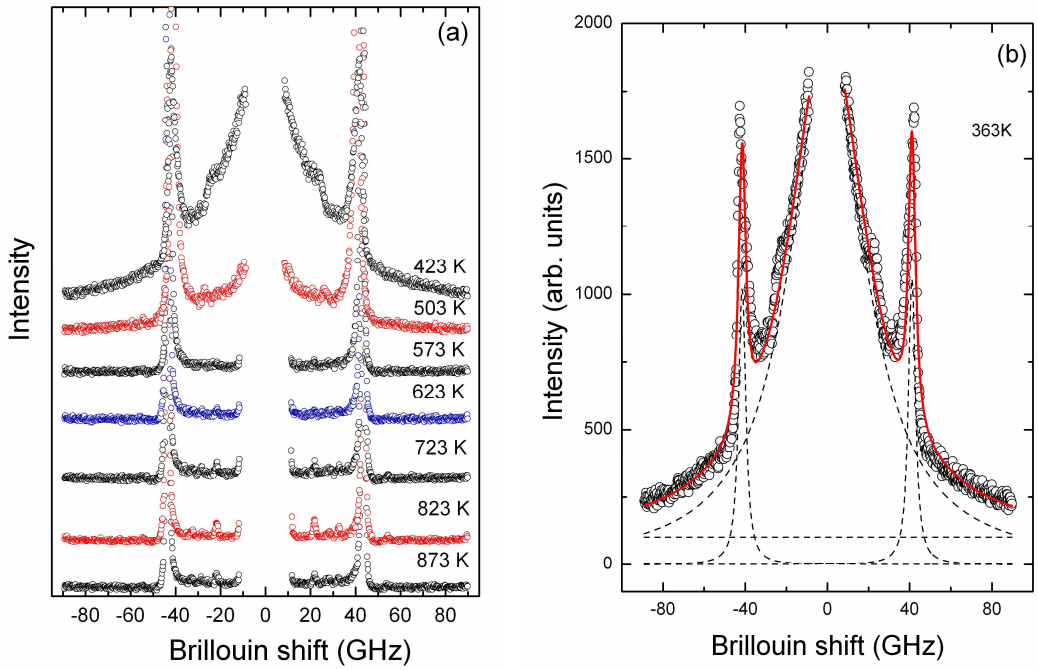

Figure 4.4 (a) Brillouin spectra of PZN-PT measured using a FSR of 100 GHz at selected temperatures and (b) Fitted spectrum along with the data at T = 363 K. Individual fitted peaks are also shown.

Figure 4.4(a) shows the Brillouin spectra using a FSR of 100 GHz at selected temperatures. A Brillouin doublet in the spectra corresponds to the LA mode. In order to precisely determine the Brillouin shift, its full width at half maximum (FWHM) and intensity, we use Voigt functions, where the width of the Gaussian component in the Voigt function is fixed as that of the instrument-function. For the spectrum measured at 363 K, the individual components of the fit are shown in Fig. 4.4(b).

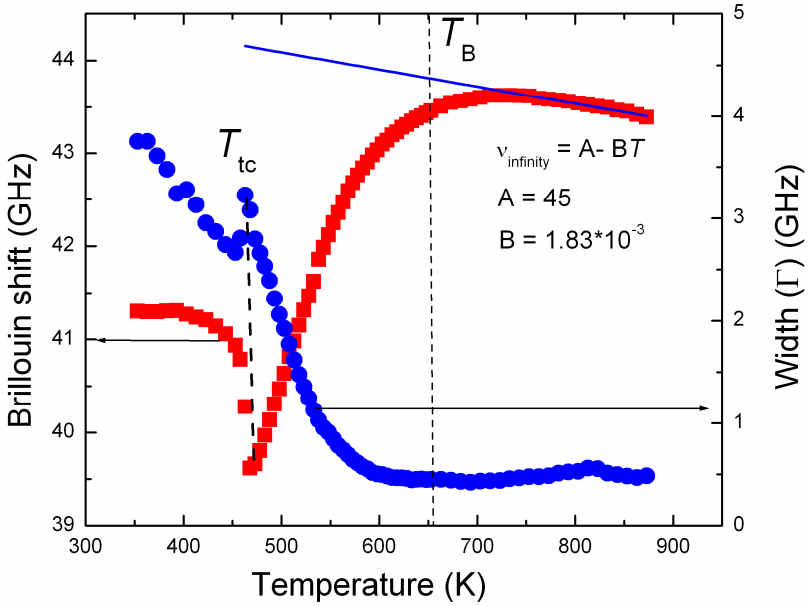

Figure 4.5 Temperature dependences of Brillouin shift and FWHM of the LA phonon mode. Solid line is a linear fit to the Brillouin shift data above 750 K, using $\nu_\infty = A\text{-}BT$, where A and B are constants.

Figure 4.5 shows the LA mode frequency and its FWHM as a function of temperature. One can see that above 650 K, the frequency and FWHM (Γ_{LA}) of LA mode exhibit marginal monotonic changes. At a sufficiently high temperature, relaxor ferroelectrics are in the paraelectric phase without any PNRs. In this temperature range the Brillouin shift is expected to show an almost linear temperature dependence without any pronounced change in the FWHM, indicating that the normal anharmonic process governs the lattice dynamical behavior. However, below 650 K, LA mode frequency shows strong softening till T_{tc} (tetragonal-cubic transition temperature). One can also see that a substantial increase in its FWHM begins around 525 K and reaches a maximum at 463 K. Note that the Brillouin shift and FWHM show sharp anomalies at T_{tc}, representing the occurance of the tetragonal-cubic transition. The behaviour of FWHM near T_{tc} is similar with those reported for higher composition x.[20,21] Earlier X-ray diffraction studies for this composition have suggested the transition temperature to be ~ 490 K.[18] The reason for observing different values of T_{tc} obtained from different techniques will be discussed later.

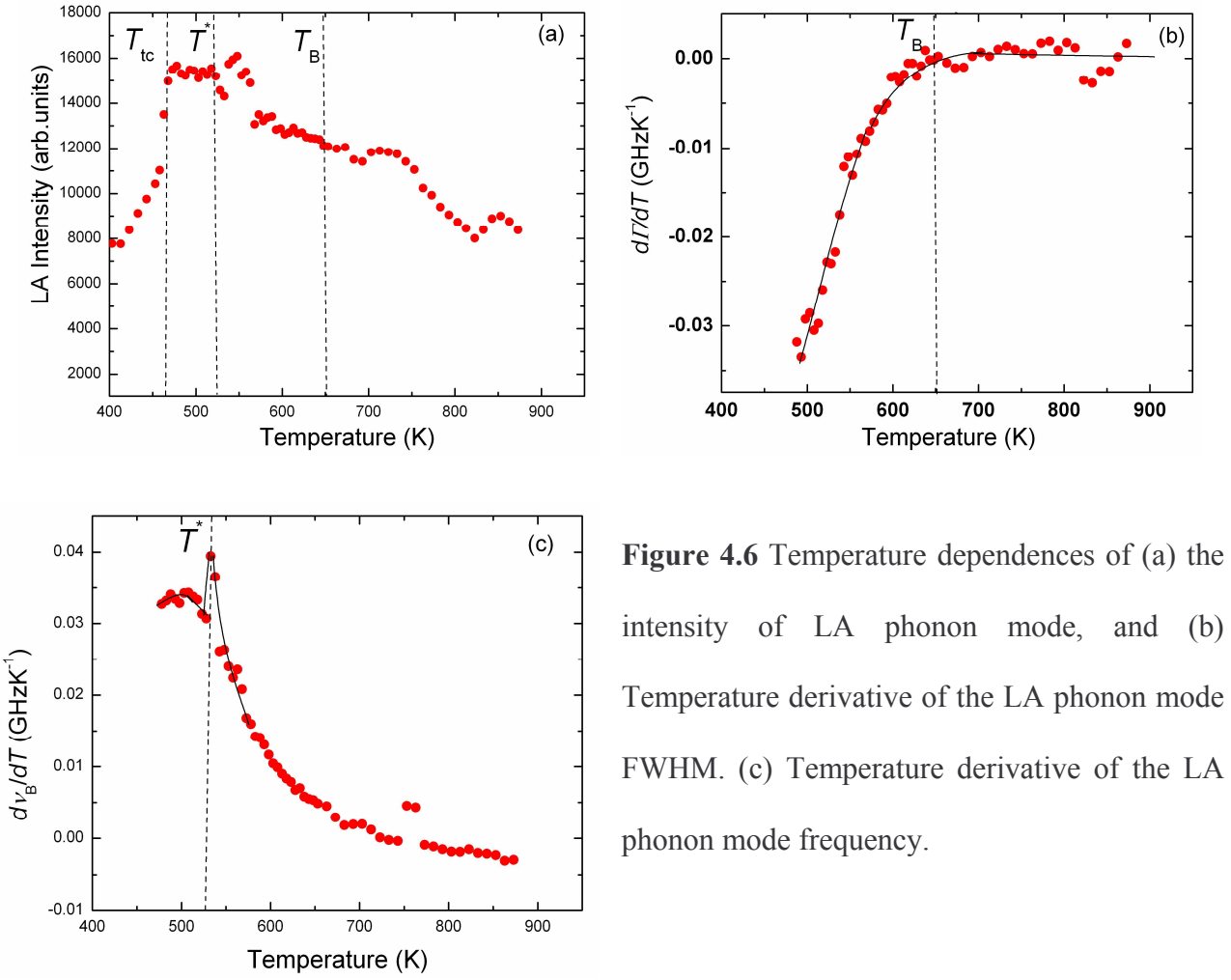

Figure 4.6 Temperature dependences of (a) the intensity of LA phonon mode, and (b) Temperature derivative of the LA phonon mode FWHM. (c) Temperature derivative of the LA phonon mode frequency.

The temperature evolution of the intensity of LA phonon mode, shown in Fig. 4.6(a), exhibits a gradual increase up to 525 K, and a plateau region below 525 K, followed by an anomaly at T_{tc} ~ 463 K. In relaxor ferroelectric materials, the origin of anomalous behavior of acoustic phonon mode has been attributed to PNRs, which begin to form below T_B.[20,32] In the spirit of Landu expression of free energy,[53] the coupling term F_C between the order parameter Q and the strain ε is usually written in terms of increasing powers of these as,

$$F_C(Q,\varepsilon) = \beta_{ij} Q_i \varepsilon_j + \eta_{ijk} Q_i Q_j \varepsilon_k + \delta_{ijk} Q_i \varepsilon_j \varepsilon_k + \ldots\ldots \quad (4.2).$$

The first term corresponds to the bilinear coupling between the order parameter Q and ε. The coupling quadratic in order parameter and linear in the strain (electrostrictive coupling) is

represented by the second term. In the relaxor phase, the PNRs are randomly oriented below T_B and the net macroscopic spontaneous polarization $\langle Q \rangle = 0$, but $\langle Q^2 \rangle \neq 0$. Therefore, one can expect that the only second term would be the dominant factor in the expression of coupling free energy F_C, below T_B. Furthermore, the change in elastic constant owing to the effect of this electrostrictive coupling could be written as[53]

$$\Delta C = \eta^2 \langle Q^2 \rangle \chi^{(\varepsilon)} \qquad (4.3)$$

where η is the electrostrictive coefficient, $\langle Q^2 \rangle$ is the mean value of squared local polarization, and $\chi^{(\varepsilon)}$ is the clamped susceptibility. In the Landau theory of second-order phase transition, the elastic constant $C(T)$ shows a step-like anomaly at the transition temperature because of total cancellation of $\chi^{(\varepsilon)}$ and $\langle Q^2 \rangle$ below the transition temperature. However in case of relaxor, this type of cancellation is not possible since the PNRs nucleate at T_B and local polarization grows gradually with decreasing temperature, which in turn contributes to the decrease of the elastic constant continuously until PNRs saturate. Therefore, the effect of electrostrictive coupling between the order parameter and strain is the reduction of elastic constant and hence a softening of Brillouin shift with decreasing temperature is understandable. The manifestation of electrostrictive coupling in PZN-PT is the gradual softening of the LA phonon frequency upon cooling from T_B to T_{tc}, as found in Fig. 4.5. In the case of relaxors (1-x)PZN-(x)PT with lower x,[20,21] PMN-PT,[54] and prototype relaxor PMN[21] the softening of acoustic mode begins at T_B. In the present investigation the observation of anomalous behaviors of Brillouin shift and FWHM of LA mode clearly suggest the T_B to be ~ 650 K. Further corroborative evidence for T_B has been obtained from the T-derivative of the FWHM[55] of the LA mode. Figures 4.6(b) and 4.6(c) respectively show the T-derivatives of line width Γ of the LA phonon and the LA mode frequency ν_B. One can see that the T-derivative of FWHM of LA mode (Fig. 4.6(b)), exhibits a

change in slope at ~650 K, confirming it to be the T_B. For systems with larger x (7%[20] and 9%[21]), the T_B was found to be above 700 K. The decrease in T_B in the present system could be related to the decrease of degree of relaxer behaviour and enhancement of ferroelectric ordering[21] with increasing PT content. Therefore, the T_B approaches towards T_{tc}. The temperature dependence of FWHM of LA phonon exhibits a λ-type peak at T_{tc} (Fig. 4.5). This is attributed to the Landau-Khalatnikov-like damping mechanism, which is connected with the bilinear coupling between strain and order parameter $(\langle Q \rangle \neq 0)$.[53] Similar mechanism was found in case other relaxor ferroelectric system PZN-PT with x = 9%[21] and also in $Pb(Sc_{0.5}Ta_{0.5})O_3$,[23] which exhibited relaxor to normal ferroelectric transition. The plateau region of intensity plot of LA phonon will be discussed later.

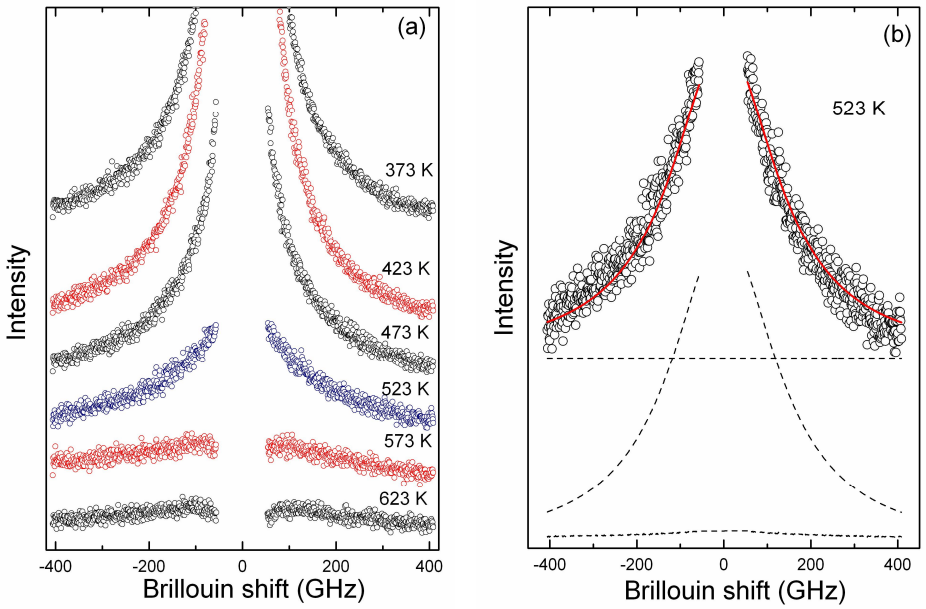

Figure 4.7 (a) Brillouin spectra of PZN-PT measured using a FSR of 400 GHz at selected temperatures. (b) Fitted spectrum along with the data at T = 523 K. Individual fitted peak is also shown.

As mentioned earlier, dynamical relaxations of PNRs give rise to a central peak in the Brillouin spectrum. One can see from Fig. 4.4 that a central peak, which is named as narrow-CP (nCP), is indeed present at lower temperatures; however, its intensity reduces upon heating and nCP finally disappears above 525 K. As the relaxor ferroelectric materials exhibit evidence of multiple time scales of relaxations,[20,32,55,56] it is worth examining if this system also possesses more than one relaxation times. In order to confirm this, Brillouin measurements were also made using a FSR of 400 GHz. Figure 4.7(a) shows the Brillouin spectra obtained using 400 GHz FSR at selected temperatures. A broad central peak (bCP) is found at lower temperatures. Upon heating it becomes weak and finally vanishes above T^*. Thus the behavior of bCP is similar to that of nCP confirming the existence of two relaxation processes. These two type of CPs are related to relaxation processes associated with polarization flipping in PNRs.[20,56] The slower relaxation has been attributed to strain associated with a non-180^o flipping process while the faster relaxation to a 180^o flipping process not involving strain. This is due to the reason that the flipping of polarization with strain can be slower than that without strain.[20,56] Further corroborative evidence for existence of more than one relaxation time was found from the fitting of the entire CP (nCP + bCP), which could not be reproduced with a single Lorenzian function.[20] Therefore, the appearance of both the CPs indicates the existence of relaxation processes involving multiple time scales. Assuming a Debye relaxation process, both nCP and bCP could be fitted using single Lorenzian functions centered at zero frequency. The fit for the bCP spectrum at 523 K is shown in Fig. 4.7(b).

The temperature dependence of integrated intensity and FWHM of both the CPs are shown in Fig. 4.8. One can see that as the temperature is reduced from high temperature, the integrated intensities of both the CPs reach maximum around T_{tc}. The FWHMs of both the CPs show a decreasing trend toward T_{tc} on approaching from paraelectric to relaxor region. The

increase in intensity of CPs and decrease in their line-width with decreasing temperature can be attributed to an increase in PNRs density and enhancement of correlation among them,[21] which in turn is related to a slowing down of the relaxation processes associated with PNRs.

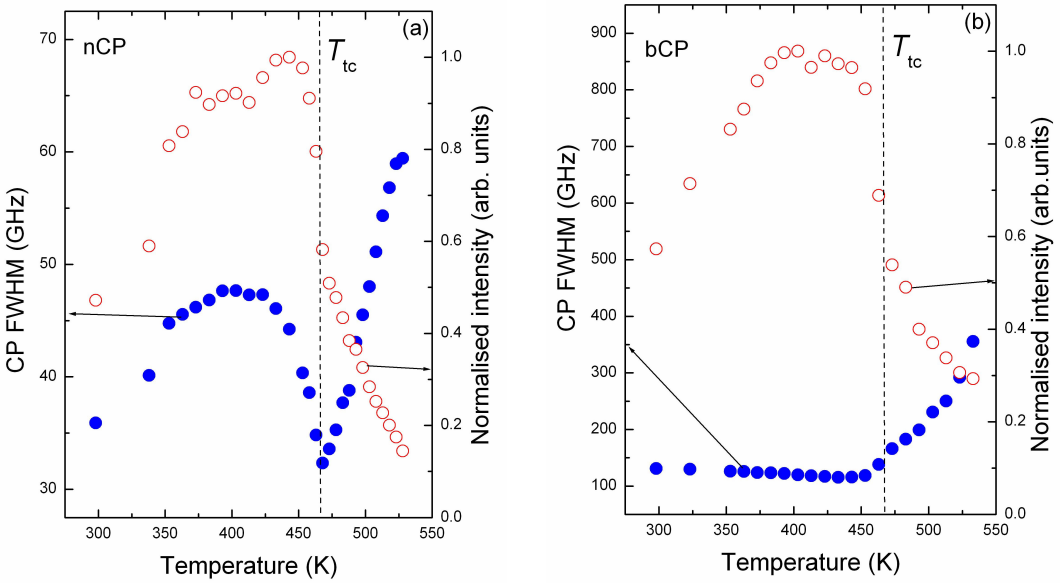

Figure 4.8 Temperature dependences of FWHM and the intensity of (a) narrow-CP and (b) broad-CP.

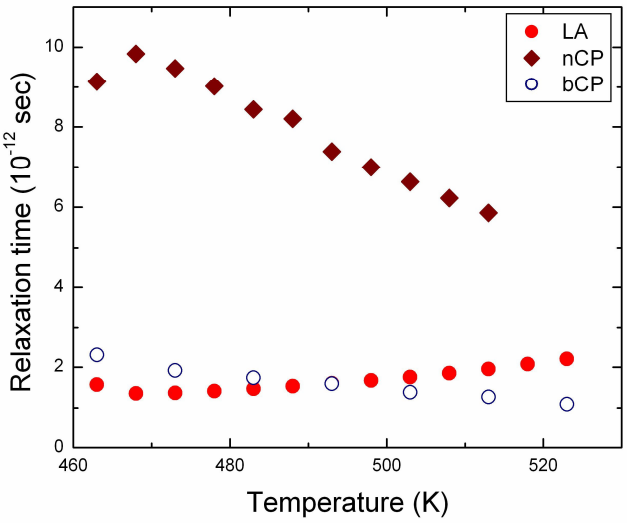

Figure 4.9 Temperature dependences of the relaxation times (τ_{LA}) determined from the LA mode and the relaxation times (τ_{ncp} and τ_{bcp}) determined from the FWHM of narrow and broad-CP.

It has been argued that the softening of LA mode below T_B is a consequence of coupling of polarization fluctuation of PNRs with strain fluctuation.[32] In order to obtain the relaxation

time of the polarization fluctuation τ_{LA} by acoustic phonons, the following equation, assuming a single relaxation process,[20,32] can be used,

$$\tau_{LA}(T) = \Gamma_{tc} / 2\pi(\nu_\infty^2 - \nu_B^2) \quad (4.4)$$

where ν_∞ denotes the Brillouin shift in the high temperature limit, Γ_{tc} is the FWHM at the phase transition temperature. We used a linear temperature dependence of ν_∞ as shown in Fig. 4.5, because of the fact that in the high-temperature range ($T > T_B$), relaxor ferroelectrics are in the paraelectric phase without any PNRs. In this temperature range, ν shows the linear temperature dependence, which is only due to lattice anharmonicity.[32] Below T_{tc} the relaxation time, is expected to be strongly influenced by the structural transition. Therefore, τ_{LA} is calculated for temperatures above 463 K and is shown in Fig. 4.9. In addition, the relaxation times above T_{tc} can also be determined from both the central peaks assuming Debye-relaxation processes, using the following equation,

$$\tau_{CP} = 1/ \pi\Gamma_{CP} \quad (4.5)$$

Figure 4.9 also shows the temperature dependence of relaxation time obtained from Eq. (4.5). One can notice the relaxation time τ_{LA} obtained from LA phonon mode is of nearly same magnitude as that obtained from bCP. This suggests that the relaxation of PNRs is determined by polarization fluctuations coupled with local strain fluctuations via the LA phonon mode. Furthermore, the calculated relaxation time increases gradually while approaching towards T_{tc} (Fig. 4.9), indicating a slowing down of the PNRs dynamics in the relaxor phase ($T_{tc} < T < T_B$). Figure 10 shows the temperature dependence of $1/\tau_{bCP}$, clearly exhibiting a linear behaviour below T_B, in the vicinity of T_{tc}. This implies that the tetragonal-cubic phase transition of PZN-PT is order-disorder type. Such a behaviour is known as critical slowing down of order-disorder transition and the relaxation time is given by the following relation:[57]

$$\frac{1}{\tau} = \frac{1}{\tau_o} + \frac{1}{\tau_1}\left(\frac{T - T_{tc}}{T_{tc}}\right) \qquad (4.6)$$

where, τ_1 is the characteristic time and τ_o is the relaxation attributed to defects.[58] Using Eq. (4.6), the best fit for the relaxation time (Fig. 4.10) yields τ_o=2.3 ps and τ_1=0.28 ps. It is worthy to compare the values of τ_1 obtained for other relaxor systems exhibiting similar order-disorder type behaviour in the vicinity of the transition temperature. In case of $70Pb(Sc_{0.5}Nb_{0.5})O_3$-$30PbTiO_3$,[22] a value of τ_1=0.47 ps has been reported. Similarly τ_1= 2.3 ps is found in $Pb(Sc_{0.5}Ta_{0.5})O_3$ relaxor.[23] From these results, one can conclude that an order-disorder mechanism contributes to the slowing down of the PNRs dynamics in PZN-PT. It may be mentioned that often relaxation processes have associated activation energy. In order to obtain the activation energy for PNRs relaxation dynamics, the *T*-dependence of bCP relaxation time is analyzed using an Arrhenius plot as shown in the inset of Fig. 4.10. The activation energy turns out to be 236 ± 11 meV. The activation energy for the PNR relaxation dynamics in PZN-PT is comparable to that found in other system such as $LiTaO_3$,[59] and PMN-PT[54] exhibiting a similar order-disorder relaxation dynamics.

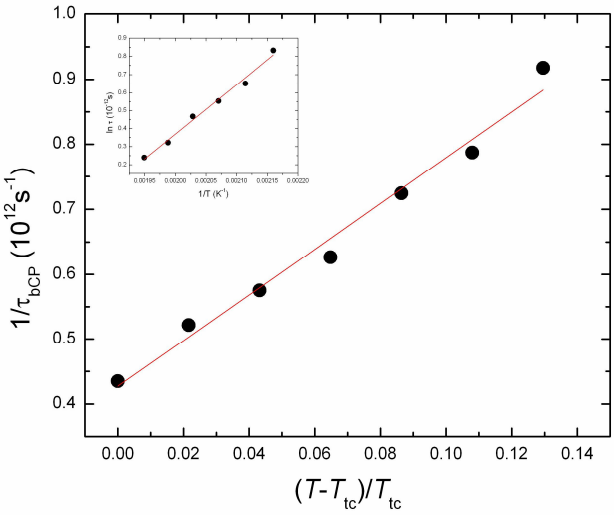

Figure 4.10 Plot of $1/\tau_{bCP}$ as a function of temperature $(T\text{-}T_{tc})/T_{tc}$; The straight line is a fit to Eq. (4.6). The inset shows the logarithmic relaxation time (τ) versus $1/T$. The straight line is a fit to Arrhenius law.

Recent acoustic emission studies on PZN and PZN-PT systems have revealed the existence of a characteristic temperature T^* below Burns temperature T_B.[37,38] From these studies, it has been argued that the coupling of PNRs with local strain fields occurs at T^* but not at T_B. Toulouse *et al*.[13] found the characteristic temperature T_B and T^* of the PZN relaxor system from the analysis of Raman parameters such as optical phonon modes and the CP. The Burns temperature T_B was argued to be associated with the formation of dynamic PNRs related to the short-lived correlation of off-centered ions, whereas below the intermediate temperature T^* long-lived PNRs appear to have formed, which is related to appearance of permanent correlation of the off-centered ions. Recently, It has been suggested that the T^* could be obtained from the extremum of the temperature derivative of Brillouin shift of LA phonon.[32] Figure 4.6(c) shows the temperature derivative of Brillouin shift of LA phonon, exhibiting a maximum at 525 K. This suggests that the strain and polarization electrostrictive coupling of PNRs exhibits an enhancement at T^*. Furthermore, the appearance of plateau region below 525 K in the plot of intensity versus temperature in Fig. 4.6(a) could be due to a signature of T^* at 525 K, where the statics PNRs begin to form. The other corroborative evidence[20] for the existence of T^* comes from the appearance of CPs below the temperature $T^* \sim 525$ K (Fig. 4.9). Dkhil *et al.* found that most of the complex lead-based relaxor ferroelectrics exhibit nearly the same intermediate characteristic temperature $T^* \sim 500 \pm 30$ K.[24] Furthermore, from the Brillouin scattering studies on (1-x)PZN-xPT (x = 4.5 and 9%), T^* was found in the range 500-550 K.[21] In the present studies, T^* turns out to be ~ 525 K.

Figure 4.11 shows the variation of integrated intensities of bCP in the unpolarized (VV+VH) and depolarized (VH) geometries. In both cases, a sharp increase in intensities around T_{tc} is found. Furthermore, the depolarized intensity is weak suggesting a strongly polarized nature of scattering. The tetragonal phase has a unique polarization axis, hence it is likely that the

PNRs in PZN-PT tend to align along that polarization axis while approaching towards tetragonal phase. In fact, this is expected for cubic to tetragonal structural phase transition.[55] Furthermore, the intensity reaches a maximum a little below T_{tc} and then reduces. This suggests that PNRs are still present in the neighbourhood of T_{tc} in the tetragonal phase, establishing a long range polar order.

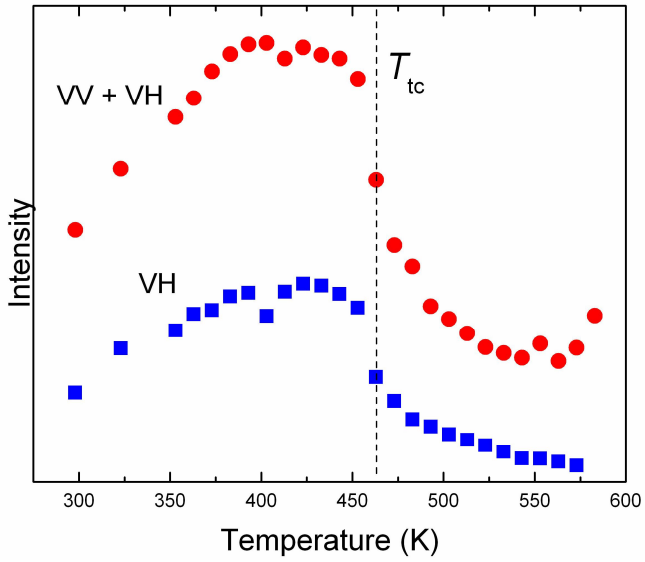

Figure 4.11 Temperature dependences of the integrated intensities of broad central peak measured in unpolarized (VV+VH) and depolarized (VH) geometries.

4.3.3 Raman spectroscopic results

The ambient tetragonal ferroelectric phase of PZN-PT belongs to the space group *P4mm*. The irreducible representation of optical phonons in this phase is: $\Gamma_{opt} = 3A_1 + 4E + B_1$, where the A_1 and E modes are both Raman and Infrared active (IR), whereas the B_1 mode is only Raman active. The Raman tensors associated with these modes are:

$$A_1(Z): \begin{bmatrix} a & 0 & 0 \\ 0 & a & 0 \\ 0 & 0 & b \end{bmatrix}; \quad E(X): \begin{bmatrix} 0 & 0 & e \\ 0 & 0 & 0 \\ e & 0 & 0 \end{bmatrix}; E(Y): \begin{bmatrix} 0 & 0 & 0 \\ 0 & 0 & e \\ 0 & e & 0 \end{bmatrix}; B_1: \begin{bmatrix} c & 0 & 0 \\ 0 & -c & 0 \\ 0 & 0 & 0 \end{bmatrix},$$

where X, Y and Z indicate the polarization direction of the IR active modes. The Raman mode for [100] oriented single crystal in X(YY)X' scattering geometry are $A_1(TO)+B_1$ and E(TO) in $X(YZ)X^{'}$ configuration. Figure 12(a) shows the unpolarized Raman spectra measured at different

temperature. At room temperature a total of five prominent Raman peaks and three shoulders are discernible in the frequency range 90-1000 cm^{-1}. By analyzing the spectra using PeakFit, eleven modes could be identified in the same range of frequency.

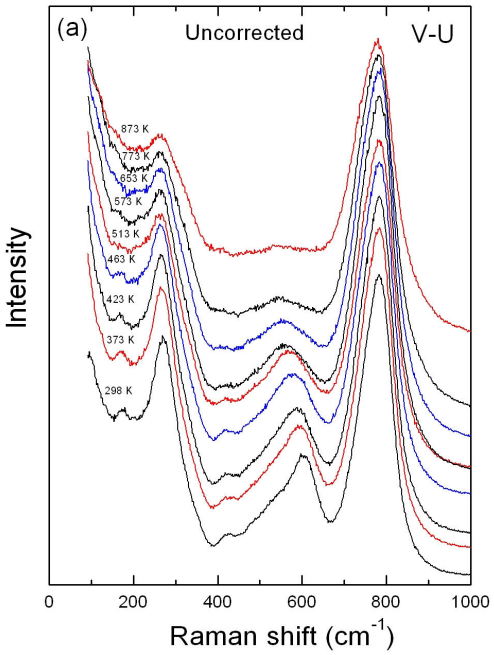

Figure 4.12 Raman scattering spectra measured at various temperatures in (a) unpolarized and in (b) VV and (c) VH polarized geometries upon heating from 298 to 873 K.

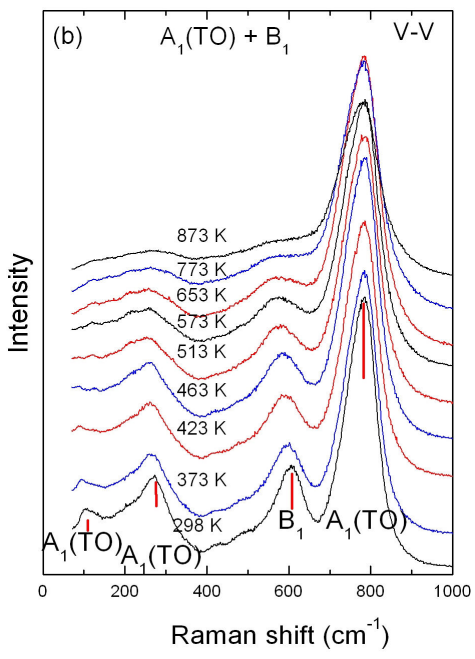

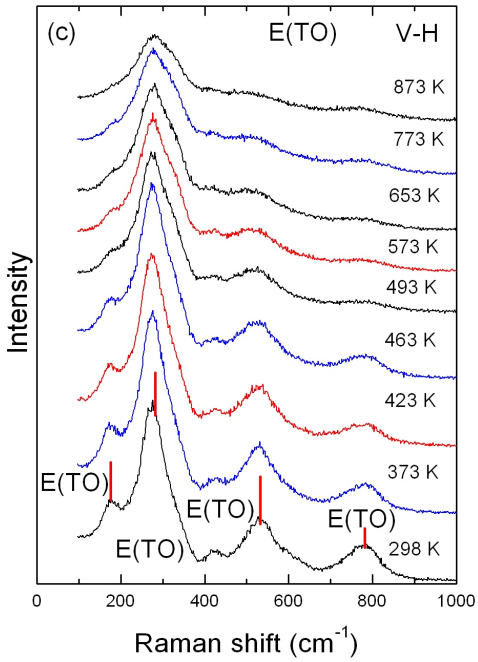

Figures 4.12 (b) and (c) show the polarized Raman spectra in VV and VH geometries at different temperatures. In these figures we have presented the reduced Raman intensity I_R after correcting

for the effect of temperature on the intensities so that the intensity changes can be compared independent of thermal population factor, which is given by $I_R = I(\omega)/(e^{\hbar\omega/k_BT} - 1)$, where $I(\omega)$ corresponds to the measured Raman intensity and $1/(e^{\hbar\omega/k_BT} - 1)$ is the Bose-Einstein phonon population factor. The Raman spectra were found to be broad at ambient temperature. The broad nature of the Raman modes has been recently argued to arise due to substitutional disorder at cation sites.[39] At elevated temperature the spectra broaden further and the intensities are found to reduce as expected. In order to study the changes caused by the influence of temperature, a quantitative analysis of the changes in the Raman spectra is required. This can be achieved only when the peak positions, line-widths and intensities of the modes are precisely obtained using curve fitting. Hence the reduced spectra were fitted to multi-Lorenzians using the PeakFit program. In the context of number of peaks used for fitting the spectrum for a given temperature, it is important to point out that although it is always possible to fit more number of peaks to a given spectrum, we adopted a strategy to use the minimum number of peaks that yield a good fit. If one uses more number of modes than required, it leads to large standard errors and strong correlations in fitted parameters.[41] The fitted parameters obtained from unpolarized Raman spectra was used to ascertain the positions and widths of the weak and poorly resolved peaks of the VV and VH spectra.[60] The fitted Raman peaks in VV geometry at 298 and 713 K as a representative example are shown in Fig. 4.13. At 298 K, ten modes could be identified at 105, 204, 273, 419, 504, 604, 728, 760, 788 and 809 cm^{-1}, respectively. On the other hand at 713 K, modes at 105, 204, 419, 504, 728, and 809 cm^{-1} could not be identified and hence only four modes survived at high temperature.

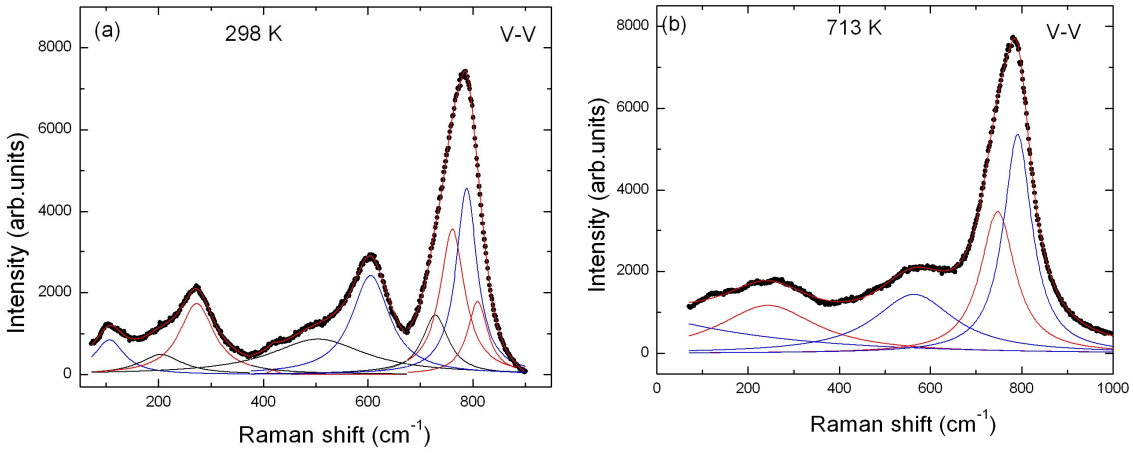

Figure 4.13 Examples of multiple peak decomposition of Raman spectra in VV geometry measured at (a) 298 K and (b) 713 K.

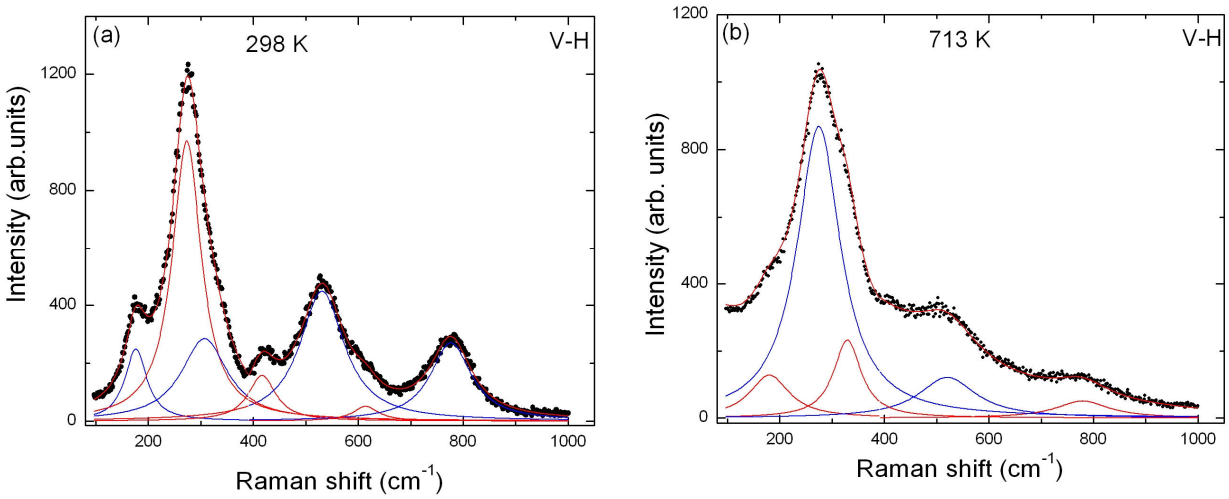

Figure 4.14 Examples of multiple peak decomposition of Raman spectra in VH geometry measured at (a) 298 K and (b) 713 K.

Similarly, Fig. 4.14 shows the fitted Raman peaks at 298 K and 713 K in VH geometry. At 298 K, seven modes at 176, 273, 307, 416, 530, 614 and 776 cm^{-1} are found whereas at 713 K, the modes at 416 and 614 cm^{-1} could not be identified. Less number of modes at high temperature in both the geometries could be due to either insufficient intensity of weak modes or transformation to the higher symmetry cubic phase. The modes in higher temperature phase will

be discussed separately. The observed Raman modes and their assignments in both the geometry are listed in table 4.1. The unassigned weak modes are possibly due to polarization leakage.

Table 4.1 Raman mode frequencies (cm^{-1}) in PZN-PT single crystal (x = 0.15) in different polarization configurations. Numbers in the parenthesis are the standard errors in least significant digits.

X(YY)X' $A_1(TO)+B_1$	X(YZ)X' E(TO)
105.9(9) A(TO)	-
-	176.2(7) E(TO)
204(2)	-
272.7(4) A(TO)	273(1) E(TO)
-	307(21)
419(2)	416.4(8)
504(4)	-
-	530.8(4) E(TO)
604.7(5) B_1	614(2)
728(4)	-
760(2)	-
788(1) A(TO)	776.4(4) E(TO)
809(4)	-

Figure 4.15 shows the dependences of mode frequencies on temperature in both polarized and depolarized geometries. One can see that in VV geometry, modes at 419 and 504 cm^{-1} could

not be followed at high temperatures. Note the disappearance of the modes at 105 and 204 cm^{-1} (Fig. 4.15(a)) at ~473 K. Similarly, the mode at 416 cm^{-1} in VH geometry (Fig. 4.15(b)) is also found to vanish at ~473 K. In addition, the modes at 273 and 760 cm^{-1} in VV (Fig. 4.15(a)) and those at 176 and 776 cm^{-1} in VH (Fig. 4.15(b)) show a discontinuous change at ~473 K. It can be mentioned here that the mode disappearance, mode broadening, and discontinuous change in mode frequencies are typical for Perovskite ferroelectrics undergoing a phase transition.[40,61] Therefore, the present observations suggest that the system undergoes a tetragonal to cubic phase transition at T_{tc} ~473 K, which is close to the transition temperature reported from XRD measurement[18] as well as the dielectric results discussed earlier.

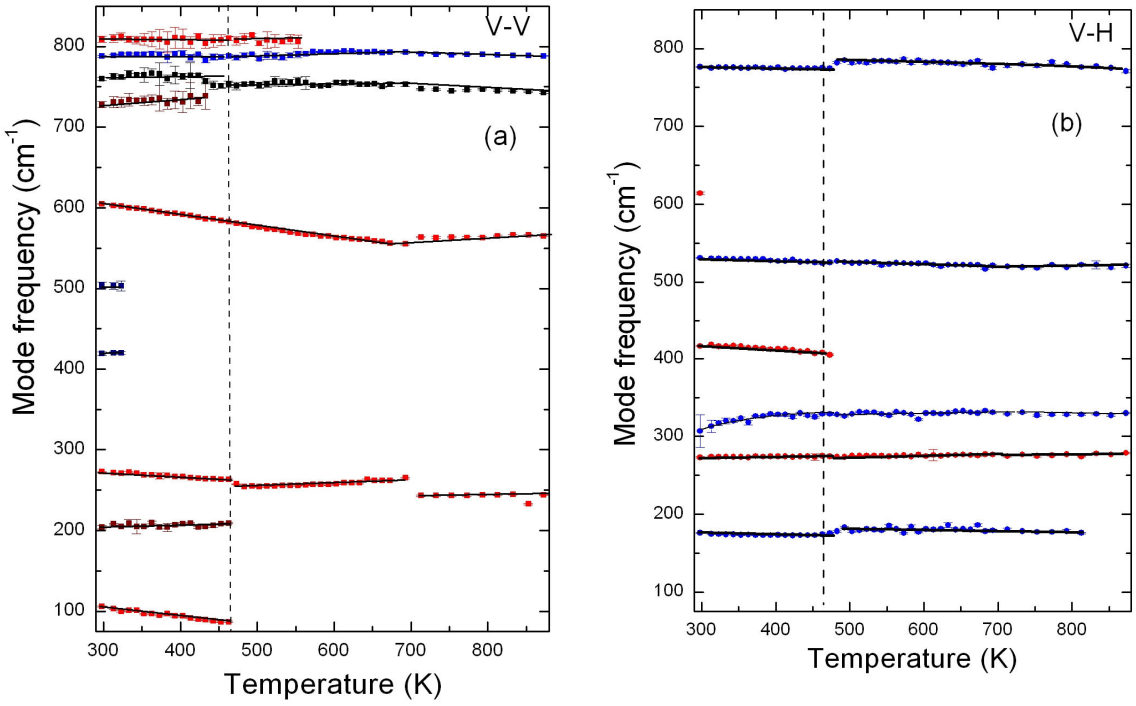

Figure 4.15 Dependence of Raman mode frequencies on temperature in (a) VV and (b) VH geometries. Vertical dashed lines correspond to tetragonal-cubic transition temperature.

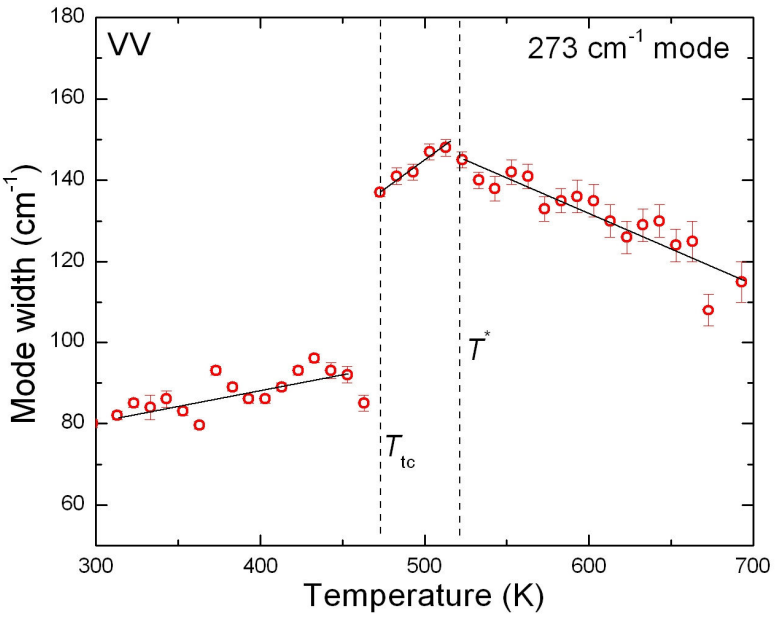

Figure 4.16 Temperature dependence of FWHM of 273 cm^{-1} mode in VV geometry. Lines through the data are guides to the eye.

As discussed in the introduction Pb-based relaxors have shown evidence of chemically ordered nano-regions of double-Perovskite structure ($Fm\bar{3}m$) dispersed in a disordered matrix with an average single-Perovskite structure ($Pm\bar{3}m$). It has been further argued that the PZN and PMN, when added with moderate amount of PT, do not disturb the cubic ordered structure ($Fm\bar{3}m$).[11,12] A strong mode at ~788 cm^{-1} in the Raman spectra (see Fig. 4.12) is the characteristic of Pb-based relaxors.[13,62-64] Therefore one should expect the Raman scattering in 0.85PZN-0.15PT should have contributions from both these ordered and disordered regions. From group theoretical analysis, the total irreducible representation of optical phonons in the cubic $Pm\bar{3}m$ phase is[12,39] $\Gamma_{opt} = 3F_{1u}+F_{2u}$, where F_{1u} is infrared active, and F_{2u} is inactive both in Raman and infrared. Thus none of these modes are Raman active. On the other hand, the optical phonons in $Fm\bar{3}m$ phase are $\Gamma_{opt} = A_{1g}+E_g+2F_{2g}+F_{1g}+4F_{1u}+F_{2u}$.[13,65] In this phase four Raman active non-polar phonons $A_{1g}+E_g+2F_{2g}$ are expected. According to the selection rules, A_{1g} and E_g modes are active in X(YY)X' geometry and the two F_{2g} modes are active in X(YZ)X' geometry.

More number of peaks than allowed by symmetry (Figs. 4.15(a, b)) above T_{tc} could be due to presence of ferroic atomic arrangements whose life time is longer than the time scale probed by Raman spectroscopy.[12]

In previous studies on Pb-based relaxors it has been reported that the Raman modes at 50 and 273 cm^{-1} are very sensitive to structural transition.[12,64] Therefore it is instructive to analyse the temperature dependence of these Raman modes. Since the mode related to Pb[12] at ~50 cm^{-1} is not covered in our spectral range, we restricted our analysis to the 273 cm^{-1} mode. This mode is the *B*-cation-localized F_{1u} mode of the prototype $Fm\bar{3}m$ structure and is infrared active, whose appearance as a Raman mode results from the off-center displacement of *B*-cations from their ideal cubic positions.[12,62,64] Figure 4.16 shows the behaviour of FWHM of this mode with temperature. A change of slope at the intermediate temperature T^*~525 and a dramatic discontinuous change at T_{tc} is unambigiously evident. The transition temperature suggested from the anomalies in Fig. 4.16 is in good agreement with that obtained from the temperature dependence of the mode frequencies (see Fig. 4.15). It can be stressed here that this mode shows decrease in its width at T^* in several types of Pb-based relaxors.[12,62,64] Therefore, T^* represents an universal character of the PNRs dynamics, where the strong correlation between the off-centered displacement of *B*-site cations begins, leading to permanent PNRs.[12] A remark on observing different phase transition temperatures from different techniques is in order. The difference in the length scale of sensitivity of XRD (~100 Å), dielectric (size of sample) and light scattering (~30-40 Å) could be the reason for different transition temperatures in different technique. It can be stressed here that the length scale of sensitivity depends on the nature of the interaction of the probed radiation and the sample.

4.3.4 Summary and conclusions

The temperature dependences of LA phonon and CP in relaxor ferroelectric PZN-PT single crystal have been investigated using Brillouin scattering in the temperature range 300-873 K. Below the Burns temperature T_B, softening of mode frequency, followed by an increase in its FWHM is found. At the tetragonal-cubic phase transition temperature ~463 K, both LA mode frequency and FWHM exhibit clear anomalies. Slowing down of relaxation time of PNRs is noticed from the narrowing of CPs while approaching the transition from high temperature side. An intermediate characteristic temperature T^*~525 K is identified below T_B. The electrostrictive coupling between the strain and polarization fluctuation begins to take place below temperature T_B. The relaxation time of CP exhibits critical slowing down upon approaching the tetragonal-cubic transition suggesting the order-disorder nature of phase transition. A comparision of unpolarized and depolarized scattering in cubic phase indicates polarized nature of the broad central peak. This implies that the PNRs tend to align to establish a long range polar ordering. Polarized Raman spectroscopic studies were carried out on 0.85PZN-0.15PT single crystal in the temperature range 298 to 873 K to study the structural transition from tetragonal-cubic phase. Anomalies in the temperature dependence of mode frequencies and line-width of 273 cm^{-1} mode were found at T_{tc} and T^*. The transition temperature is found to be T_{tc} ~473 K consistent with that obtained from Brillouin scattering.

References

1. D. Viehland, J. F. Li, S. J. Jang, L. E. Cross, and M. Wuttig, Phys. Rev. B **46**, 8013 (1992).
2. S. -E. Park and T. R. Shrout, J. Appl. Phys. **82**, 1804 (1997).
3. D. E. Cox, B. Noheda, G. Shirane, Y. Useu, K. Fujishiro, and Y. Yamada, Appl. Phys. Lett. **79**, 400 (2001).
4. D. Viehland, S. J. Jang, L. E. Cross, and M. Wuttig, J. Appl. Phys. **68**, 2916 (1990).
5. R. Pirc and R. Blinc, Phys. Rev. B **60**, 13470 (1990).
6. S. Tinte, B. P. Burton, E. Cockayne, and U. V. Waghmare, Phys. Rev. Lett. **97**, 137601 (2006).
7. S. Vakhrushev, S. Zhukov, G. Fetisov, and V. Chernyshov, J. Phys.: Condens. Matter **6**, 4021 (1994).
8. I. W. Chen, P. Li, and Y. Wang, J. Phys. Chem. Solids **57**, 1525 (1996).
9. I. W. Chen, J. Phys. Chem. Solids **61**, 197 (2000).
10. P. K. Davies and M. A. Akbas, J. Phys. Chem. Solids **61**, 159 (2000).
11. O. Svitelskiy, D. La-Orauttapong, J. Toulouse, W. Chen, and Z.-G. Ye, Phys. Rev. B **72**, 172106 (2005).
12. N. Waeselmann, B. Mihailova, B. J. Maier, C. Paulmann, M. Gospodinov, V. Marinova, and U. Bismayer, Phys. Rev. B **83**, 214104 (2011).
13. J. Toulouse, F. Jiang, O. Svitelskiy, W. Chen, and Z.-G. Ye, Phys. Rev. B **72**, 184106 (2005).
14. B. Maier, B. Mihailova, C. Paulmann, J. Ihringer, M. Gospodinov, R. Stosch, B. Güttler, and U. Bismayer, Phys. Rev. B **79**, 224108 (2009).

15. W. S. Chang, L. C. Lim, F.-T. Wang, C.-M. Hsieh, and C.-S. Tu, J. Phys. Condens. Matter **20**, 395229 (2008).

16. D. La-Orauttapong, J. Toulouse, J. L. Robertson, and Z. G. Ye, Phys. Rev. B **64**, 212101 (2001).

17. I. K. Jeong and J. K. Lee, App. Phys. Lett. **88**, 262905 (2006).

18. D. La-Orauttapong, B. Noheda, Z.-G. Ye, P. M. Gehring, J. Toulouse, D. E. Cox, and G. Shirane, Phys. Rev. B **65**, 144101 (2002).

19. Y. Gorouya, Y. Tsujimi, M. Iwata, and T. Yagi, Appl. Phys. Lett. **83**, 1358 (2003).

20. S. Tsukada and S. Kojima, Phys. Rev. B **78**, 144106 (2008).

21. Jae-Hyeon Ko, Do Han Kim, and S. Kojima, Phys. Rev. B **77**, 104110 (2008).

22. S. Kojima, S. Tsukada, Y. Hidaka, A. A. Bokov, and Z.-G. Ye, J. Appl. Phys. **109**, 084114 (2011).

23. V. Sivasubramanian and S. Kojima, Phys. Rev. B **85**, 054104 (2012).

24. B. Dkhil, P. Gemeiner, A. Al-Barakaty, L. Bellaiche, E. Dul'kin, E. Mojaev, and M. Roth, Phys. Rev. B **80**, 064103 (2009).

25. Burns and F. H. Dacol, Solid State Commun. **48**, 853 (1983).

26. D. Viehland, J. F. Li, S. J. Jang, L. E. Cross, and M. Wuttig, Phys. Rev. B **46**, 8013 (1992).

27. L. E. Cross, Ferroelectrics **76**, 241 (1987).

28. Y. Moriya, H. Kawaji, T. Tojo, and T. Atake, Phys. Rev. Lett. **90**, 205901 (2003).

29. G. Shabbir and S. Kojima, Appl. Phys. Lett. **91**, 062911 (2007).

30. J.-H. Ko, D. H. Kim, and S. Kojima, Appl. Phys. Lett. **90**, 112904 (2007).

31. J.-H. Ko, D. H. Kim, S. Kojima, W Chen, and Z.-G. Ye, J. Appl. Phys.**100**, 066106 (2006).

32. S. Tsukada, Y. Ike, J. Kano, T. Sekiya, Y. Shimojo, R. Wang, and S. Kojima, J. Phys. Soc. Jpn. **77**, 033707 (2008).

33. S. G. Lushnikov, J.-H. Ko, and S. Kojima, Appl. Phys. Lett. **84**, 4798 (2004).

34. J.-H. Ko, S. Kojima, A. A. Bokov, and Z.-G. Ye, Appl. Phys. Lett. **91**, 252909 (2007).

35. Do Han Kim, Jae-Hyeon Ko, C. D. Feng, and S. Kojima, Appl. Phys. Lett. **87**, 072908 (2005).

36. Yohei Nakata, Yuhji Tsujimi, Kohei Katsuraya, Makoto Iwata, and Toshirou Yagi, Appl. Phys. Lett. **89**, 022903 (2006).

37. E. Dul'kin, M. Roth, P.-E. Janolin, and B. Dkhil, Phys. Rev. B **73**, 012102 (2006).

38. M. Roth, E. Mojaev, E. Dul'kin, P. Gemeiner, and B. Dkhil, Phys. Rev. Lett. **98**, 265701 (2007).

39. K. K. Mishra, V. Sivasubramanian, R. M. Sarguna, T. R. Ravindran, and A. K. Arora, J. Solid State Chem. **184**, 2381 (2011)

40. K. K. Mishra, V. Sivasubramanian, and A. K. Arora, J. Raman Spectrosc. **42**, 517 (2011)

41. K. K. Mishra, A. T. Satya, A. Bharathi, V. Sivasubramanian, V. R. K. Murthy, and A. K. Arora, J. Appl. Phys. **110**, 123529 (2011).

42. N. K. Karan, R. S. Katiyar, T. Maiti, R. Guo, and A.S. Bhalla, J. Raman Spectrosc.**40**, 370 (2009).

43. P.S. Dobal, A. Dixit, and R. S. Katiyar, J. Appl. Phys. **89**, 8085 (2001).

44. M. Shen, G. G. Siu, Z. K. Xu, and W. Cao, Appl. Phys. Lett. **86**, 252903 (2005).

45. J. Y. Sun, Y. L. Yang, K. Zhu, Y. Liu, G. G. Siu, and Z. K. Xu, Chin. Phys. Lett. **25**, 290 (2008).

46. Y. Liu, Y. Jiang, J. Liu, Y. Mo, S. Xie, Z. Zhang, and S. Quan, Phys. Rev. B **49**, 5058 (1994).

47. J. Cheng, Y. Yand, Y. H. Tong, S. B. Lu, J. Y. Sun, K. Zhu, Y. L. Liu, G. G. Siu, and Z. K. Xu, J. Appl. Phys. **105**, 053519 (2009).

48. M. Iwata, Y. Hasegawa, R. Aoyagi, M. Maeda, N. Wakiya, H. Suzuki, and Y. Ishibashi, Ferroelectrics **378**, 84 (2009).

49. M. EI Marssi and H. Dammak, Solid State Commun. **124**, 487 (2007).

50. B. K. Barick, K. K. Mishra, A. K. Arora, R. N. P. Choudhary, and D. K. Pradhan, J. Appl. Phys. D, **44**, 355402 (2011).

51. M. Tyunina, M. Plekh, M. Antonova, and A Klavane, Phys. Rev. B **84**, 224105 (2011).

52. K Dutta, P.A Thomas, and K Roleder, Phys. Rev. B **82**, 224105 (2010).

53. W. Rehwald, Adv. Phys. **22**, 721 (1973).

54. F. M. Jiang and S. Kojima, Phys. Rev. B **62**, 08572 (2000).

55. V. Sivasubramanian, S. Tsukada, and S. Kojima, Jpn. J. Appl. Phys. **47**, 7740 (2008).

56. S. Tsukada, Y. Ike, J. Kano, T. Sekiya, Y. Shimojo, R. Wang,, and S. Kojima, Appl. Phys. Lett. **89**, 212903 (2006).

57. M. E. Lines and A. M. Glass, *Principles and Applications of Ferroelectrics and Related Materials*, (Clarendon, Oxford, 1977), p. 50.

58. R. Ohta, J. Zushi, T. Ariizumi, and S. Kojima, J. Appl. Phys. **98**, 092909 (2011).

59. A. Hushur, S. Gvasaliya, B. Roessli, S. Lushnikov, and S. Kojima, Phys. Rev. B **76**, 064104 (2007).

60. O. Svitelskiy, J. Toulouse, and G. Yong, Phys. Rev. B **68**, 104107 (2003).

61. Juan Cheng, Yang Yang, Yan-Hua Tong, Sheng-Bo Lu, Jing-Ya Sun, Ke Zhu, Yu-Long Liu, G. G. Siu, and Z. K. Xu, J. Appl. Phys. **105**, 053519 (2009).

62. B. Mihailova, U. Bismayer, B. G¨uttler, M. Gospodinov, and L. Konstantinov, J. Phys. Condens. Matter **14**, 1091 (2002).

63. H. Taniguchi, M. Itho, and D. Fu, J. Raman Spectrosc., **42**, 706 (2011).

64. A.-M. Welsch, B. J. Maier, B. Mihailova, R. J. Angel, J. Zhao, C. Paulmann, J. M. Engel, M. Gospodinov, V. Marinova, and U. Bismayer, Z. Kristallogr. **226**, 126 (2011).

65. M. I. Aroyo, A. Kirov, C. Capillas, J. M. Perez-Mato, and H. Wondratschek, Acta Crystallogr. Sect. A **62**, 115 (2006).

Chapter 5

Vibrational, structural, and magnetic properties of multiferroic BLFPT$_x$

5.1 Introduction

Multifunctional materials that couple electric, magnetic and structural order parameters resulting in coexistence of ferroelectric, ferromagnetic, and ferroelastic behaviors have attracted considerable attention among the scientific community in recent years. Rhombohedral $BiFeO_3$ (BF) is unique among other multiferroic materials due to the coexistence of two types of long-range order: antiferromagnetic order below the Neel temperature T_N = 643 K and the ferroelectric order below Curie temperature T_C = 1100 K.[1, 2] However, the compound was not found to show the magnetoelectric effect, as an spiral modulated spin structure led to disappearance of overall magnetization.[3] In addition, the electric polarization was also found to be quite low.[4, 5] Furthermore, the synthesis of ideal Perovskite phase of pure BF is difficult because of comparable thermodynamic stability of Fe^{3+} and Fe^{2+} states of iron in this compound.[6, 7] In order to overcome these limitations, several solid-solutions have been synthesized and their properties investigated. The solid-solutions of BF with other ABO_3 compounds such as $PbTiO_3$ (PT), $PrFeO_3$ and $BaTiO_3$ stabilize the perovskite phase and exhibit spontaneous magnetization.[8-10] Recently, Zhu *et al* have carried out structural and magnetic studies on (1-y)($BiFeO_3$)–y($PbTiO_3$) solid solutions as a function of composition.[11] It was pointed out that the mixed crystals with $BiFeO_3$-$PbTiO_3$ (BF-PT) ratio around 50:50 favor the formation of chemically ordered micro-regions in which spiral spin modulation decreases. Singh *et al*.[12] reported improved dielectric and magneto-electric properties for the system 0.50($Bi_{1-x}La_xFeO_3$)-0.50($PbTiO_3$) (BLFPT$_x$) for x = 0.5 compositions. However, the phonon spectra of this system were not investigated. In addition, the dependence of phonon, magnetic and dielectric behaviors on La-substitution have not been reported so far. Cheng *et al*.[13] studied the effect of

La-doping on magnetic and electrical behavior of $0.45(Bi_{1-x}La_xFeO_3)$-$0.55(PbTiO_3)$ only in a limited range of $0.1 \leq x \leq 0.3$ and found significantly enhanced polarization and magnetization as compared to pure $BiFeO_3$. The phonon spectra of pure and La-substituted BF-PT have not been investigated as a function of temperature and across the tetragonal-cubic transition. Raman spectroscopy is a powerful technique for studying short-range order[14-17] and phase transitions in perovskites.[14, 18-20] The phonon dynamics can provide useful insight into microscopic properties such as mode softening, structure property relations, nature of local ordering, and structure in the nano-scale range.[21, 22]

The $BLFPT_x$ solid solution belongs to the family of Perovskite structure with the general formula ABO_3 (Inset Fig. 1.6). The sublattice *A* is occupied by randomly distributed nonmagnetic Bi^{3+} ($6p^0$, S=0), Pb^{2+} ($6p^0$, S=0) and La^{3+} ($5d^0$, S=0) ions, while the *B* site is occupied by randomly distributed the magnetic Fe^{+3} ($3d^5$, S=5/2) and non-magnetic Ti^{4+} ($3d^0$, S=0) ion. Incorporating La^{3+} and Pb^{2+} cations at Bi^{3+} site and Ti^{4+} on Fe^{3+} site can cause a canted spin arrangement of unpair electrons on Fe^{3+} ions.[23] The La^{3+} doping in BF is also argued to destrory spiral modulated spin structure and favoring a collinear antiferromagnetic spin configuration.[24] In addition, BF-PT possesses a strong chemical inhomogeneity due to the occupation of the *A* and *B* site by heterovalent cations. This leads to a frustration between charge neutrality and lattice strain, which on the local scale can result in the formation of ordered nanoregion.[25, 26] There are a few reports on investigation on magnetic and polarization behaviors of La-modified $BiFeO_3$-$PbTiO_3$ with different ratio of BF and PT. However, there is no systematic study on the effect of La on the evolution of magnetic and polarization behaviors of $BLFPT_x$ in the full range of *x*. In the chapter the results of a detailed study of $BLFPT_x$ using several techniques are presented. At First, we discuss synthesis and investigations of structural and vibrational properties of pure and La-substituted $(Bi_{1-x}La_x)_{0.5}Pb_{0.5}Fe_{0.5}Ti_{0.5}O_3$ compounds at ambient using

X-ray diffraction and Raman spectroscopy. The emphasis is to understand the nature of the phonons in this mixed-crystal system and to probe the crystallographic phase transition. Secondly, recent reports of improved dielectric and magneto-electric properties in this system for certain compositions[27] provide compelling reason for more detailed investigations of the structural stability as a function of x and T. Although a tetragonal phase has been found[13] at ambient in 45:55 BLFPT$_x$ up to x = 0.3, synthesis of 50:50 BF-PT system doped with La up to x = 0.3 has not been reported. Furthermore, the structural stability of these technologically important solid-solutions has not been investigated so far at elevated temperature. Therefore, a first x-T phase diagram of $0.50(Bi_{1-x}La_xFeO_3)$-$0.50(PbTiO_3)$ solid-solution was also investigated using *in-situ* X-ray diffraction at high temperature and the results are discussed. Finally, the phonons, magnetic and ferroelectric ordering in La-substituted BLFPT$_x$ are investigated for x = 0.0, 0.2, 0.3, 0.4 and 0.5 samples as a function of temperature using Raman, magnetization and polarization measurements. The Raman spectra are analyzed quantitatively to obtain mode frequencies, their line widths and intensities. Magnetization measurements are made from ambient down to 4 K in field-cooled and zero-field cooled conditions. The field dependence of magnetization is also studied to examine the possibility of a spin-glass like magnetic ordering. From the ferroelectric hysteresis loop, the composition dependence of remnant polarization is also obtained. The observed results are discussed in the context of anisotropy and tetragonal-cubic structural transition.

5.2 Experimental details

Polycrystalline $(Bi_{1-x}La_x)_{0.5}Pb_{0.5}Fe_{0.5}Ti_{0.5}O_3$ powder samples were synthesized for x = 0.0, 0.2, 0.3, 0.4 and 0.5 by the solid-state reaction technique. The high purity precursors (Bi_2O_3, La_2O_3, PbO, Fe_2O_3, and TiO_2) of 99.9% purity (Alfa Aesar) weighed in stoichiometric proportion were mixed using an agate mortar for 2 h and then in wet (acetone) medium to get a homogeneous

mixture for 4 h. The mixture so obtained were then calcined in a closed platinum crucible for 3 hours at 773 K in air, reground and calcined again for 4 hours at 1073 K. The calcined powders were pressed into pellets and sintered at 1373 K for 2 hours. The pellets were about 10.5 mm in diameter and 1.5 mm thick, respectively. The formation and quality of compound were checked by X-ray diffraction (XRD) analysis. X-ray powder diffraction patterns of the sintered samples were measured to determine the structure and confirm the phase purity. X-ray diffraction patterns as a function of temperature were obtained using an Edmund Buhler high temperature attachment. A tantalum strip with a radiation shield was used as sample holder and temperature was controlled within ± 0.1 K. Cu-Kα radiation was used for recording the diffraction patterns using a Siemen's X-ray diffractometer (D500) operating in the Bragg-Brentano geometry. Diffraction patterns were analyzed using STOE software for indexing the peaks and obtaining the refined lattice parameters. Energy dispersive X-ray analysis (EDAX) and microstructural analysis (i.e., grain size, grain distribution, voids etc.) of the samples were carried out using a Cam Scan (CS 3200) scanning electron microscope. Selected area electron diffraction (SAED) pattern were obtained using a JEOL–2000 EX II transmission electron microscope operated at 200 kV. Raman spectra were recorded using a Ranishaw micro-Raman spectrometer (model InVia) equipped with a Leica microscope and a 20× long-working distance objective. The measurements were conducted in backscattering geometry using the 514.5 nm line of an Ar-ion laser. The spectrometer resolution for 1800 l/mm grating was ~1.5 cm^{-1}. The *in situ* temperature-dependent experiments were conducted in a Linkam heating-cooling stage ensuring a temperature stability of ±0.1 K. Data acquisition time and the laser power were adjusted for obtaining a good signal-to-noise ratio. The spectra were fitted to Lorenzian line shapes to determine the peak positions, full widths at half maximum (FWHM) and intensities, using PEAKFIT software (JANDEL). Magnetization (*M~H* loop) were obtained using a vibrating

sample magnetometer (Cryogenics make) up to a maximum field of ± 50 kOe at ambient and down to 4 K. The zero field cooled (ZFC) and field cooled (FC) magnetization were measured as a function of *T* in the 4-300 K range. For *P-E* measurements, the pellets were silver electroded on both sides. The *P-E* measurements were carried out using automatic *P-E* loop tracer.

5.3 Results and discussion

5.3.1 Microstructural and structural properties

EDAX measurements were carried out on pellets of all the samples to study the chemical composition. The EDAX spectra (Fig. 5.1) show the presence of all the cationic elements. The scanning electron micrographs (inset to Fig. 5.1) taken on fractured surface of pellets show uniform distribution of grains. The grain size is slightly different for each La-content, but there is no correlation between the two parameters. The density of all samples was between 96.5 and 99% of the theoretical density. Table I gives the characteristic parameters of the microstructure and the tetragonal-cubic phase transition temperature for the samples. The selected area diffraction patterns indicate the polycrystalline nature of all samples and are indexed to the tetragonal phase for $0 \leq x \leq 0.3$ and cubic for $x \geq 0.4$ (inset to Fig. 5.1).

Table 5.1 Compositional dependence of grain size, relative density and tetragonal-cubic transition temperature ($T_{T\text{-}C}$) for $BLFPT_x$ ($0 \leq x \leq 0.5$).

x-La	0	0.2	0.3	0.4	0.5
Grain size (μm)	0.95	1.2	1.15	1.5	1.2
Relative density	96.5%	97%	99%	99%	99%
$T_{T\text{-}C}$[b]	988 K	773 K	618 K	Cubic	Cubic

[b]Ref[28]

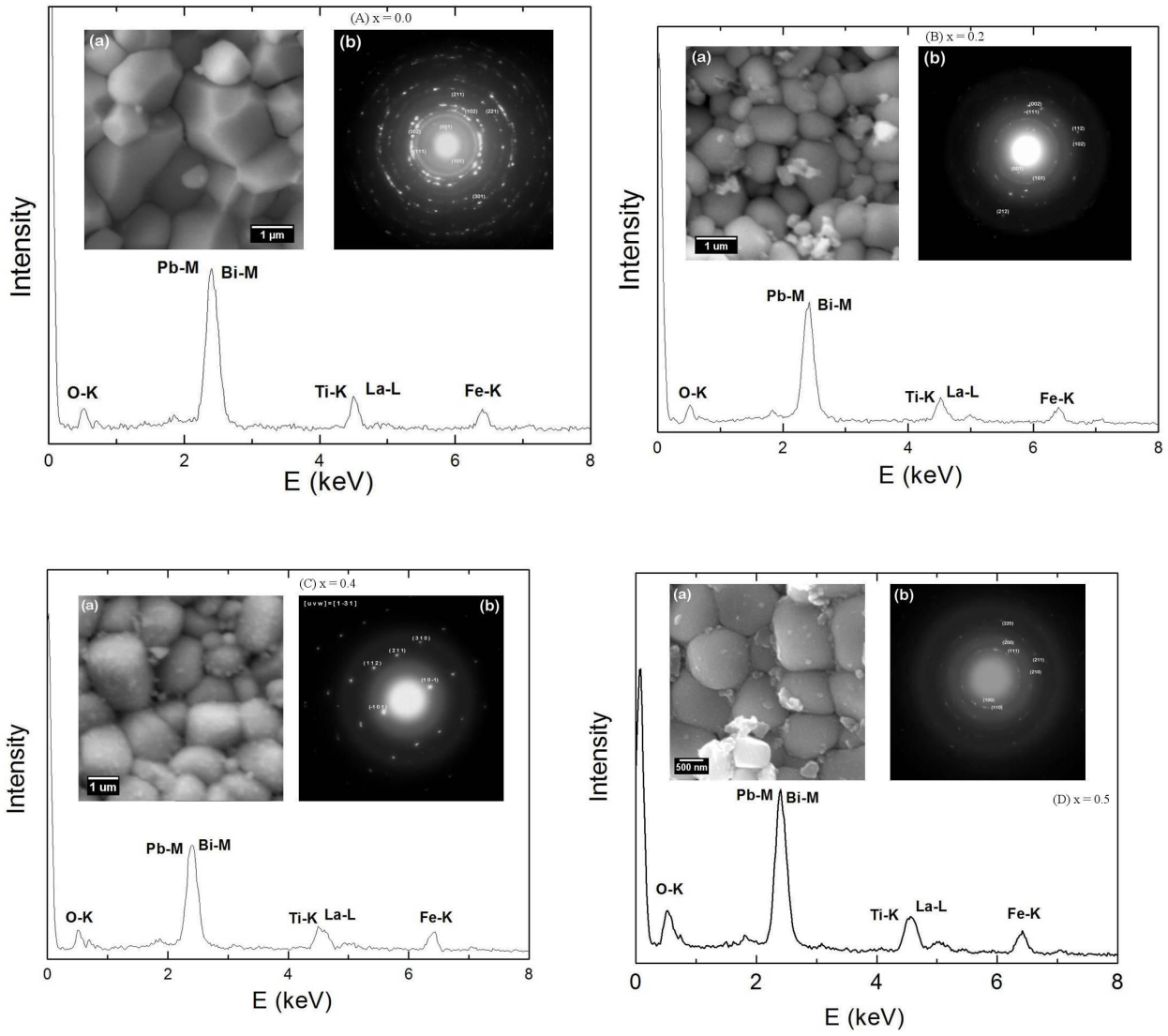

Figure 5.1 EDAX spectra of BLFPT$_x$ for x = (A) 0.0, (B) 0.2, (C) 0.4 and (D) 0.5. Inset (a) shows the SEM image and inset (b) shows SAED pattern.

Figure 5.2 shows X-ray diffraction patterns from the pure and La-substituted BF-PT ($0 \leq x \leq 0.5$). All the diffraction peaks could be fitted to the tetragonal phase with space group *P4mm* for $x \leq 0.3$. The tick pattern shown at the bottom of the figure is the calculated peak positions for the tetragonal phase for $x = 0$. It may be pointed out that it is in principle possible to fit this pattern also to centrosymmetric space group *P4/mmm*. However, as BF-PT exhibits ferroelectric properties, it is more appropriate to analyze the structure under non-centrosymmetric space group *P4mm*. From the x-ray reflections, it can be seen that as there are no unindexed lines, the

compounds are single phase. The (001) reflection at 20° 2θ is found to shift towards (100) peak and the two merge at x = 0.4. This suggests a reduction in the c-cell parameter of tetragonal phase as x increases and attaining a value same as that of cell parameter a for x = 0.4. Similar merging of doublets at 2θ ~ 32°, 47° and 53° is also found corresponding to (101)-(110), (002)-(200) and (201)-(210) reflections, respectively. The c/a ratios were calculated to be 1.133, 1.047 and 1.022 for x = 0.0, 0.2 and 0.3, respectively. One can notice that the lattice anisotropy (c/a) becomes smaller with increasing La-content. For $x \geq 0.4$, the diffraction patterns fit to a cubic structure with space group *Pm3m*. Thus, the structural change from tetragonal to cubic phase arises due to the homovalent substitution of Bi (ionic radius 1.34 Å) by La (ionic radius 1.36 Å).[29] Figure 5.3 shows the variation of the cell parameters as a function of La-composition. An unusually large tetragonality (c/a = 1.133) is found for x = 0.0, which decreases to 1.022 for x = 0.3. For $x \geq 0.4$, the tetragonal distortion disappears and a cubic phase with lattice parameter a = 3.9467(2) Å emerges.

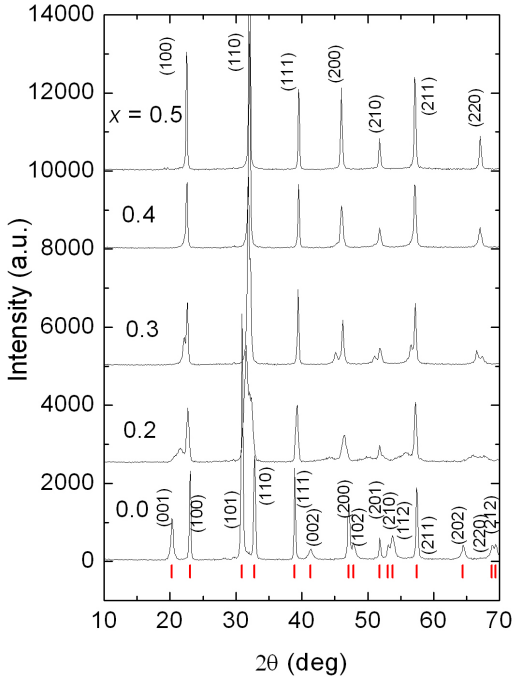

Figure 5.2 X-rays diffraction patterns of $(Bi_{1-x}La_x)_{0.5}Pb_{0.5}Fe_{0.5}Ti_{0.5}O_3$ ($0 \leq x \leq 0.5$). The tick pattern is the calculated peak positions for the tetragonal phase (*P4mm*) for x = 0.

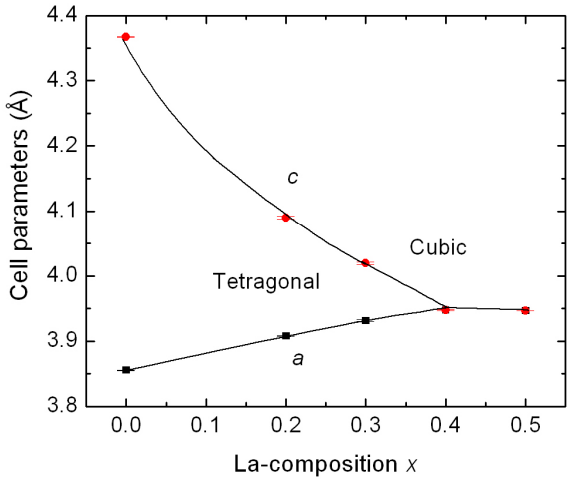

Figure 5.3 Variation of the lattice parameters (*c* and *a*) as a function of composition in the La-substituted BF-PT solid solution system, ($0 \leq x \leq 0.5$). The curves drawn through the data are guides to the eye.

5.3.2 Raman Scattering at ambient from La-substituted $BiFeO_3$-$PbTiO_3$

As mentioned earlier, $PbTiO_3$ (PT) is a classical example of tetragonal ferroelectric material at ambient temperature and belongs to the space group *P4mm*. The irreducible representation of optical phonons in this phase is $\Gamma_{opt} = 3A_1 + 4E + B_1$, where A_1 and E modes are both Raman and Infrared active, whereas the B_1 mode is only Raman active. Since BF-PT also has the same symmetry, the same set of modes is expected here too. Figure 5.4 shows the Raman spectrum of pure BF-PT and also those of La-substituted compounds. Raman spectra of La-substituted BF-PT will be discussed later.

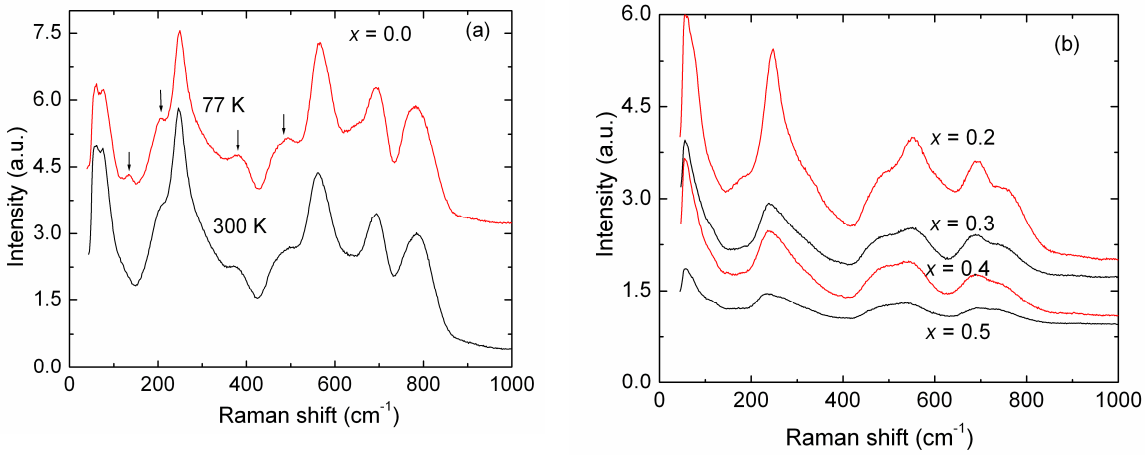

Figure 5.4 (a) Raman spectra of $(Bi_{1-x}La_x)_{0.5}Pb_{0..5}Fe_{0.5}Ti_{0.5}O_3$ sample measured at 300 and 77 K (For $x = 0.0$) (b) Raman spectra of $BLFPT_x$ samples ($0\ 2 \leq x \leq 0.5$) at ambient.

In the case of pure BF-PT, five prominent peaks and three shoulders are discernible. By analyzing the spectra using PEAKFIT, ten modes could be identified in the frequency range 40–1000 cm^{-1}. The fitted mode frequencies are listed in table 5.2 and are assigned by comparing with those of PT.[30] The lowest frequency mode appears at 65 cm^{-1}. In Raman spectrometers with single monochromator and edge filter, often spectra are strongly attenuated at lower cm^{-1}. However, the edge filter used in this set up permits measurements down to 30 cm^{-1}. In order to

Table 5.2 Mode frequencies of the Raman bands in pure and La-substituted BF-PT for $x = 0$ and 0.5 obtained from Lorentzian fitting of spectra. The reported mode frequencies of $PbTiO_3$ single crystal and their assignments are also included for comparision.

$(Bi_{1-x}La_x)_{0.5}Pb_{0.5}Fe_{0.5}Ti_{0.5}O_3$ Present work Mode frequency (cm^{-1})		Assignment	$PbTiO_3$[a]
$x = 0.0$	$x = 0.5$		Mode frequency (cm^{-1})
65	63	$E^{(1)}$- TO	89
113	-	$E^{(1)}$-LO	130
199	-	$A_1^{(1)}$-TO	148
247	233	$E^{(2)}$-TO	220
284	276	$E^{(4)}$-TO, $E^{(4)}$ LO	290
380	-	$A_1^{(2)}$-TO	362
476	477	$E^{(2)}$-LO	440
566	540	$E^{(3)}$-TO	508
689	684	$A_1^{(3)}$-TO	650
789	733	$E^{(3)}$-LO	720

[a]Ref.[30]

confirm, whether the 65 cm^{-1} is genuine or an artifact of the notch filter, Raman spectrum of another compound $Zr(WO_4)_2$, which has a Raman peak at 41 cm^{-1}, was also recorded. The spectrum exhibited a clear mode at 41 cm^{-1} (not shown here) confirming the genuineness of the 65 cm^{-1} mode in BF-PT. One can see that none of the three A_1-LO modes are present; this may be either due to insufficient intensity or due to small LO-TO splitting of A_1 modes. All these modes are broad as compared to those reported[30] for $PbTiO_3$ single crystal. The broadening can arise due to several factors. The Raman spectrum of a polycrystalline powder sample is expected to be broader because of scattering of phonons at grain boundaries. In addition, because of randomly oriented grains, the phonon propagation direction is random with respect to crystallographic direction. Hence, the modes with mixed A_1-E character or mixed LO-TO character can arise. This is found even in polycrystalline powders and thin films of $PbTiO_3$.[31] The broadening of spectrum can also arise due to finite (ambient) temperature of the sample, because phonon life-times are known to decrease as temperature is increased. In order to confirm whether the Raman bands become sharper upon lowering temperature, we have also measured the spectrum at 77 K and the same is included in Fig. 5.4(a). One can see that all the major peaks have nearly the same width while some of the weak bands that existed as shoulders such as those at 131, 199, 384 and 478 cm^{-1} (labeled with arrows), become more prominent at 77 K. Thus, the temperature does not play a dominant role in determining the widths of the Raman bands in this mixed-crystal system. Another reason for phonon line-shape broadening could be the substitutional disorder arising from the random occupancy of cation site *A* by Bi / Pb and of cation site *B* by Fe / Ti. Consider a unit cell containing either FeO_6 or TiO_6 octahedron. Depending on the magnitude of the Fe-O and Ti-O force constants the bond-distances can fluctuate from one unit cell to the other. This would make the characteristic vibrational frequencies of the two octahedra different. Although X-ray diffraction gives average cell

parameters, and average atom positions for *A*, *B*, and O, on a microscopic scale there are fluctuations in the bond-lengths and microscopic strains in the mixed-crystals.[32] Assuming that a given unit cell has TiO_6 octahedron, the six neighboring unit cells may have either TiO_6 or FeO_6 octahedra with a 50% probability. Thus, there are large number of ways in which different octahedral can occupy neighboring cells. Each of these configurations would result in slightly different vibrational frequencies and the total Raman lines shape. For example, for Ti-O stretching vibration, the spectrum will be a weighted sum of all possible frequencies. This argument is also valid for Bi-O and Pb-O vibrations. Thus, broadening of all modes is expected in 50-50 random solid-solution BF-PT as compared to pure PT. Raman spectra of La-substituted BF-PT, shown in Fig. 5.4(b), exhibit gradual change. For $x = 0.2$ the Raman features are nearly the same except that the intensity is slightly reduced. For $x = 0.3$, eight distinct Raman modes could be found in the same frequency range. The peaks are further broadened and the intensities reduced upon increasing the La-composition. Figure 5.5 shows the individual components and total fitted spectrum for $x = 0.4$. Similar Lorenzian fitting has been done for other compositions also. Table 5.2 also lists the frequencies of observed Raman modes for $x = 0.5$. In the cubic phase the fitting yielded seven modes. The modes in the cubic phase are even broader due to substitutional disorder. Substitutional disorder has been shown to cause significant broadening of Raman line-shape in other mixed crystals.[33]

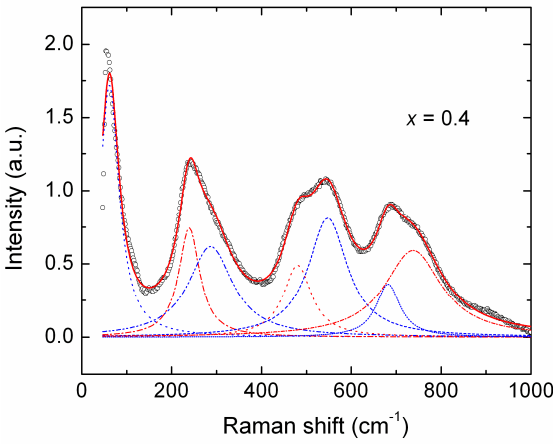

Figure 5.5 Raman spectrum fitted to sum of 7 Lorenzian peaks for $x = 0.4$ composition. Individual fitted peaks are also shown.

Table 5.3 Correlation diagram between irreducible representations of the C_{4v} (tetragonal) and O_h (cubic) point groups.

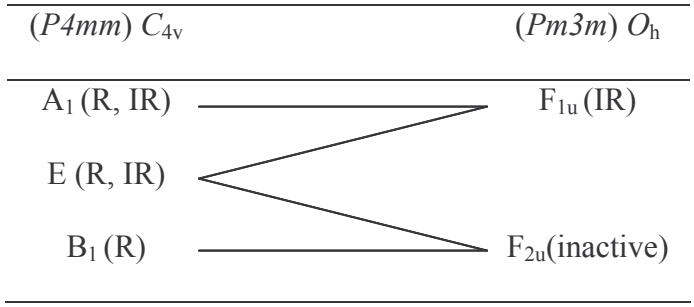

As mentioned earlier, upon La-substitution the tetragonal anisotropy reduces and the system becomes cubic for $x \geq 0.4$. The irreducible representation for the optical phonons in the cubic phase is $\Gamma_{opt} = 3F_{1u} + F_{2u}$, where the F_{1u} mode is infrared active, and F_{2u} is a "silent mode", since it is inactive both in the Raman and in the infrared. These modes can be correlated to those of the tetragonal phase via a correlation diagram (table 5.3). Thus, no Raman active modes are expected in the cubic phase. On the other hand, seven of the modes of the tetragonal phase for $x = 0.3$ could be identified unambiguously in the cubic phase also. The modes in the cubic phase that have correspondence with those of the tetragonal structure appear to arise due to the breakdown of the Raman selection rule due to the substitutional disorder at the cation site and essentially represent the phonon density of states. Similar symmetry-forbidden Raman scattering has been reported in $BaTi_{1-x}Zr_xO_3$ and $BaCe_xZr_{1-x}O_3$.[19, 34] Very recently a small rhombohedral distortion (space group *R3c*) of the cubic phase has been reported, based on the presence of very weak satellite peaks in the neutron diffraction for $x = 0.5$ system.[35] It may be pointed out that for the rhomohedral symmetry, a total of thirteen Raman active phonons ($4A_1 + 9E$) are expected.[36] On the other hand, in the present study we find only seven modes for $x \geq 0.4$. Furthermore, all these modes continue to have correspondences with those of the tetragonal phase. In view of this, it is inappropriate to assign the modes of $x = 0.4$ and 0.5 to those arising from a rhombohedral

structure. In fact, the rhombohedral angle of the basic pseudo-cubic cell turns out to be 90.03° from the reported hexagonal primitive cell parameters.[35] It is likely that this small distortion is not able to activate the modes predicted for this symmetry. Thus, it is reasonable to attribute the spectra to symmetry-forbidden scattering.

In order to examine the manner in which total Raman intensity depends on the composition, we measured the Raman spectra at large number of spots on each pellet and obtained the average integrated intensity (integrated from 40 to 1000 cm^{-1}). In order to make this intensity free from extrinsic factors such as laser power, focusing and alignment, a fused-quartz plate, placed next to the pellet, was also measured as a reference sample. Raman intensity from quartz plate was also integrated in the same spectral range. The total Raman intensity is shown in Fig. 5.6 after normalizing with that of the quartz. One can see that the scattered intensity decreases rapidly as x approaches tetragonal-cubic transition boundary. As the tetragonal distortion ($c/a - 1$) is only 0.022 at $x = 0.3$, the Raman intensity has exhibited a large decrease as compared to lower x values. The fact that intensity does not become zero in the cubic phase implies that the symmetry-forbidden scattering is significant.

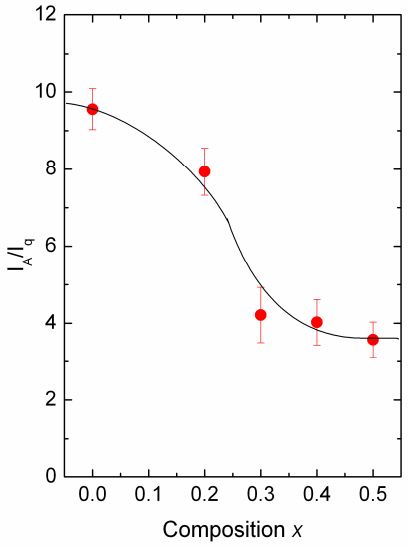

Figure 5.6 Dependence of normalized integrated intensity on La-composition. Curve through the data is guide to the eye.

Figure 5.7 shows real part of dielectric constant (ε_r) as a function of temperature at different frequencies for x = 0.5. It is evident that a diffuse (relaxor-type) phase transition is exhibited similar to that reported by others for 50% La-substituted BF-PT.[12] As the aim of the present study is to investigate the phonon spectra, the dielectric data is included only for the sake of completeness.

As the relaxor behavior in this system is well established,[12] a discussion on the possible correlation of Raman spectra with the relaxor behavior is in order. Relaxor behavior arises due to existence of polar nano-regions (PNRs) in randomly substituted mixed-crystal systems.[14, 25, 37] Microscopic compositional fluctuations or chemical ordering over a few nm length scale can give rise to formation of PNRs although X-ray diffraction yields an average cubic structure consistent with the average stoichiometry.

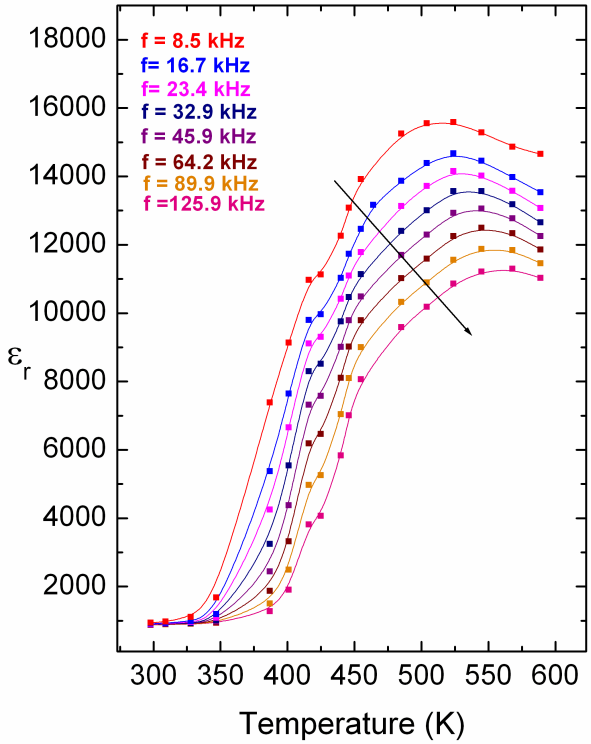

Figure 5.7 Temperature dependence of real part of relative dielectric permittivity at various frequencies between 8 and 125 kHz for x = 0.5. The arrow indicates the direction of increasing frequency.

Within the PNR the local structure could be different due to the chemical ordering. As the Raman scattering is very sensitive to changes in local structure, sharp Raman peaks[25, 37] are

sometimes found, though not allowed by the cubic point group symmetry. In the present case, we do not find appearance of new sharp peaks riding over the symmetry forbidden broad spectrum. It is also worth examining if one can correlate/identify specific phonons with the magnetoelectric effect. In this context it is important to point out that ferroelectric and magnetic properties originate (a) in pure compounds from the equilibrium positions of different atoms in the unit cell and (b) in the substituted mixed-crystals from the displacements of atoms from ideal positions and / or formation of chemically ordered polar regions of nanometer length scale. Thus, optical phonons do not play direct role in determining the multiferroic properties. On the other hand, phonons do play important role in inducing structural phase transitions and other physical properties. The mode frequencies are shown as function of composition in Fig. 5.8. Some of modes such as $A_1^{(1)}$-TO, $E^{(2)}$-TO, $E^{(3)}$-TO, $E^{(3)}$-LO show a decrease of the frequency as x increases, while a few other modes such as $E^{(1)}$-TO, $E^{(2)}$-LO, $A_1^{(3)}$-TO etc. do not change significantly. It is worth examining the consequences of changes in the tetragonal distortion on the phonon spectra. As one can see from the correlation diagram, the triply degenerate F_{1u} mode

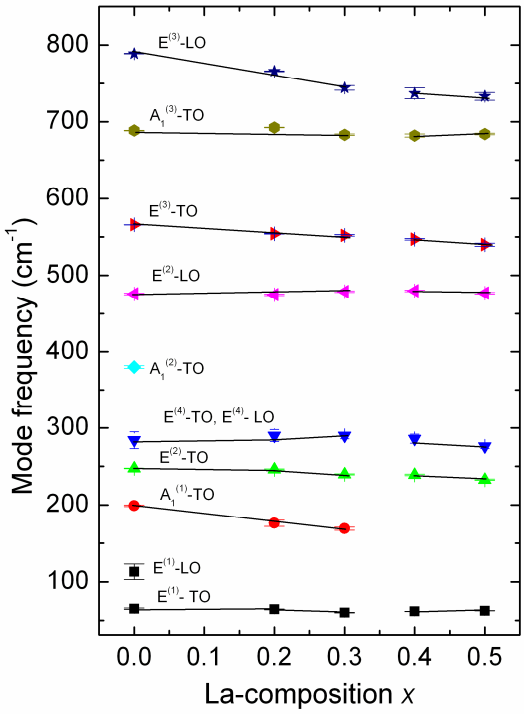

Figure 5.8 Dependence of Raman mode frequency on La-composition. Lines through the data are guides to the eye.

of the cubic phase splits into a singly degenerate A_1 and a doubly degenerate E mode due to lowering of symmetry to tetragonal.[30, 38] Thus, a reduction in the anisotropy splitting is expected as La-concentration is increased. Figure 5.9 shows the separation of $A_1^{(1)}$-TO and $E^{(1)}$-TO as a function of tetragonal distortion *c*/*a*. Note that A_1-E anisotropy splitting reduces as *c*/*a* approaches unity. It may be pointed out that the $A_1^{(1)}$-TO and $E^{(1)}$-TO modes have been identified as the soft phonons in $PbTiO_3$ across tetragonal-cubic transition[30] at 495°C. The softening of these phonons found in the present work as a function of La-composition is qualitatively similar to those of $PbTiO_3$. Figure 5.9 also shows the LO-TO splitting of the $E^{(2)}$ mode as a function of *c*/*a*. This splitting is governed by the Born's effective dynamic charges on the cations and anions. One can see that the LO-TO splitting increases upon La-substitution signifying an increase in the ionicity of the system.

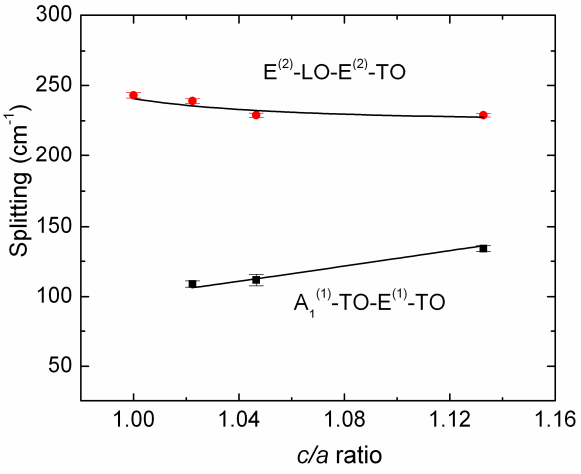

Figure 5.9 Dependence of mode splitting on *c*/*a* ratio. Lines through the data are guides to the eye.

5.3.3 *in-situ* X-ray diffraction at high temperature

In order to obtain *x*-*T* phase diagram *in-situ* X-ray diffraction measurements were made at elevated temperature. The X-ray diffraction patterns for the undoped BF-PT (x = 0) sample at elevated temperatures are shown in Fig. 5.10(a). One can notice the shift of the peaks at higher temperature. In addition, separation of some doublets such as (100) and (001) is found to reduce. For the x = 0.3 $BLFPT_x$ sample the separation of such doublets are smaller to begin with and

reduce further at high temperature (Fig. 5.10(b)). This suggests that the anisotropy reduces at high temperature for pure BF-PT as well as for doped $BLFPT_x$ samples. In pure BF-PT the diffraction pattern at 1003 K could not be fitted to the tetragonal structure; instead it fitted to the cubic space group *Pm3m*. Similarly for the doped samples the cubic phase was found on and above 783 K and 623 K for x = 0.2 and 0.3 respectively. Figure 5.11 shows the diffraction patterns for x = 0.0 on an expanded scale to highlight the behavior of (001)-(100) and (101)-(110) doublets near $2\theta \sim 22^o$ and 32^o respectively. One can see that (001) and (100) peaks shift in opposite direction and move towards each other as the temperature is increased. Similarly the (101) reflection shifts towards (110) and merges with it at high temperature. Similar merging of triplets at $2\theta \sim 45^o$, 51^o and that of a doublet at 66^o is also found corresponding to (002)-

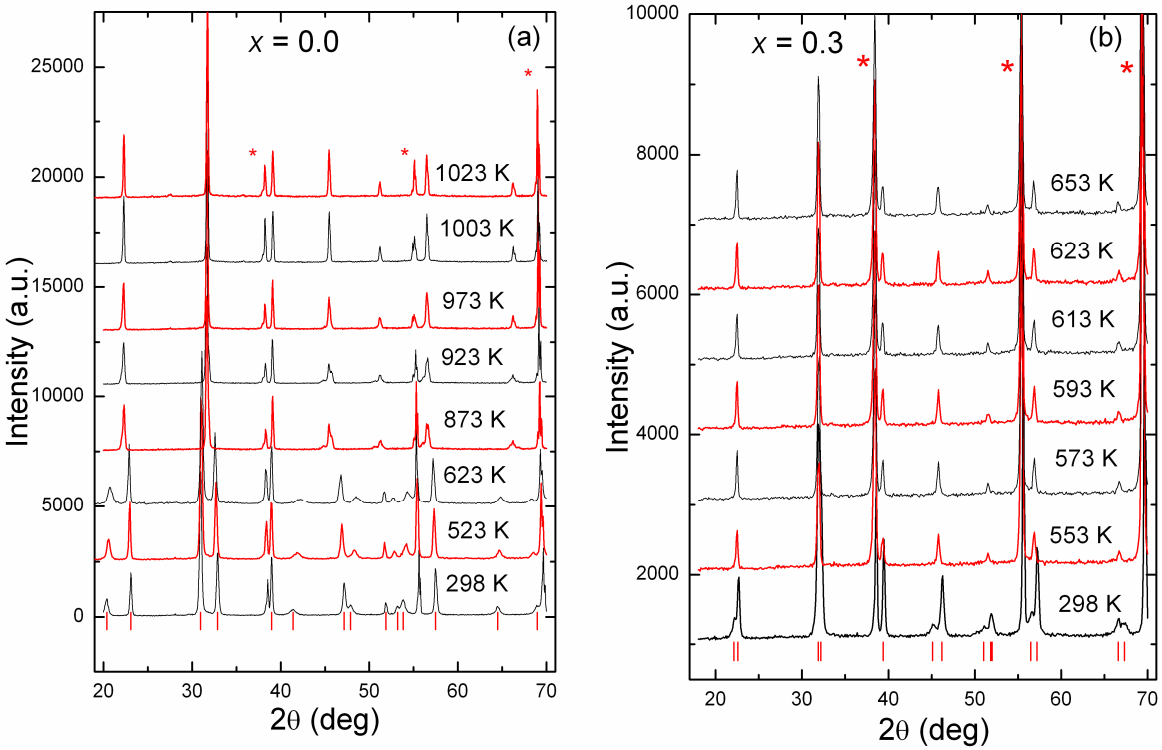

Figure 5.10 X-rays diffraction patterns of $BLFPT_x$ powders measured at different temperatures. The tick pattern is the calculated peak positions for the tetragonal phase (*P4mm*) at 298 K; (a) x = 0.0, (b) x =0.3. The asterisk (*) marks represent the Ta sample holder peaks.

(200)-(102), (201)-(210)-(112) and (202)-(220) reflections respectively. Similar behaviors are found in x = 0.2 and 0.3 samples except that the singlet formation occurs at lower temperature for higher x samples. This suggests a reduction in the c-parameter of tetragonal phase as temperature increases and approaching a value close to that of a-parameter. As mentioned earlier, the La-doping reduces the transition temperature.

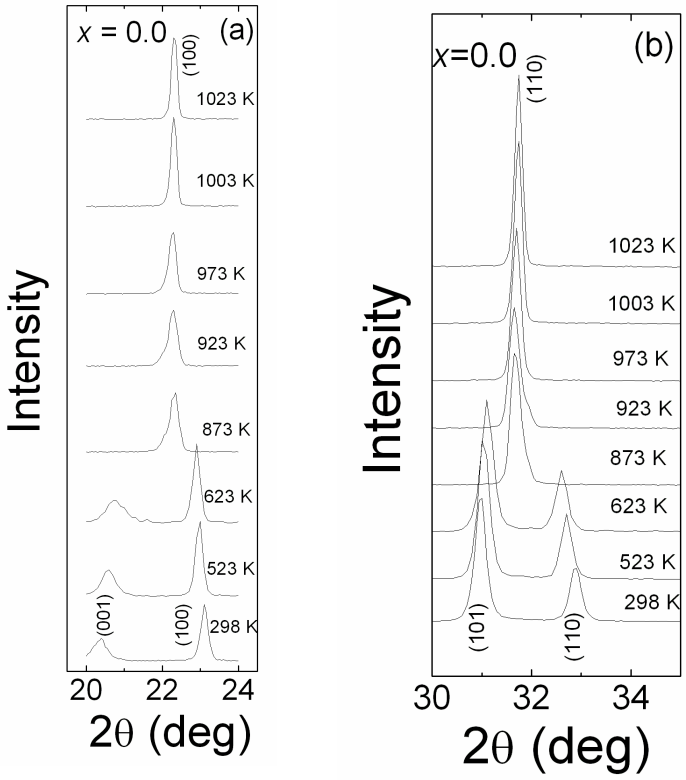

Figure 5.11 Diffraction patterns, expanded in the 2θ regions, covering doublets to highlight the anisotropy of the structure for x = 0.0 at elevated temperatures; (a) (001)-(100) doublet and (b) (101)-(110) doublet.

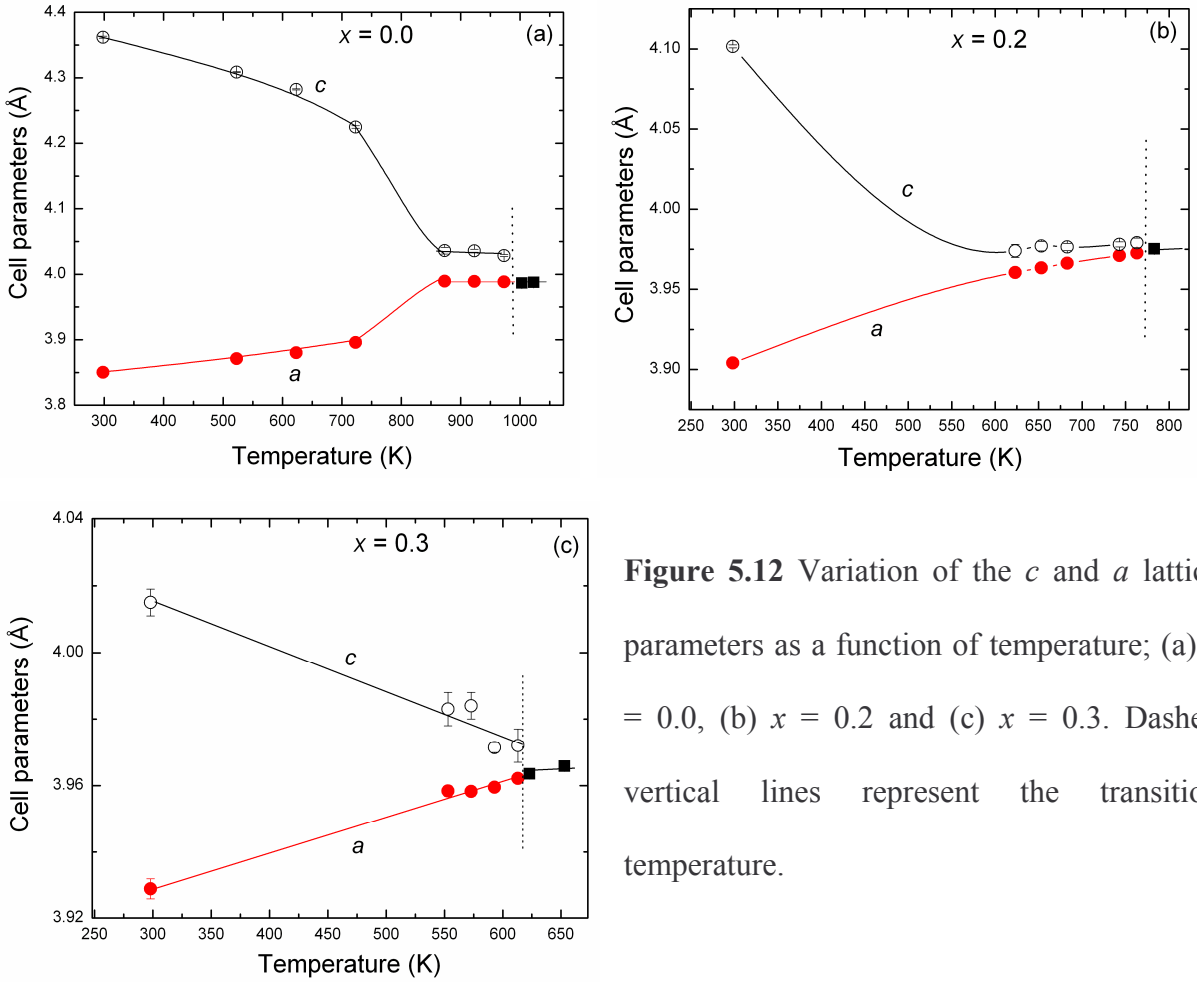

Figure 5.12 Variation of the *c* and *a* lattice parameters as a function of temperature; (a) x = 0.0, (b) x = 0.2 and (c) x = 0.3. Dashed vertical lines represent the transition temperature.

The *T*-dependences of the cell-parameters are shown in Fig. 5.12 for different La-compositions. The *in-situ* measurements were made at larger *T*-intervals away from the transition temperature and at closer intervals near the structural transition. The x = 0.0 sample exhibits an unusually large anisotropy, which decreases with the increase in temperature from c/a = 1.133 at ambient to 1.0 at 1003 K. At this temperature the tetragonal distortion disappears and a cubic unit cell with a = 3.9875(9) Å is found. For x = 0.2 and 0.3 samples also the lattice parameters show similar behavior with temperature and the tetragonal-cubic transition is found to occur at 783 and 623 K, respectively. The phase transition is primarily due to the reduction of the *c*-parameter as the increase of *a*-lattice parameter is rather small for larger value of x. Figure 5.13 shows the dependence of tetragonal-cubic transition temperature T_C on La-composition x.

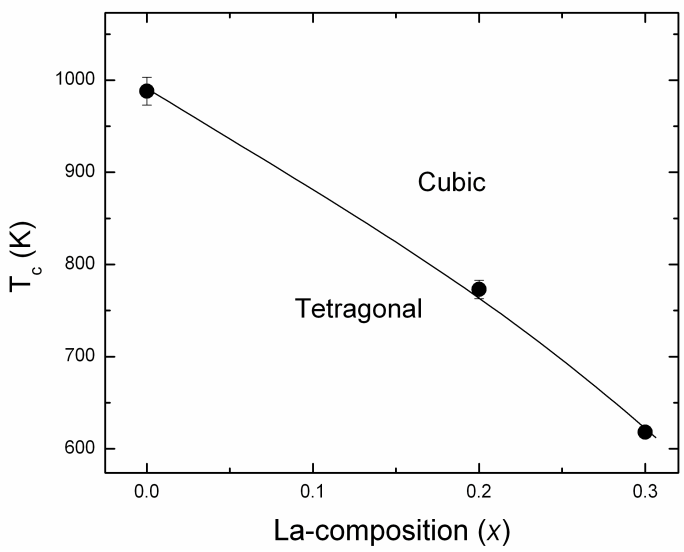

Figure 5.13 *x*-*T* phase diagram of the tetragonal $BLFPT_x$ solid-solution.

One can see that at higher x the transition occurs at lower temperatures. From these results it emerges that the anisotropy of the La-substituted BF-PT system depends both on the composition and the temperature. Increasing x as well as T reduces the anisotropy and the system transforms to a cubic phase. Thus, the decrease in the anisotropy of $BLFPT_x$ upon La-doping is essentially responsible for the lowering of T_C. It can be noted that for x = 0.4 and 0.5 solid-solutions already has a cubic structure at the ambient.[39] Hence this system was not included in the T-dependent X-ray diffraction study. Furthermore, the synthesis of x = 0.1 sample was not considered necessary as it is also expected to have a tetragonal structure with a- and c-parameters lying between those of x = 0.0 and 0.2.

5.3.4 *In-situ* Raman Scattering from $BLFPT_x$ at high temperature

As shown in Fig. 5.4(a) and discussed in section 5.3.2, the Raman bands in x = 0.0 sample are relatively sharper at 83 K, and the shoulders are better defined, Raman spectra of all the samples were measured at 83 K and analyzed. Figure 5.14 (a) shows the Raman spectra for all the compositions $0 \leq x \leq 0.5$ at 83 K. A quantitative analysis of the changes in the Raman spectra is possible only when the peak positions, line-widths and intensities of the modes are precisely obtained using curve fitting. Hence the spectra were fitted to multi-Lorenzians using the PeakFit

program. The individual components and total fitted spectrum for x = 0.0 and 0.5 are shown in Figs. 5.14(b) and (c), respectively. Similar fittings have been done for other composition also. For x = 0.0, the fitting yielding 12 peaks as shown in Fig. 5.14(b) whereas 8 peaks could be identified in the case of x = 0.5. One can see a good agreement between the total fitted spectrum and the data. Table 5.4 gives the frequencies of the Raman modes at 83 K and their assignments[30] for all the compositions. One can see that the mode frequencies do not depend strongly on the composition of La; however, some of the weak modes are not present in the mixed-crystals with higher x.

Table 5.4 Mode frequencies in $BLFPT_x$ ($0 \leq x \leq 0.5$) at 83 K.

Mode frequency (cm^{-1})					Assignment[(a)]
$x = 0.0$	$x = 0.2$	$x = 0.3$	$x = 0.4$	$x = 0.5$	
57	-	58	-	59	E-TA
78	64	82	64	70	$E^{(1)}$- TO
134	135	-	-	-	$E^{(1)}$-LO
200	-	-	-	-	$A_1^{(1)}$-TO
249	247	243	244	253	$E^{(2)}$-TO
283	304	290	296	330	$E^{(4)}$-TO
386	-	-	-	-	$A_1^{(2)}$-TO
476	482	479	482	484	$E^{(2)}$-LO
568	564	556	552	548	$E^{(3)}$-TO
648	-	-	-	-	$A_1^{(2)}$-LO
695	694	688	684	684	$A_1^{(3)}$-TO
786	758	751	741	743	$E^{(3)}$-LO

[a]Assignment of modes in the tetragonal phase is based on the comparison with mode frequencies of $PbTiO_3$ (Ref.[30]).

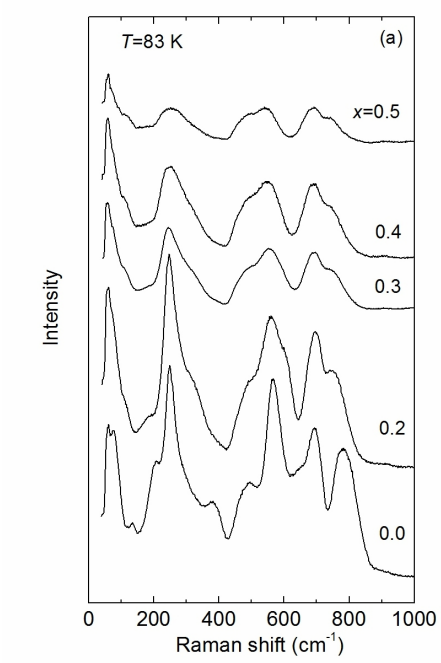

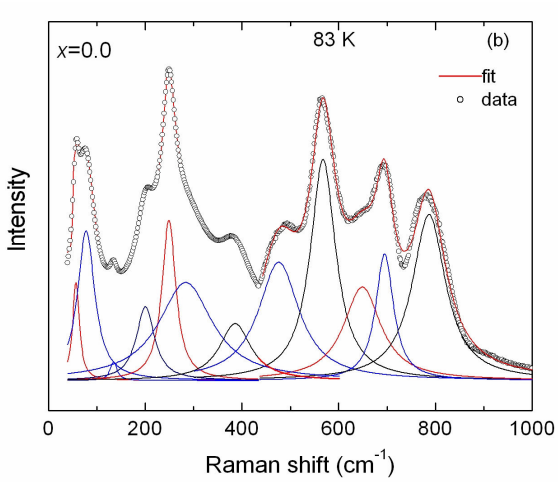

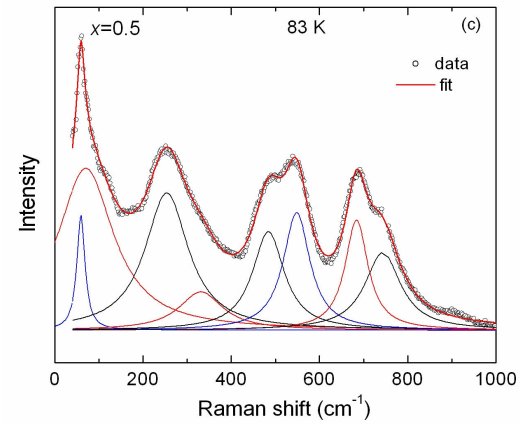

Figure 5.14 Raman spectra of $BLFPT_x$ recorded at 83 K (a) for $0 \leq x \leq 0.5$. (b) Fitted spectrum for x=0.0. Individual fitted peaks are also shown. (c) Fitted spectrum for $x = 0.5$. Individual fitted peaks are also shown.

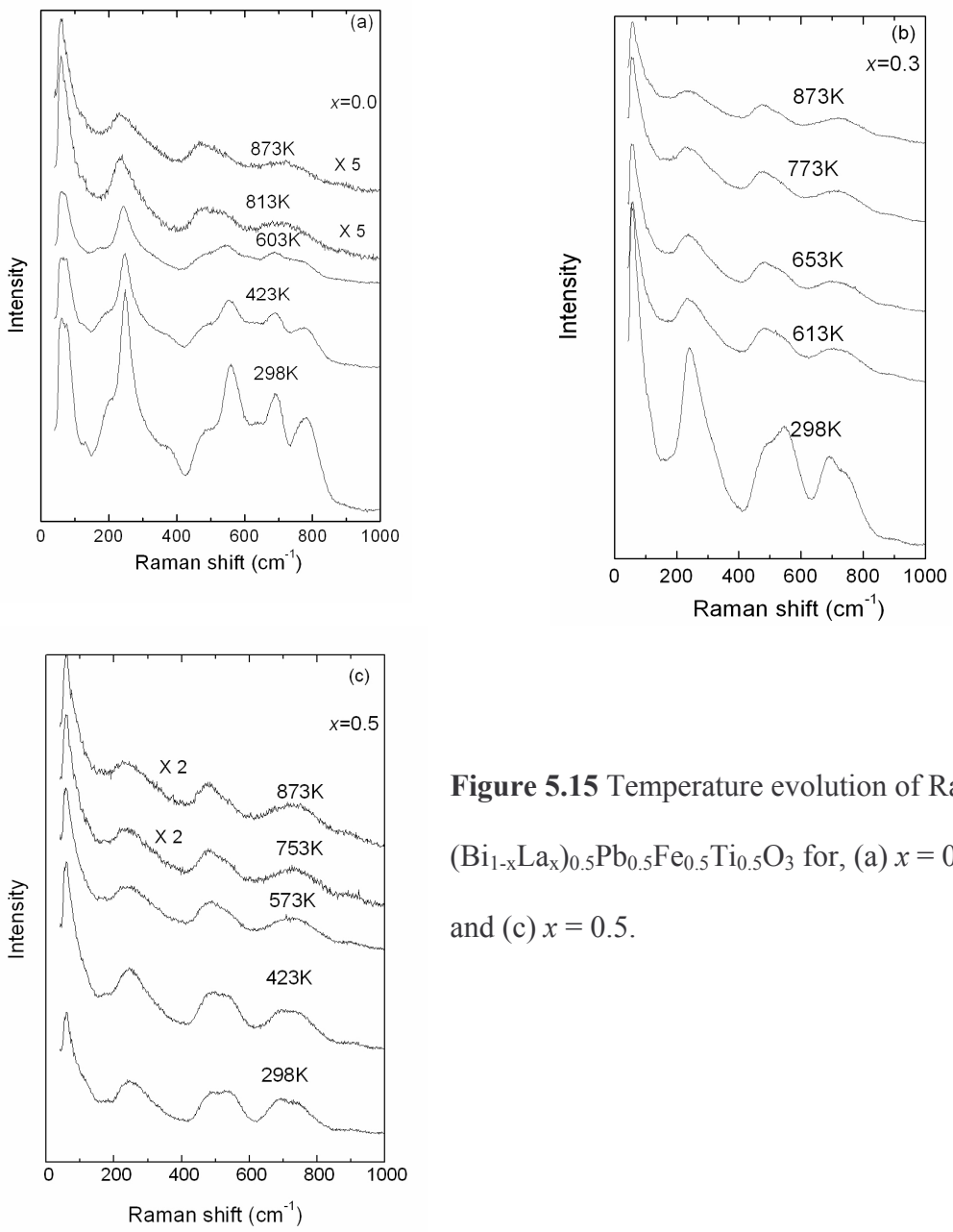

Figure 5.15 Temperature evolution of Raman spectra of $(Bi_{1-x}La_x)_{0.5}Pb_{0.5}Fe_{0.5}Ti_{0.5}O_3$ for, (a) $x = 0.0$, (b) $x = 0.3$ and (c) $x = 0.5$.

Figure 5.15 shows the Raman spectra of pure and La-substituted BF-PT samples at elevated temperature starting from ambient to 873 K. At ambient temperature also, in pure BF-PT (Fig. 5.15(a)) five prominent broad peaks and several shoulders are observed, similar to the spectrum at 83 K. As mentioned earlier, the broad nature of the Raman peaks arise due to substitutional disorder at cation sites *A* and *B*.[39] In La-substituted BF-PT the peaks are found to be broader than those of pure BF-PT and their intensities are low even at ambient (Figs. 5.15(b)

and (c)). This will be discussed later in more detail. One can see from Fig. 5.15 that at elevated temperature the spectra broaden further and the intensities are found to reduce. These spectra were also analyzed using Lorenzian fitting. The fittings of 298 and 673 K Raman spectra of pure BF-PT are shown in Fig. 5.16. One can see that the 134, 200, 386 and 476 cm^{-1} bands of the 83 K spectrum become weaker and appear as shoulder. Similar to 83 K, the spectrum at 298 K could also be resolved into a total of 12 peaks. On the other hand, at 673 K the shoulders at 200 and 385 cm^{-1} disappear and only 10 modes could be fitted to the spectrum. In the context of number of peaks used for fitting the spectrum for a given composition or temperature, it is important to point out that although it is always possible to fit more number of peaks to a given spectrum, we adopted a strategy to use the minimum number of peaks that yield a good fit. If one uses more number of modes than required, it leads to large standard errors and strong correlations in fitted parameters. At 873 K, the modes at 134, 200, 283, 386, 648 and 786 cm^{-1} could not be identified (Fig. 5.15(a)) and hence only 6 modes survived at the highest temperature. Less number of modes at high temperature arises due to insufficient intensity of weak bands.

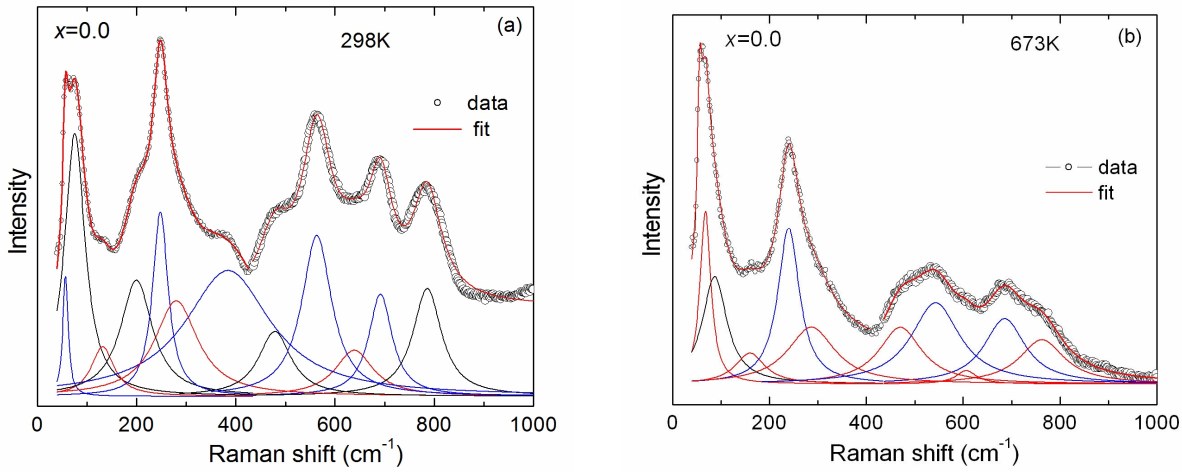

Figure 5.16 Raman spectrum fitted to sum of Lorenzian peaks for $x = 0.0$, (a) at 298 K and (b) at 673 K. Individual fitted peaks are also shown.

For x = 0.2 and 0.3 samples, 8 modes were found at ambient. Similar to x = 0 sample, here also the modes broaden with increasing temperature, as expected, and as many as 5 modes survived at 873 K. As mentioned earlier, pure BF-PT is tetragonal (*P4mm*) in ambient temperature[39] and transform to cubic phase (*Pm3m*) at 993 K.[28] Therefore, the structural transition temperature is higher than the highest temperature reached in the present measurements. The occurrence of less number of modes at the highest temperature is essentially due to broadening and weakening of modes that could not be identified in the fitting procedure. On the other hand, in the substituted mixed-crystals the tetragonal anisotropy reduces at elevated temperatures and for x = 0.2 and 0.3, and system transforms to cubic phase (*Pm3m*) at 813 and 618 K, respectively.[28] These transition temperatures are lower than the highest temperature of present investigations and hence it is possible that certain anomalies in the temperature dependence of the parameters of the modes could exist across the structural transition. An analysis of parameters such as Raman mode frequencies and the line-widths will be discussed later from the point of view of identification of the phase transition. Evolution of Raman spectrum at elevated temperature is shown in Fig. 5.15(c) for x = 0.5. Both for x = 0.4 and 0.5, as many as 7 modes are observed at ambient. All modes are broad and only 4 modes could be found at 873 K. One can see from the correlation table (Table 5.3) that across tetragonal-cubic transition the A_1 and E modes of the tetragonal phase combine to give F_{1u} infrared active mode of the cubic phase. Similarly, B_1 and E modes combine to give F_{2u} silent mode. Thus, appearance of weak Raman spectra for x = 0.4 and 0.5 samples can be attributed to breakdown of Raman selection rule due to substitutional disorder. The spectra for these compositions are likely to have large contribution from the phonon density of states. Appearance features corresponding to phonon density of states are well known to appear along with zone-center phonon Raman lines even in the single crystals of homogeneous solid solution (mixed crystals).[40] In fact the flat

regions of the dispersion curves near the zone centre and other high symmetry points in the Brillouin zone make large contribution to the phonon density of states. Thus, all the phonons, whether Raman active or not can, in principle, contribute to the disorder activated Raman scattering as found in samples for $x = 0.4$ and 0.5. The appearance of Raman spectra in the cubic phase has also been interpreted as an evidence of symmetry breaking. This is argued to arise due to the existence of nanoscale ordering (Polar Nano Regions), which is not detectable in X-ray diffraction.[25] In certain substituted compounds local chemical ordering gives additional sharp Raman lines[25] riding over the broad spectrum; however, in the present system we do not find such additional peaks.

Figure 5.17 shows the dependence of mode frequencies on temperature. One can see that frequencies of almost all the modes decrease with increasing temperature. This is understandable on the basis of anharmonicity of phonons.[41] For $x = 0.0$, the modes at 131, 199 and 638 cm^{-1} vanish at a temperature around 700 K. The mode pairs at 279 and 384 cm^{-1} and 695 and 786 cm^{-1} merge and give raise to single peaks (Fig. 5.17(a)). Similarly in the case of $x = 0.2$, only 5 modes survived at 873 K (Fig. 5.17(b)). The weak mode at 176 cm^{-1} vanishes and the modes at 246 and 290 cm^{-1} and 692 and 765 cm^{-1} merge to give rise to single peak. One can notice from Fig. 5.17(c) that the mode at 291 cm^{-1} disappears and the modes at 684 and 740 cm^{-1} merge together and show a single mode at ~ 620 K, which is close to the tetragonal-cubic phase transition temperature of 618 K for $x = 0.3$ system. In principle one can expect signatures of the structural transition for $x = 0.2$ system also; however, if we compare Fig. 5.17(b) with 5.17(c), it is found that the 290 and 692 cm^{-1} modes, which disappeared at 618 K in $x = 0.3$ compound, are already absent in the $x = 0.2$ compound much below the transition temperature of 813 K due to weak intensity. The five modes which are present above 618 K in $x = 0.3$ also exist in $x = 0.2$ compound over a wide temperature range. As a result those signatures of the phase transition are

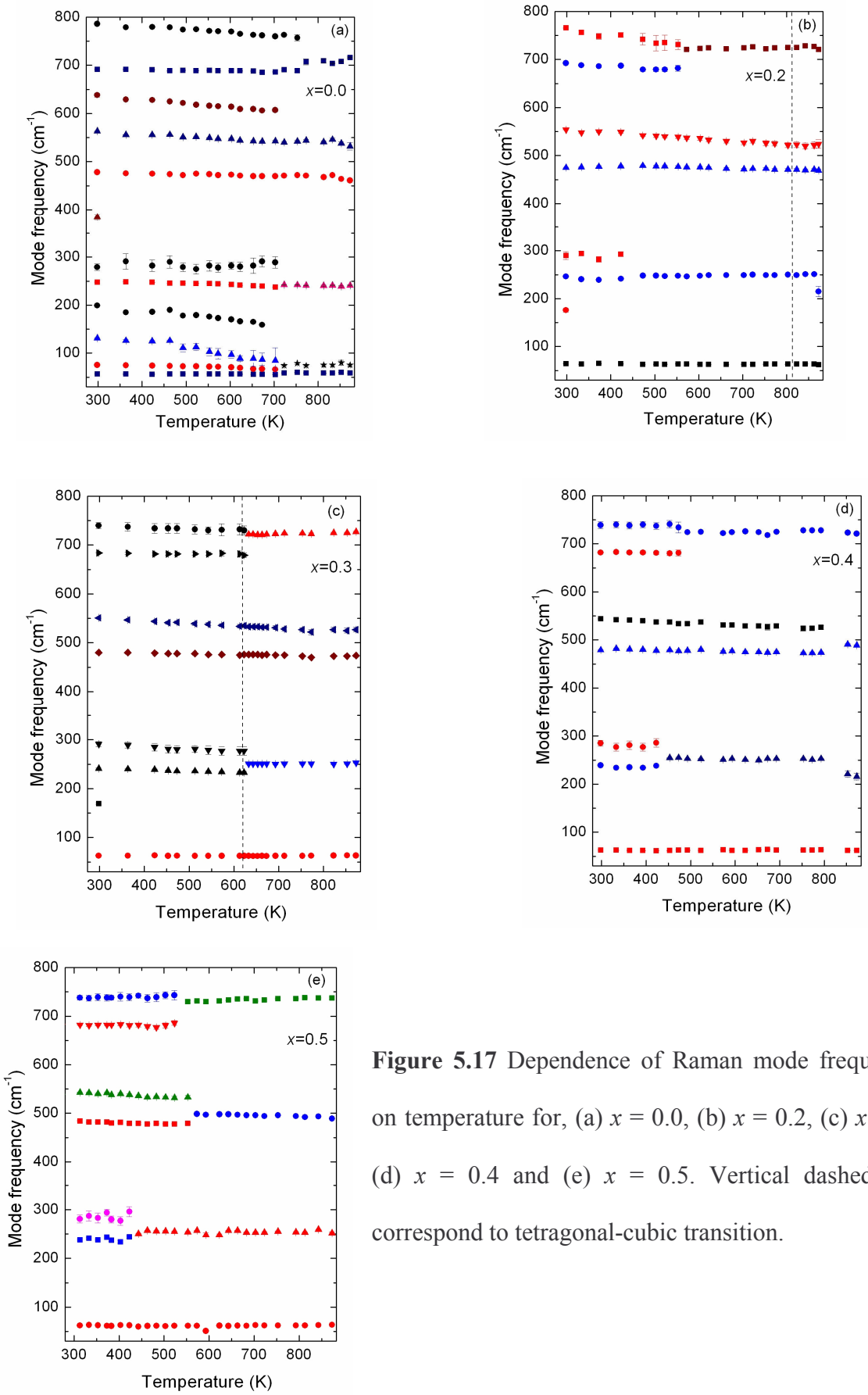

Figure 5.17 Dependence of Raman mode frequencies on temperature for, (a) x = 0.0, (b) x = 0.2, (c) x = 0.3, (d) x = 0.4 and (e) x = 0.5. Vertical dashed lines correspond to tetragonal-cubic transition.

not found in x = 0.2 near 813 K. Figures 5.17(d) and (e) show merging of modes at 285, 479 and 682 cm^{-1} with those at 239, 544 and 739 cm^{-1}, respectively. The line-widths of almost all modes are found to increase with increasing temperature. This is expected due to reduced phonon life times at elevated temperature. However, a few modes exhibit opposite behavior i.e. became narrow at high temperature.

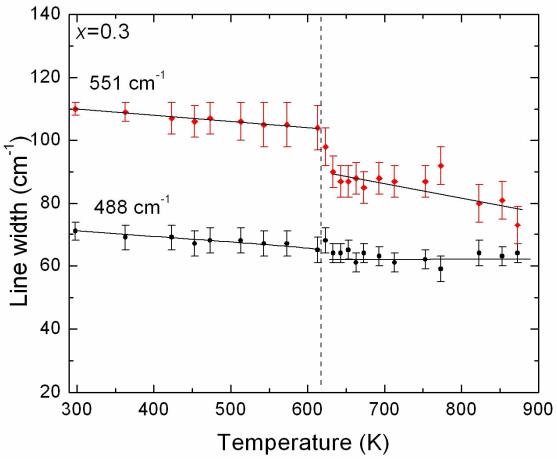

Figure 5.18 Dependence of Raman line-widths on temperature for x = 0.3. Lines through the data show the change in slope. The vertical dashed line at 618 K corresponds to the phase transition.

The temperature dependence of the line-widths of pair of modes at 488 and 551 cm^{-1} is shown in Fig. 5.18 for x = 0.3. It may be pointed out that in x = 0.3 system the neighbouring modes at 386 and 648 cm^{-1} (found in x = 0) are not found even at 83 K. Hence, the line-width parameters of the 488 and 551 cm^{-1} are not expected to be affected by other far away peaks and the temperature dependence presented in Fig. 5.18 is genuine. The line-widths of these modes also show anomaly around 618 K, associated with the tetragonal-cubic phase transition. These modes are associated with the oxygen vibrations of BO_6 octahedral. As temperature is increased, the anisotropy of the octahedral reduces. As a result, the distribution of B-O bond length is expected to reduce. This can reduce the inhomogeneous broadening of the octahedral vibrations. It may be pointed out that the homogeneous (intrinsic) broadening of phonons in pure compounds is much smaller at ambient and even at elevated temperature as compared to the inhomogeneous broadening in mixed crystals due to bond-length distribution. For example, in pure $BiFeO_3$ the two Fe-O

distances are 1.958 and 2.110 Å while in pure $PbTiO_3$ the two Ti-O distances are 1.97 and 2.032 Å. Thus, in the $x = 0.3$ sample the *B*-O bond lengths in BO_6 octahedral are expected to have a range of values. At ambient the average *B*-O bond length in the $x = 0.3$ sample in the *a*-*b* plane is 1.966Å while along the *c*-direction, it is 2.01Å. In the cubic phase the BO_6 octahedron becomes regular with a bond length of 1.983 Å. A regular octahedron is expected to have a narrow distribution of bond lengths.

5.3.5 Magnetic behaviour of BLFPT$_x$

Figure 5.19(a) and (b) present the results of magnetization measurements showing the hysteresis loops in the *M*-*H* curves for $x = 0$ and 0.5, respectively, at 4 K. Other compositions also show similar behavior. The present results for $x = 0$ are similar to those reported by Zhu *et al.*[11] for 45:55 BF-PT system. The value of magnetization obtained in the present sample is more than that reported earlier.[11] The *M*-*H* curves for all compositions show a hysteresis loop and it does not saturate up to applied field of 6 T. From the hysteresis loop, it can be inferred that magnetization arising because of two contribution. One is the ferromagnetic contribution, which gives hysteresis curve and other one arising from paramagnetic host giving rise to a non-saturating linear variation of *M* at higher field. This suggests the existence of magnetically ordered clusters in an overall paramagnetic host. Formation of magnetically ordered clusters in solid solutions has been reported in other systems also.[11] The remnant magnetization appears to depend on *x*. This has been argued to be due to the incorporation of La^{3+} in *A* site of BLFPT$_x$ leading to destruction of spiral modulated spin structure and hence Dzyaloshinskii-Moriya type interaction is enhanced.[23, 24] The *M*-*H* loop for $x = 0.5$ at different temperatures is shown in Fig. 5.19(c). A hysteresis loop with remnant magnetization appears clearly at 77 K, which becomes more enhanced at 4 K. However, at room temperature all samples are in a paramagnetic state.

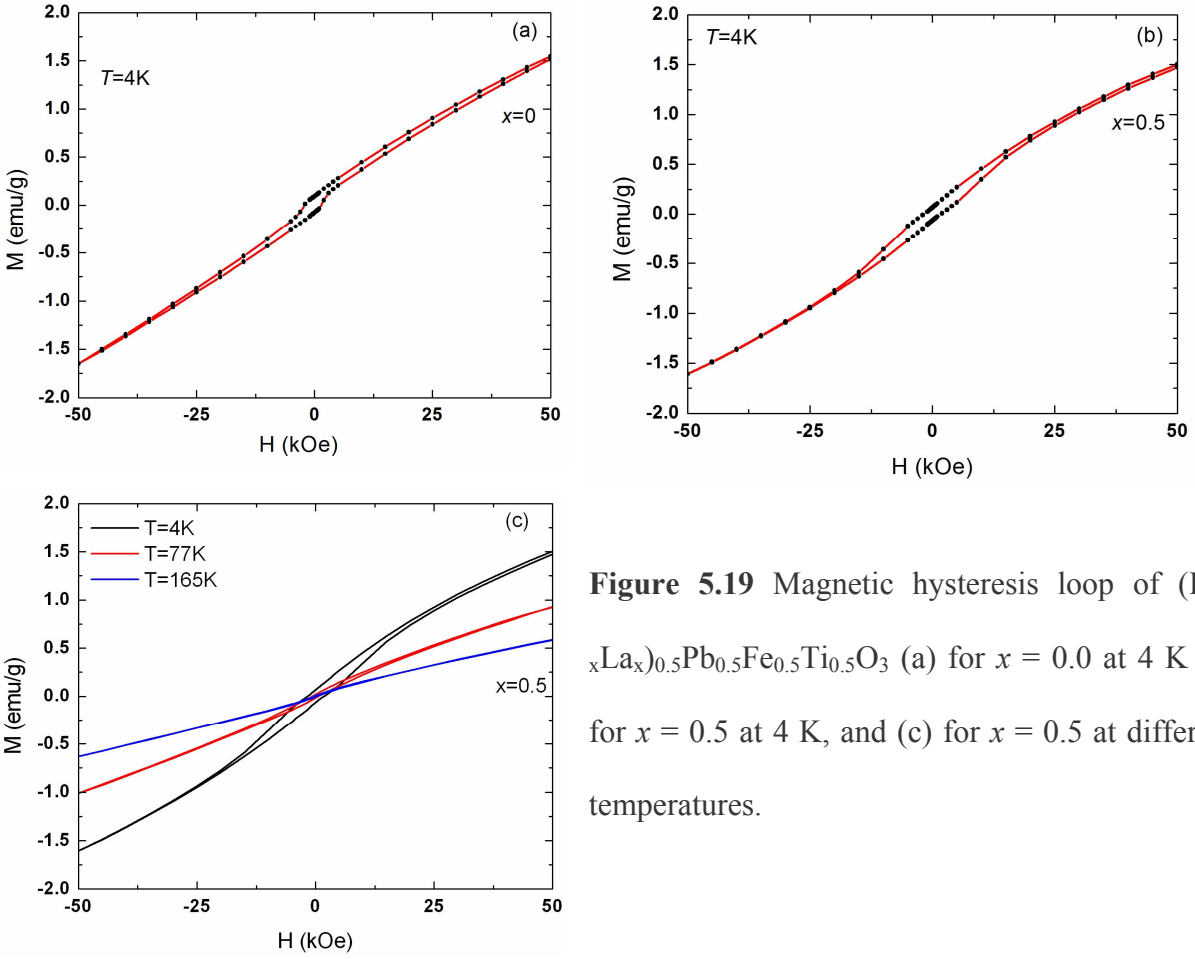

Figure 5.19 Magnetic hysteresis loop of $(Bi_{1-x}La_x)_{0.5}Pb_{0.5}Fe_{0.5}Ti_{0.5}O_3$ (a) for x = 0.0 at 4 K (b) for x = 0.5 at 4 K, and (c) for x = 0.5 at different temperatures.

In order to understand the nature of magnetic ordering, temperature dependence of magnetization was investigated at applied field of 1 kOe for all the samples. For zero field-cooled (ZFC) magnetization measurement, the sample is cooled from room temperature to 4 K without any external magnetic field, and the magnetization is recorded while heating the sample in the applied field of 1 kOe. In case of field-cooled (FC) magnetization, the sample is cooled under the same magnetic field and the magnetization is measured in the heating-run. Figure 5.20 shows the temperature dependence of ZFC and FC magnetization at static field of 1 kOe. One can see that the magnetization decreases with temperature and depends on the thermal history of the samples exhibiting irreversibility effect. The temperature at which the ZFC and FC branches coalesce is called irreversibility temperature T_{irr}. The T_{irr} is found to shift towards higher temperature with increasing La-composition. This will be discussed later in more detail.

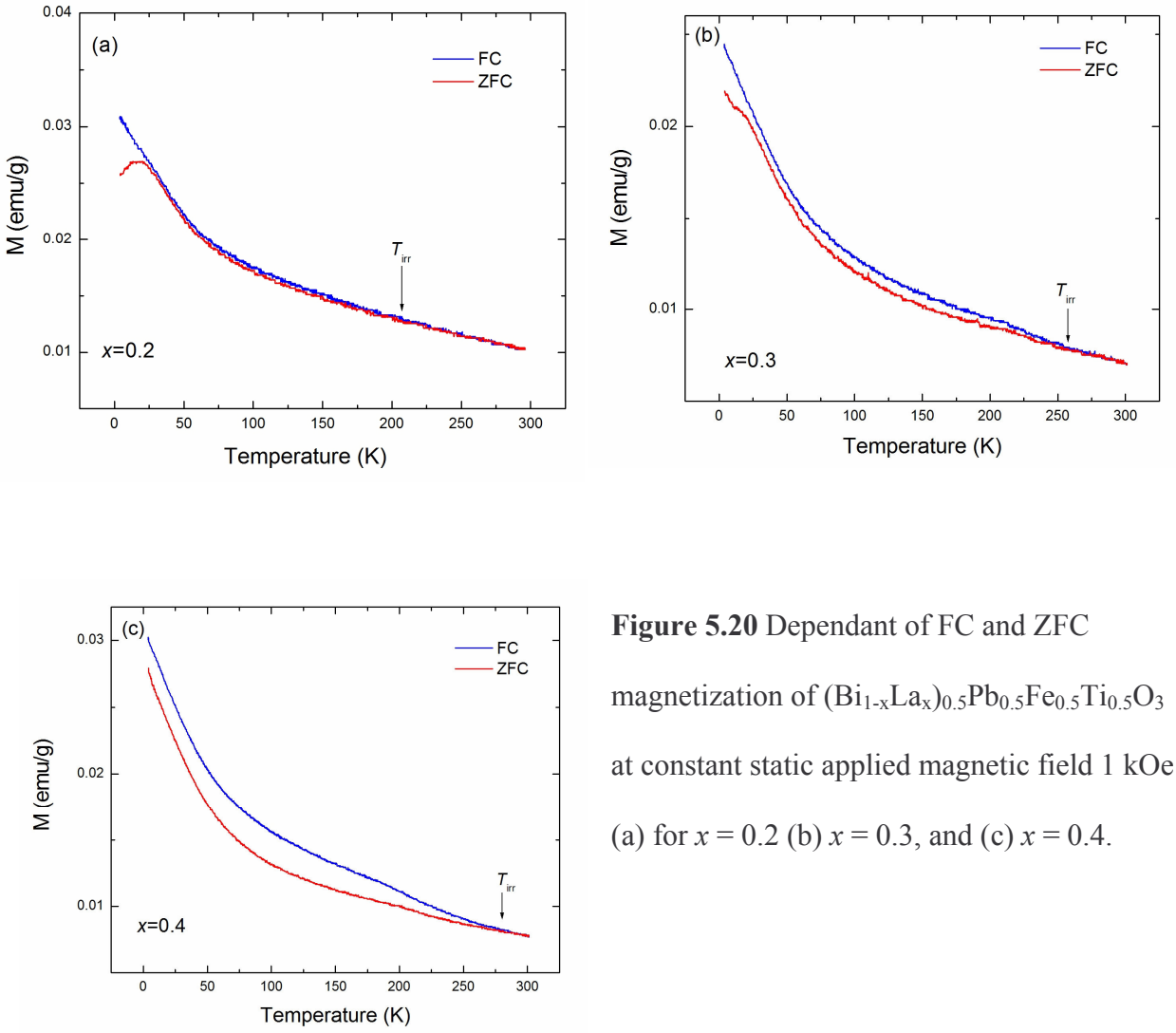

Figure 5.20 Dependant of FC and ZFC magnetization of $(Bi_{1-x}La_x)_{0.5}Pb_{0.5}Fe_{0.5}Ti_{0.5}O_3$ at constant static applied magnetic field 1 kOe (a) for $x = 0.2$ (b) $x = 0.3$, and (c) $x = 0.4$.

It may be pointed out that for $x = 0.2$ sample, the ZFC magnetization shows a cusp at low temperature. This could be due to a spin glass behavior.[25, 42] In order to confirm this ZFC magnetization was measured at different static applied magnetic fields and the dependence of the peak temperature on the applied field was obtained. Figure 5.21(a) shows the temperature dependence of ZFC magnetization for $x = 0.2$ at different static applied fields. One can see that at 1 kOe the peak of magnetization curve occurs around 17.5 K, the spin glass transition temperature T_g.

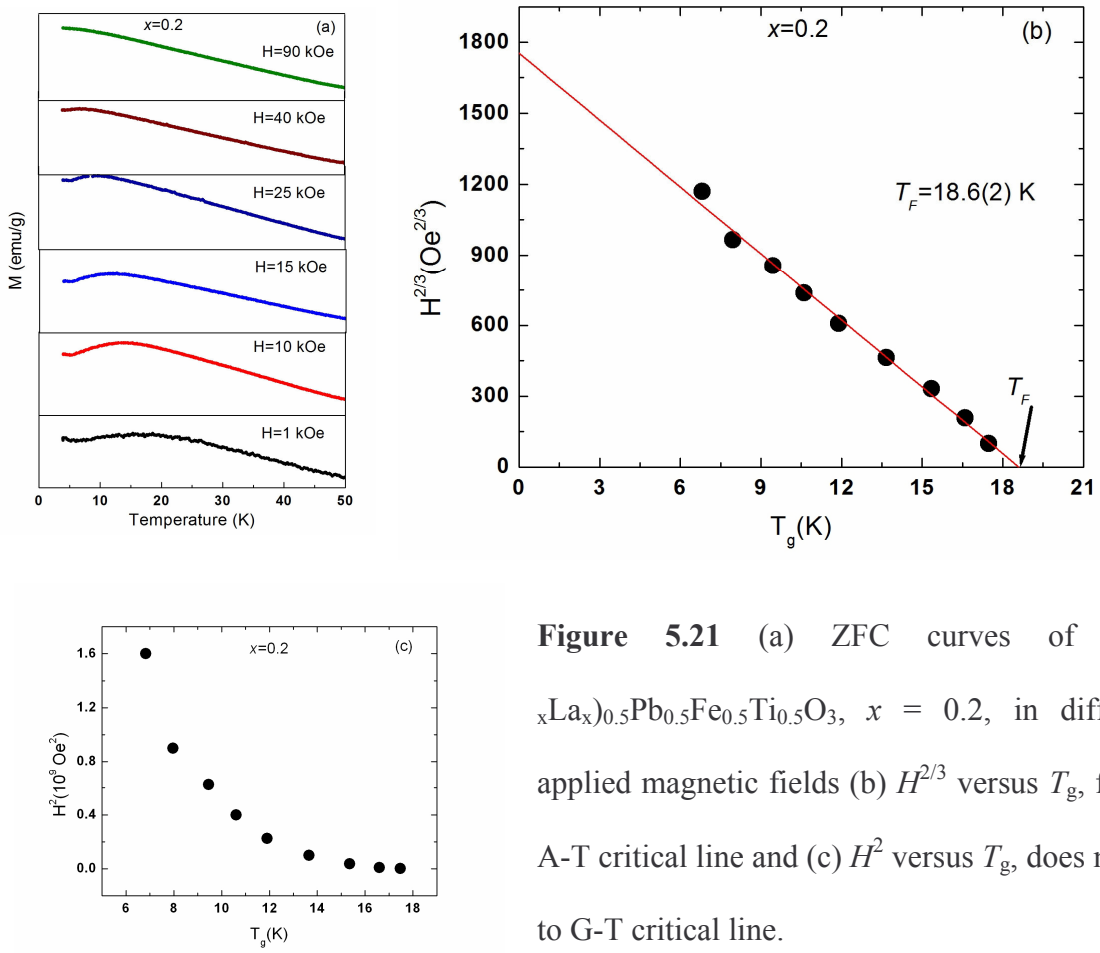

Figure 5.21 (a) ZFC curves of $(Bi_{1-x}La_x)_{0.5}Pb_{0.5}Fe_{0.5}Ti_{0.5}O_3$, x = 0.2, in different applied magnetic fields (b) $H^{2/3}$ versus T_g, fits to A-T critical line and (c) H^2 versus T_g, does not fit to G-T critical line.

The peak position T_g shifts to lower temperature at higher fields and gradually broadens. A shift of T_g with field is one of the characteristic features of a spin-glass like behavior.[42-46] A spin glass order parameter can be estimated from the field dependence of T_g (H) that vanishes linearly with temperature at freezing temperature (T_F).[44] It can be pointed out that a spin glass is described by many order parameters and not by a single one because of the existence of many phases.[45] In order to understand the frozen state and freezing transition, the behavior of magnetic field has been analyzed in the field-temperature plane (T_g vs $H^{2/3}$ and T_g vs H^2). In Fig. 5.21(b) and (c), the field dependence of T_g was analyzed with $H^{2/3}$ and H^2 dependence, respectively, for comparing with the critical lines predicted by de Almeida and Thouless (called AT line) for Ising spin glass

and by Gabay and Toulouse (called GT line) for the Heisenberg spin glass.[42-45] As can be seen, the data fits well with AT line implying an Ising spin glass and T_F was found to be 18.6 ± 0.2 K. The exact nature of frozen disorder and magnetic frustration responsible for the spin glass-like behavior is not well understood. However, a possible conjecture is that some of the diamagnetic spin clusters involving Ti^{4+} ion could have embedded into the ferromagnetic matrix involving Fe^{3+} ion because of almost equal ionic radii and short-range ordering of these ions due to charge difference causing the magnetic frustrations and randomness necessary for the origin of spin-glass behavior. The absence of spin-glass behavior for $x \geq 0.3$ implies that La-doping has a significant role in affecting magnetic properties of the systems. However, further studies are needed to explore the role of La in tuning the magnetic properties.

It may be pointed out that because of *B*-site being randomly occupied by Ti/Fe with equal probability, the Fe^{3+} ion has, on the average, only 3 Fe^{3+} neighbours that can participate in the magnetic ordering. However, the nature of the magnetic interaction remains same, i.e. each Fe^{+3} ion interact magnetically with neighboring Fe^{+3} ions. Hence, due to cooperative magnetic interaction of Fe^{+3}-O-Fe^{+3}, the magnetic ordering arises in this system.[11] The magnetic ordering temperature is the temperature at which the cooperative magnetic interaction sets in and forms a spin-network. However, above the magnetic ordering temperature, the spin network breaks and consequently, the cooperative magnetic interaction disappear. It can be pointed out that the magnetic interaction persists locally in the magnetic clusters up to a certain critical temperature above which the material becomes paramagnetic. We now discussed the effect of La-doping on the magnetic ordering. The magnetic ordering temperature is related to the average atomic distance of Fe^{+3}-O-Fe^{+3} along a-, b- and c-crystallographic directions.[11] It implies that longer the atomic distance, the lower the ordering temperature. In the case of $BLFPT_x$ system, for $x = 0$, the lattice parameter *c* of the tetragonal phase is larger than *a* with largest *c*/*a* than other

compositions. Hence, the average atomic distance of Fe^{3+}-O-Fe^{3+} along the c-direction is larger than that along a- and b-directions. Therefore, the magnetic interaction along the c-direction weakens earlier than that along a- and b-directions with increasing temperature, making the spin-network break. With increase in x the c/a ratio decreases (Fig. 5.22) and hence the average atomic distance along the c-direction approaches to that along a-direction which in turns enhances the magnetic ordering temperature. Therefore, increase in the magnetic ordering temperature with increasing x is understandable.[47]

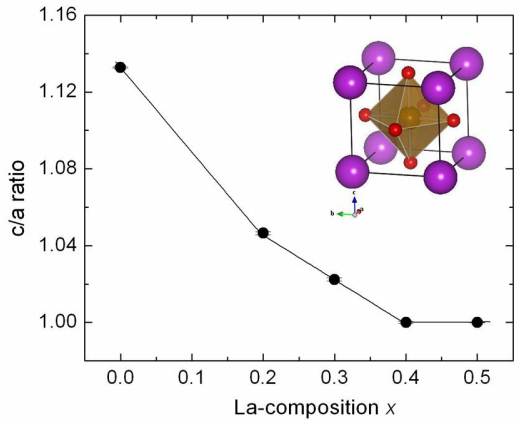

Figure 5.22 Variation of c/a ratio for $(Bi_{1-x}La_x)_{0.5}Pb_{0.5}Fe_{0.5}Ti_{0.5}O_3$ ($0 \leq x \leq 0.5$) with composition x. Lines through the data are guides to the eye. Inset shows the ABO_3 perovskite structure displaying BO_6 octahedron.

5.3.6 Ferroelectric properties

Figure 5.23(a) shows the ferroelectric hysteresis loop of $BLFPT_x$ at ambient. Well defined hysteresis loops were observed with increasing La-composition. However, the saturation of polarization was not found to occur due to inadequate applied electric field. Note that the slope of the major axis of the hysteresis loop, which is proportional to the dielectric constant, increases rapidly in the tetragonal phase ($x \leq 0.3$) suggesting that the dielectric response improves considerably as the anisotropy reduces. However, the remnant polarization remains low. One can

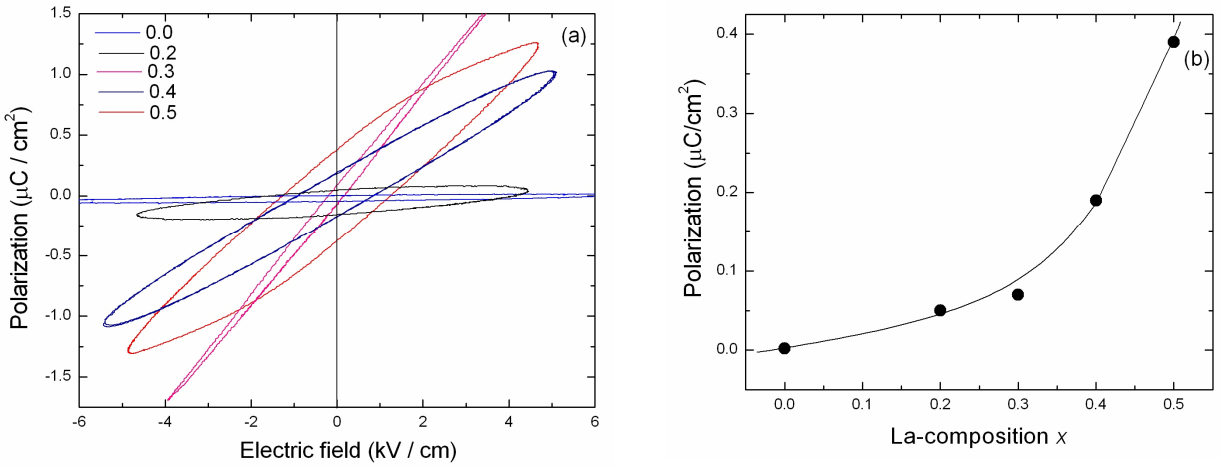

Figure 5.23 (a) Evolution of polarization (*P*-*E*) loop of $(Bi_{1-x}La_x)_{0.5}Pb_{0.5}Fe_{0.5}Ti_{0.5}O_3$ ($0 \leq x \leq 0.5$) at ambient temperature (b) Effect of La-composition on the remanent polarization of $BLFPT_x$. Curve through the data is a guide to the eye.

also see that in the cubic phase (for x = 0.4 and 0.5) the loops at room temperature show a ferroelectric-like behavior (relaxor) with large remnant polarization, although the cubic phase is expected to be paraelectric due to inversion symmetry. The variation of remnant polarization as a function of composition is shown in Fig. 5.23(b). The remnant polarization increases with x rapidly in the cubic phase. Based on the shift of the peak temperature in ε_r vs T plots (Fig. 5.7), the cubic phase of $BLFPT_x$ has shown a relaxor behavior.[39] The relaxor behavior in substituted system has been argued to arise due to formation of polar nano grains due to nano-scale ordering. This is also considered as an evidence of symmetry breaking, consistent with observation of symmetry forbidden Raman scattering in the cubic phase. Thus, the present study of La-substitution in the multiferroic BF-PT system clearly establishes the manner in which the magnetic and dielectric properties are controlled by the tetragonal anisotropy of this system.[47]

5.4 Summary and conclusions

Pure and La-substituted $Bi_{1-x}La_xFeO_3$-$PbTiO_3$, polycrystalline samples were synthesized for compositions x = 0.0, 0.2, 0.3, 0.4 and 0.5 by the solid-state reaction method. A single-phase

Perovskite structure was confirmed from X-rays diffraction. The system is found to exhibit a tetragonal-cubic structural transition at $x = 0.4$. In analogy with the tetragonal $PbTiO_3$, pure BF-PT also shows all the predicted Raman active vibrations. Although upon substituting Bi by La the intensities of the Raman modes are found to diminish, as many as seven modes are found in the cubic phase, which have correspondence with the modes of the tetragonal structure. These modes, although forbidden by the cubic point group symmetry, are activated by the substitutional disorder and represent phonon density of states. The decrease in the anisotropy splitting of the A_1 and E phonons is found to be consistent with the reduction in c/a ratio. The increase in LO-TO splitting upon increasing La-composition arises due to increased ionicity in the mixed-crystal system. *In-situ* X-ray diffraction at high-temperature for $x = 0.0$, 0.2 and 0.3 reveals that this tetragonal system undergoes a structural transition to a cubic phase at elevated temperature. The transition temperature is found to decrease with increasing x and an x-T phase diagram is reported.

Temperature dependence of mode frequencies shows a monotonic decrease, typical of anharmonic behavior. The discontinuous changes in the mode frequencies at 618 K in $x = 0.3$ sample is found to be associated with the tetragonal-cubic transition. In contrast to the expected broadening, two modes are found to become sharper at elevated temperature. This is believed to arise due to reduction of anisotropy in the system. The shape of M-H loops at low temperature suggests existence of magnetically ordered clusters in an overall paramagnetic matrix. However, evidence of spin glass behavior is found in $x = 0.2$ compound. The dielectric response is found to increase with increasing La-composition in the tetragonal phase. On the other hand, the cubic phase exhibits the relaxor behavior arising from the existence of polar nano regions.

References

1. Yu. N. Venevtsev, G. Zhdanov, and S. Solov'ev, Sov. Phys. Crystallogr. **4**, 538 (1960).
2. G. Smolenskii, V. Isupov, A. Agranovskaya, and N. Krainik, Sov. Phys. Solid State **2**, 2651 (1961).
3. F. Kubel and H. Schmid, Acta Crystallogr., Sect. B: Struct. Sci. **46**, 698 (1990).
4. M. M. Kumar, V. R. Palkar, K. Srinivas, and V. Suryanarayana, Appl. Phys. Lett**. 76**, 2764 (2000).
5. S. T. Zhang, M. H. Lu, D. Wu, Y. F. Chen, and N. B. Ming, Appl. Phys. Lett**. 87**, 262907 (2005).
6. X. Qi, J. Dho, R. Tomov, M. G. Blamire, and J. L. MacManus-Driscoll, Appl. Phys. Lett**. 86**, 062903 (2005).
7. W. M. Zhu and Z.–G. Ye, Ceram. Int. **30**, 1435 (2004).
8. V. V. S. S. Sai Sunder, A. Halliyal, and A. M. Umarji, J. Mater. Res. **10**, 1301 (1995).
9. M. M. Kumar, A. Srinivas, S. V. Suryanarayana, and T. Bhimasankaram, Phys. Status Solidi A **165**, 317 (1998).
10. K. Balamurugan, N. H. Kumar, and P. N. Santhosh, J. Appl. Phys. **105**, 07D909 (2009).
11. W.-M. Zhu, H.-Y. Guo, and Z.-G. Ye, Phys. Rev. B **78,** 014401 (2008).
12. A. Singh, A. Gupta, and R. Chatterjee, Appl. Phys. Lett. **93**, 022902 (2008).
13. J. Cheng, S. Yu, J. Chen, and Z. Meng, Appl. Phys. Lett. **89,** 122911 (2006).
14. N. K. Karan, R. S. Katiyar, T. Maiti, R. Guo, and A.S. Bhalla, J. Raman Spectrosc. **40,** 370 (2009).
15. J. Frantti and V. Lantto, Phys. Rev. B **56**, 221 (1997).
16. J. Frantti, V. Lantto, and J. Lappalainen, J. Appl. Phys. **79**, 1065 (1996).
17. A. Slodczyk, P. Daniel, and A. Kania, Phys. Rev. B **77,** 184114 (2008).

18. H. Zhang, S. Leppavuori, and P. Karjalainen, J. Appl. Phys.**77**, 2691 (1995).

19. P.S. Dobal, A. Dixit, and R. S. Katiyar, J. Appl. Phys. **89**, 8085 (2001).

20. C. Chemarin, N.Rosman, T. Pagnier, and G. Lucazeau, J. Solid State Chem. **149**, 298 (2000).

21. S. M. Cho and H. M. Jang, Appl. Phys. Lett. **76**, 3014 (2000).

22. M. N. Iliev, A. P. Litvinchuk, H.-G. Lee, C. L. Chen, M. L. Dezaneti, C. W. Chu, V. G. Ivanov, M. V. Abrashev, and V. N. Popov, Phys. Rev. B **59**, 364 (1999).

23. A. S. Bborovik-Romanov, Sov. Phys. JETP **11**, 786 (1960).

24. I. Sosnowska, R. Przenioslo, P. Fischer, and V. A. Murashov, J. Magn. Magn. Mater. **160,** 384 (1996).

25. R. Martinez, R. Palai, H. Huhtinen, J. Liu, J. F. Scott, and R. S. Katiyar, Phys. Rev. B **82,** 134104 (2010).

26. N. Waeselmann, B. Mihailova, B. J. Maier, C. Paulmann, M. Gospodinov, V. Marinova, and U. Bismayer, Phys. Rev. B **83,** 214104 (2011).

27. Thorsten Leist, Torsten Granzow, Wook Jo, and Jurgen Rodel, J. Appl. Phys. **108**, 014103 (2010).

28. K. K. Mishra, R.M. Sarguna, S. Khan, and A.K. Arora, AIP Advances **1**, 032126 (2011).

29. R. E. Eitel, C. A. Randall, T. R. Shrout, P. W. Rehrig, W. Hackenberger, and S-E Park, Jpn. J. Appl. Phys. **40**, 5999 (2001).

30. M. D. Fontana, H. Idrissi, G. E. Kugel, and K. Wojcik, J. Phys.: Condens. Matter **3**, 8695 (1991).

31. D. S. Fu, H. Iwazaki, H. Suzuki, and K. Ishikawa, J. Phys.: Condens. Matter **12,** 399 (2000).

32. O. Pages, A.V. Postnikov, M. Kassem, A. Chafi, A. Nassour, and S. Doyen, Phys. Rev. B **77,** 125208 (2008).

33. S. Sahoo, S. Dhara, V. Sivasubramanian, S. Kalavati, and A. K. Arora, J. Raman Spectrosc. **40**, 1050 (2009).

34. C. Chemarin, N.Rosman, T. Pagnier, and G. Lucazeau, J. Solid State Chem. **149**, 298 (2000).

35. A. Singh, R. Chatterjee, S. K. Mishra, P. S. R. Krishna, and S. L. Chaplot, Arxiv:1002.1545.

36. R. Palai, H. Schmid, J. F. Scott, and R. S. Katiyar, Phys. Rev. B **81**, 064110 (2010).

37. R. Ranjan, R. Hackl, A. Chandra, E. Schmidbauer, D. Trots, and H. Boysen, Phys. Rev. B **76**, 224109 (2007).

38. R. Ouillon, J-P Pinan–Lucarre, P. Ranson, Ph Pruzan, S. K. Mishra, R. Ranjan, and D. Pandey, J. Phys.: Condens. Matter **14**, 2079 (2002).

39. K. K. Mishra, V.Sivasubramanian, R. M. Sarguna, T. R. Ravindran, and A.K. Arora, J. Solid State Chem. **184**, 2381 (2011).

40. A. K. Arora, D. U. Bartholomew, D. L. Peterson, and A. K. Ramdas, Phys. Rev. B **35**, 7966 (1987).

41. T. R. Ravindran, A. K. Arora, and T. A. Mary, Phys. Rev. B **67**, 064301 (2003).

42. R. Palai, H. Huhtinen, J. F. Scott, and R. S. Katiyar, Phys. Rev. B **79**, 104413 (2009).

43. M. Gruyters, Phys. Rev. Lett. **95**, 077204 (2005).

44. K. Binder and A. P. Young, Rev. Mod. Phys. **58**, 801 (1986).

45. K. H. Fischer and J. A. Hertz, *Spin Glasses* (Cambridge University Press, Cambridge, 1993).

46. J. B. Yi, J. Ding, Y. P. Feng, G. W. Peng, G. M. Chow, Y. Kawazoe, B. H. Liu, J. H. Yin, and S. Thongmee, Phys. Rev. B **76**, 224402 (2007).

47. K. K. Mishra, A. T. Satya, A. Bharathi, V. Sivasubramanian, V. R. K. Murthy, and A. K. Arora, J. Appl. Phys. **110**, 123529 (2011).

Chapter 6

Summary and conclusions

6.1 Summary

Perovskite ferroelectric compounds with general formula ABO_3 have been of interest both from fundamental and applications point of view. Based on their dielectric behaviour the ferroelectric materials can be classified in three broad categories: (a) normal ferroelectric materials such as $PbTiO_3$, $KNbO_3$ etc. (b) relaxor-ferroelectric materials such as $Pb(Mg_{1/3}Nb_{2/3})O_3$, $K(Ta_{1-x}Nb_x)O_3$ etc., and (c) multiferroic materials such as $BiFeO_3$, $Bi_{1-x}Sr_xFeO_3$, which exhibit more than one ferroic order (ferroelectric + magnetic order). This thesis discusses results of Raman and Brillouin spectroscopic investigations of phase transitions in one representative system of each type: (a) ferroelectric $NaNbO_3$, (b) relaxor-ferroelectric $Pb(Zn_{1/3}Nb_{2/3})_{0.85}Ti_{0.15}O_3$ (PZN-PT) and (c) multiferroic $(Bi_{1-x}La_x)_{0.5}Pb_{0.5}Fe_{0.5}Ti_{0.5}O_3$, $0 \leq x \leq 0.5$ (BLF-PT). Temperature is used as a primary thermodynamic parameter to take the system across phase transition(s). Where ever possible, both polycrystalline ceramic samples and single crystals are investigated. In the case of BLF-PT, tetragonal-cubic structural transition induced by La-composition as well as by temperature is studied using *in-situ* high temperature X-ray diffraction. Supporting dielectric and magnetic measurements are also carried out, where ever necessary. Correlations of these properties with structural changes are also discussed. The new results obtained from the present set of studies are listed later in the chapter.

A detailed Raman spectroscopic study of $NaNbO_3$ ceramic synthesized by solid state reaction method was carried out to study the anti-ferroelectric to ferroelectric transition both in cooling and heating cycles in the temperature range 10–300 K. The spectra were analyzed to obtain the temperature dependence of mode wavenumbers. The temperature dependence of integrated intensities of low as well as high wavenumber modes has been examined in detail to

obtain information about coexistence and hysteresis. In addition, single crystals of $NaNbO_3$ were grown by flux method and Brillouin scattering measurements were carried out from ambient to 773 K to study the central peak across the anti-ferroelectric (D_{2h}^{11}, Z=8) to anti-ferroelectric (D_{2h}^{13}, Z=24) transition (P to R phase). The behaviours of the low-frequency Raman modes and the CP were obtained as a function of temperature. The temperature-dependence of the relaxation time was analysed to obtain the activation energy of the relaxation process.

Single crystals of $Pb(Zn_{1/3}Nb_{2/3})_{0.85}Ti_{0.15}O_3$ were grown by flux method. Brillouin spectroscopic studies of tetragonal-cubic transition and the dynamical behaviour of polar nano regions (PNRs) were investigated over a wide range of temperature. The behaviour of acoustic phonon and the central peak across the transition and their correlation with dynamical behaviour of PNRs were examined in details. In addition, polarized *micro*-Raman spectroscopy has been employed in the temperature range 298-873 K to study the behaviour of phonon across tetragonal-cubic phase transition. Anomalies in the temperature dependence of mode frequencies and line-width of 273 cm^{-1} mode were examined to identify the structural transition and the intermediate characteristic temperature for freezing of PNRs.

Polycrystalline $(Bi_{1-x}La_x)_{0.5}Pb_{0.5}Fe_{0.5}Ti_{0.5}O_3$ powder samples were synthesized for x = 0.0, 0.2, 0.3, 0.4 and 0.5 by the solid-state reaction technique. Structural and vibrational properties of pure and La-substituted BLF-PT compounds were studied at ambient using X-ray diffraction and Raman spectroscopy. The emphasis was to understand the nature of the phonons in this mixed-crystal system and to probe the crystallographic phase transition. The structural stability of these technologically important solid-solutions has been investigated at elevated temperature. The phonons, magnetic and ferroelectric ordering in La-substituted BLF-PT were investigated as a function of temperature using Raman, magnetization and polarization measurements. The Raman spectra are analyzed quantitatively to obtain mode frequencies, their line-widths and intensities.

Magnetization measurements are made from ambient down to 4 K in field-cooled and zero-field cooled conditions. The field dependence of magnetization is also studied to examine the possibility of a spin-glass-like magnetic ordering. From the ferroelectric hysteresis loop, the composition dependence of remnant polarization is also obtained. The observed results are discussed in the context of anisotropy and tetragonal-cubic structural transition.

6.2 Conclusions

The significant new results presented in this thesis are:

1. Hysteresis and two-phase coexistence were determined across orthorhombic-rhombohedral transition in $NaNbO_3$ (hysteresis ~80 K, coexistence ~60 K).[1]
2. Anomalies in the intensity of the central peak and relaxation time in $NaNbO_3$ single crystal suggest order-disordered nature of anti-ferroelectric (D_{2h}^{11}, Z=8) to anti-ferroelectric (D_{2h}^{13}, Z=24) (P to R phase) transition at ~643 K using Brillouin scattering technique. The activation energy for hopping of Nb ion between allowed and vacant sites is estimated.[2]
3. The behavior of relaxation times obtained from LA phonon and central peak in PZN-PT single crystal in the relaxor-cubic phase suggests electrostrictive coupling between the strain and polarization fluctuation begins to take place below temperature T_B. The relaxation time of CP exhibits critical slowing down upon approaching the tetragonal-cubic transition suggesting the order-disorder nature of phase transition.[3]
4. Polarized Raman measurements on PZN-PT across tetragonal-cubic transition (473 K) exhibit anomalies in mode frequencies and line-widths.[4]
5. BLF-PT is found to undergo a tetragonal-cubic transition at $x \geq 0.4$.[5]
6. A x-T phase diagram of BLF-PT is obtained for the first time.[6]
7. Remnant polarization increases with La-doping x in BLF-PT.[7]

8. Large polarization and forbidden Raman scattering in the cubic phase of BLF-PT is attributed to symmetry breaking due to formation of PNRs leading to relaxor behavior.[7]
9. Magnetic hysteresis in BLF-PT suggests existence of ferromagnetic clusters embedded in paramagnetic host. For $x = 0.2$ system an Ising-type spin-glass behavior was found.[7]
10. Evidence of tetragonal-cubic transition is found at 618 K from *T*-dependence of mode frequencies in $x = 0.3$ BLF-PT.[7]

6.3 Directions for future studies

- Study on local structure of $NaNbO_3$ system by using extended X-rays absorption fine structure (EXAF) technique would be helpful to find the local nano-scale ordering and hence one would be able to understand the rhombohedral and orthorhombic coexistence mechanism. Furthemore, in case of BLF-PT, as the degree of disorder increases with La-substitution for Fe and Ti in Pb-based complex Perovskite, the systematic change in the local structure can be obtained using EXAFS. This can further improve the understanding of the structural transition. The distinct advantage of this technique is in its ability to probe the dynamical distortions in the time scale of the order of 10^{-15} s as compared to the other techniques such as Raman scattering whose characteristic time scale of measurement is 10^{-10} s or longer.
- The direction of ionic displacements responsible for the spontaneous dipole moment of PNRs and the local structure of PNRs can be investigated using dynamical structural analysis of diffuse neutron scattering.
- Acoustic emission technique can be used for further studying the PNR-related phase transitions in relaxor. Using this method one can detect classical phase transitions as well as anomalies related to PNRs in relaxors.

- From applications point of view, magnetoelectric coupling coefficient, dielectric and magneto-dielectric studies can be carried out on BLF-PT and its possible correlation with structure will be useful.
- Single crystals on BLF-PT can be grown and studied for obtaining a better understanding of the phonons in this mixed-crystal system. In single crystals of BLF-PT Brillouin spectroscopy can also be employed for studying phase transition.

References

1 Low-temperature Raman spectroscopic studies in $NaNbO_3$
K. K. Mishra, V. Sivasubramanian, and A. K. Arora,
J. Raman Spectrosc. **42**, 517 (2011).

2 Brillouin spectroscopic study of central peak in $NaNbO_3$ single crystal
K. K. Mishra, V. Sivasubramanian, A.K. Arora, and R. M. Sarguna (Under review).

3 Anomalous behavior of acoustic phonon mode and central peak in $Pb(Zn_{1/3}Nb_{2/3})_{0.85}Ti_{0.15}O_3$ single crystal studied using Brillouin scattering
K. K. Mishra, V. Sivasubramanian, A.K. Arora, and D. Pradhan (Under review).

4 Polarized *micro*-Raman spectroscopic study of relaxor $Pb(Zn_{1/3}Nb_{2/3})_{0.85}Ti_{0.15}O_3$ single crystal
K. K. Mishra, V. Sivasubramanian, A.K. Arora, and D. Pradhan (Under review).

5 Raman scattering from La-substituted $BiFeO_3$–$PbTiO_3$
K. K. Mishra, V. Sivasubramanian, R. M. Sarguna, T. R. Ravindran, and A. K. Arora, J. Solid State Chem. **184**, 2381 (2011).

6 *x*-T phase diagram of La-substituted $BiFeO_3$-$PbTiO_3$
K. K. Mishra, R. M. Sarguna, S. Khan, and A. K. Arora, AIP Advances **1**, 032126 (2011).

7 Vibrational, magnetic, and dielectric behavior of La-substituted $BiFeO_3$-$PbTiO_3$
K. K. Mishra, A. T. Satya, A. Bharathi, V. Sivasubramanian, V. R. K. Murthy, and A. K. Arora, J. Appl. Phys. **110**, 123529 (2011).